Excitons in monolayer semiconductors in complex environments and under external fields

DISSERTATION ZUR ERLANGUNG DES DOKTORGRADES
DER NATURWISSENSCHAFTEN (DR. RER. NAT.)
DER FAKULTÄT FÜR PHYSIK
DER UNIVERSITÄT REGENSBURG

vorgelegt von

Jonas Zipfel
aus Regensburg

Februar 2020

Das Promotionsgesuch wurde eingereicht am: 04.12.2019
Die Arbeit wurde angeleitet von: Dr. Alexey Chernikov

Prüfungsausschuss:	Vorsitzender:	Prof. Dr. Vladimir Braun
	Erstgutachter:	Dr. Alexey Chernikov
	Zweitgutachter:	Prof. Dr. Christian Schüller
	weitere Prüfer:	Prof. Dr. Dominique Bougeard

Excitons in monolayer semiconductors in complex environments and under external fields

DISSERTATION ZUR ERLANGUNG DES DOKTORGRADES
DER NATURWISSENSCHAFTEN (DR. RER. NAT.)
DER FAKULTÄT FÜR PHYSIK
DER UNIVERSITÄT REGENSBURG

vorgelegt von

Jonas Zipfel
aus Regensburg

Februar 2020

Contents

Chapter 1
Introduction

Preface - a few personal considerations

Writing this first part of the work I find myself at a point where it is commonly expected to give a motivation for what has been researched. This immediately leads me to confront the question, that I have heard what feels like a thousand times over the course of this work: *"What can it be used for?"*. In terms of the audience reached with this work, such a question might have less relevance, however, given how often I encountered it, also in scientific surroundings, it at least deserves a few words of consideration. Quite obviously it can be extended to a bigger philosophical magnitude of questioning what anything is ever useful for, that has racked many a brains and is far beyond the few words I will spare it here. Yet I feel the need to give at least a somewhat satisfactory justification for why I have put three years of work into this research. Turning back to the question under the aspect of whether this work has direct relevance for any applications, I can honestly state that I do not know. But I also do not think that it is the relevant question here. Research can and should not be judged on whether it yields direct relevance or use for novel applications. It is rather directed in gathering information about promising systems, concepts or ideas, with no certainty of whether the proposed big breakthrough is found in the end. In a way it is comparable to the prominent parabola of exploring a cave, where someone might choose a certain branch-off, not knowing whether he finds a dead end or the anticipated light at the end of the tunnel. In this context it is common to encounter one or the other dead end, or find no exit at all, but that should not stop us from searching. The gathered information can be used to draw a map of a bigger picture, that is then of assistance for further (re)searches. The more important question is thus, whether choosing a certain path can yield new, relevant or helpful information based on what we already know. With that being put up front, let me try to give the expected motivation, in terms of simply introducing the branch of the tunnel that we are in, for this particular work. It is then upon the individual reader to assess, whether, in the context of existing technologies, concepts and ideas, it is worth to be further pursued.

Motivation

Understanding, controlling and manipulating charge carriers has been the fundamental concept of everyday information technology, since at least the demonstration of the first working transistor in 1948 [1] and thus lays the very foundation for almost every electrical or opto-electrical device based on semiconducting materials. An ever increasing demand of computing power, while at the same time keeping devices of handy size, has long called to the need for a shrinking of the individual operating units [2]. However, the miniaturization of electronic devices has also manifested itself particularly in making devices thinner, with futuristic concepts such as fully transparent and flexible devices starting to take a hold in everyday life [3–5]. From a more realistic point of view this rises the quite general and omnipresent question of *"where are the limits?"*. Given the state of the art understanding of solid state physics, the answer to such a question is readily found in the smallest stable material quantity known to us: a single atom. Now while it is widely known that atoms do not live up to the greek etymology of their name-giving as being 'indivisible', a single layer of atoms does still constitute the thinnest stable material system one can imagine to exist.

On one hand, just taking the concept of such a system, it is found that the reduction of a material's dimensions to such dramatic extent brings along intriguing aspects to consider. It is well understood, that such dimensional confinement leads to arising quantization effects in their electronic structure [6], resulting in a wide range of novel physical concepts and properties, readily utilized in state of the art opto-electrical technologies [7]. However, the room for postulated ideas and potential applications in this world of quantum-engineering is still seemingly limitless [8]. On the other hand, one should recognize what results from the fact of a material really being intrinsically two-dimensional in a realistic scenario. Following this thread of thought, it is of particular interest to refer to a famous saying, attributed to Pauli [9], stating that the surfaces of materials were "made by the devil". They set a boundary to the well ordered and structured system of the bulk material and thus give rise to a source for significant amounts of inhomogeneities, disorder and impurities [10]. In sufficiently big bulk materials, electronic properties are dominated by the volume and the influence of these surface and interface states is mostly of subordinate importance. However, decreasing the dimensionality of a structure then calls back the significance of precisely such states. In the limit of single layers of atoms, that are materials of inherent two-dimensional character, this is taken to the extreme, as they can also be viewed to be pure surfaces. Following Pauli's reasoning one would then come to the conclusion, that such materials are of the devil's own making, as reducing their size to such fundamental limits introduces a potential for chaotic amounts of disorder. In this context however, it should

be acknowledged that controlling disorder and defects is one of the most fundamental concepts for the tailoring of material properties [11, 12]. The 2D-character of this class of materials thus gives ways to proverbially play tricks on the devil, in the means of making use of exactly that pronounced surface sensibility. It opens up a whole new way of influencing and controlling charge carrier dynamics, that is in form of the material's direct *surroundings*. In contrast to conventional quantum well systems, this might even be extended to the concept of combining multiple such single-atom layers via lateral stacking to create novel materials with entirely unseen electronic properties [13].

Resulting from such concepts and ideas follows an incentive for the search of materials and structures that approach such a two-dimensional limit, while at the same time holding suitable and intriguing electronic properties. By now there are a wide range of available ultra-thin materials from all different material classes, including metals, semi-metals, semiconductors, insulators, superconductors etc. [14–16] An important class of such materials is found in single layers of van-der-Waals crystals, due to the discovery that monolayers of such materials can be easily fabricated through exfoliation of mono-crystalline bulk crystals. First prominently demonstrated on the example of graphite, yielding single layers of graphene [17, 18], a rapidly evolving field of these two-dimensional crystals was established, with van-der-Waals crystals spanning a huge variety of available and stable elemental compositions [19].

A sub-class of such structures that has spread wide interest in the scientific community over the past several years is that of the two-dimensional semiconductors, in particular in the form of monolayers of transition metal dichalcogenides (TMDC). This is mainly due to two important intrinsic properties. On the one hand, as first demonstrated for the compound of MoS_2 [20, 21], TMDCs have direct bandgap character in the monolayer limit. On the other hand, as a result from quantum and dielectric confinement, Coulomb interactions in these systems are significantly enhanced [22, 23]. This gives rise to the formation of extraordinarily tightly bound electron-hole pairs, called excitons. These quasi-particles are found to have binding energies sufficiently high ($\sim 500\,\mathrm{meV}$) to make them stable under ambient conditions and therefore dominate the charge carrier properties of these materials even under room temperature [24].

Together these two properties lead to remarkably efficient light-matter coupling in these materials. From such intriguing properties follows a variety of proposed concepts, including the fabrication of artificial heterostructures as mentioned above [25], seemingly well accessible from simple and efficient fabrication methods, such as exfoliation and subsequent stamping onto desired substrates [26]. While such methods lack scalability, they turn out to be a suitable and efficient approach to build even complex structures on a laboratory scale. From that, the easy access to exciton dynamics via optical means made these two-dimensional structures a prototypical platform for the

study of fundamental physical concepts and effects, arising from the quantum confinement in one direction. It has turned out to be of particular interest for the investigation of excitonic properties in systems where, in contrast to conventional semiconductors, excited charge carriers are generally not found in an unbound state. Here, a wide range of novel physical phenomena can be studied. In particular, it is of interest to point towards the physical behavior found in connection with excitons in these systems, baring remarkable resemblance to the concept of a hydrogen atom as known from classical atomic physics. Such findings include an excitonic Rydberg series of excited states [27, 28], charged excitons [29, 30] or even exciton aggregates, so called biexcitons [31–33]. Additionally their peculiar band structure gives rise to riveting effects, such as coupling of spin and valley degree of freedom, allowing for the selective optical addressing of spin states and introducing a novel stage for the research of spin phenomena [34–36]. Finally such intriguing exciton properties also give rise to more futuristic opto-electrical innovations and conceptional devices [15, 37, 38], not least arising from the materials' capability to efficiently transport photoexcitations in the form of correlated electron-hole pairs over considerably large distances [39, 40].

In the frame of this work we use these remarkable electro-optical properties and dedicate ourselves to the study of fundamental exciton properties. With remark to Pauli's statement, we show that the material's optical response can be used to investigate influences of the surroundings, in particular disorder, on the bound charge carrier states, given the two-dimensional character of the structures. Via optical spectroscopy, insight into the exciton ground and excited states' spatial extent from field induced resonance shifts is given. We further investigate the impact of environmental disorder and moreover study how it can be suppressed in a controlled way, using the concept of above mentioned artificial heterostructures. We then utilize such structures to study exciton transport dynamics and examine the influence of disorder effects by comparing the results to that of pristine monolayers subjected to significant disorder [40].

Finally, we also investigate a different two-dimensional semiconductor system, that of layered halide perovskites. These systems find wide interest, in particular in the use as suitable materials for photo-voltaic devices and their research in the past was indeed driven from a more application oriented point of view. However, their similar optical response compared to TMDC monolayers, in particular the formation of equally tightly bound excitons, has sprung an incentive for are more in-depth understanding of their general electro-optical properties. We show that our theoretical understanding, as well as experimental methods from the study of two-dimensional TMCD structures can be extended to such systems. Moreover, we find that it provides a way to empirically study fundamental material properties and exciton dynamics that are yet theoretically hard to capture.

Chapter 2
Theoretical background

In the first segment of this scientific discourse the necessary theoretical background for the underlying work shall be presented. The first section gives an introduction into the basic properties found in the two-dimensional semiconductor materials of monolayer transition metal dichalcogenides. Their intriguing electro-optical properties are highlighted with particular focus on the extraordinarily strong light-matter interaction and formation of tightly bound excitons. Hereafter, sections 2.2 - 2.5 are dedicated to more specific topics and the content as well as the structuring follow closely along with experimental results presented in chapter 4, defining a central theme to follow. For this purpose the second section discusses the origin of magnetic field induced energy shifts of exciton resonances and details how these are linked to fundamental properties of the same. The following section outlines the relevance of a material's surroundings, given an inherent two-dimensional character and how this can affect experimental observations. In the third section, the concept of excitons as freely moving quasi-particles is detailed and the theoretical description of such transport processes is captured. Finally, in the last section a different two-dimensional semiconductor material class, that of layered hybrid halide perovskites, will be discussed and similarities to the monolayer TMDCs will be illustrated on an empirical basis.

2.1 Basic properties of transition metal dichalcogenides

In this first part we focus on the fundamental properties of transition metal dichalcogenides (TMDC) in the limit of an atomically thin monolayer of the material. While at first a brief introduction to their crystal structure is given, the main focus lies on their electronic structure and resulting electro-optical properties. Particular focus is put on the strong light-matter interaction, dominated by the formation of bound electron-hole pairs (excitons), as a result from quantum and dielectric confinement effects due to their two-dimensional character. While in this context general properties of excitons and exciton formation dynamics in ultra-thin semiconductors are discussed, also more specific concepts, resulting from the unique band structure of TMDC materials, are introduced.

2.1.1 Crystal structure

Real space lattice

Transition metal dichalcogenides (TMDCs) in bulk form are so called van-der-Waals crystals, meaning, that in analogy to the well known graphite, these crystals are built from stacked layers, weakly bound by van-der-Waals forces in the out-of-plane direction. In the in-plane direction, however, the single layers are formed by strong covalent bonds, resulting in a honeycomb-like hexagonal lattice [41–43]. In contrast to graphite, TMDC layers have two different atoms in their base lattice, shown in fig. 2.1 (a) in a top view, which leads to a reduced D_{6h} point group symmetry with in-plane lattice constants between two atoms of the same type typically ranging around 3.1-3.3 Å [44]. There are three known different stacking orders called 1T, 2H and 3R phases [45], where the 1T phase is a non-stable phase, that is not found to exist naturally [46–48].

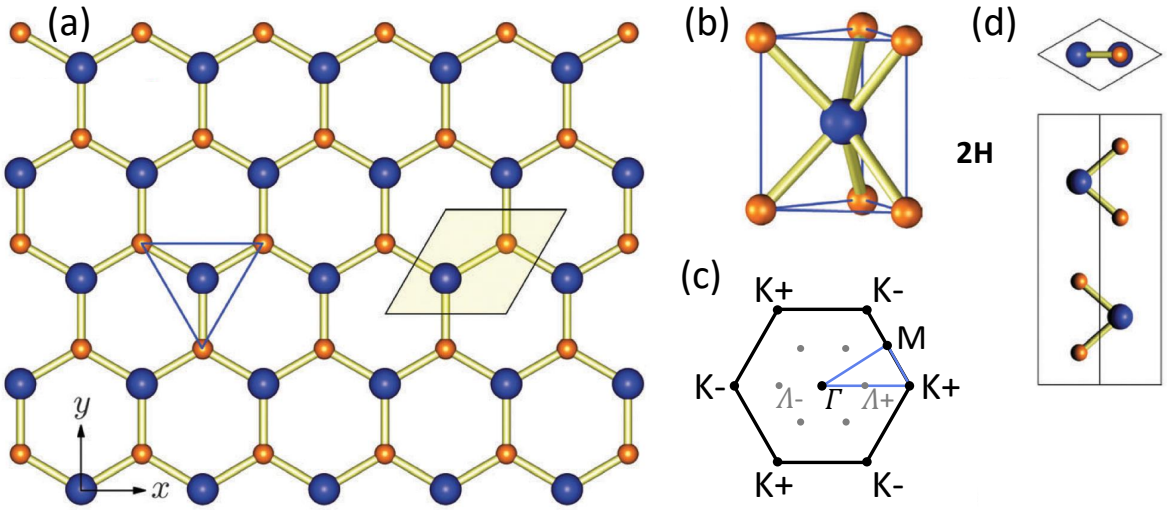

Figure 2.1: Adapted from [45]: (a) Top view of a single layer of a transition metal dichalcogenide crystal, with transition metal atoms in blue and chalcogenides in orange. The yellow diamond represents the unit cell. (b) Three dimensional cutout of the single layer along the blue triangle shown in (a). (c) First Brillouin zone of a TMDC monolayer including high symmetry points. (d) Schematic representation of the 2H phase, with alternating layers being rotated by 180° and ABAB stacked.

While in principle both 2H and 3R phase can be stable, first principle calculations show the 2H form to be the energetically favorable phase [49]. Accordingly, most of the available TMDC materials are found in the 2H form [50], where alternating layers are stacked in an ABAB pattern on top of each other, with an additional 180° twist angle between adjacent layers (see fig. 2.1 (d)). As a consequence only this phase will be considered in the scope of this work. Fig. 2.1 (b) shows a cutout of a single layer along

the blue triangle. It can be seen, that a single layer of these materials is made up by basically sandwiching a layer of transition metals between two layers of chalcogenides. Considering the unit cell of such a crystal illustrated in fig. 2.1 (a) by a yellow diamond, one yields the stochiometric formula of MX_2, where M is a transition metal and X a chalcogen atom. While there are different combinations of elements to form TMDCs, the relevant material systems for this work include only the prominent combinations of M=Mo/W and X=S/Se. From now on referring to TMDCs will only include these four combinations.

Since single layers of such crystals are only weakly bound to one another, it was found that they can be easily separated by mechanical exfoliation down to a single monolayer [17, 18]. While this does have immediate consequences for the electronic band structure due to quantum confinement effects (further discussed in the next section), it also leads to breaking of the inversion symmetry [51, 52]. A bulk hexagonal lattice in 2H stacking does always have an inversion center in the approximation of the bulk being infinitely big compared to the surface. This approximation, however, breaks down when considering crystals of only few layers. In this limit even numbered layers will still have an inversion center, since in 2H stacking, a transition metal atom of the subsequent layer will always be stacked on top of a chalcogen atom of the previous layer (see fig. 2.1 (d)). For odd numbered layers in the few layer limit though, this will lead to a breaking of the inversion symmetry, most easily evident in the case of a monolayer. As a consequence, the symmetry group is reduced to a three-fold rotational symmetry with the point group D_3h [45].

Reciprocal lattice

The hexagonal real space lattice of monolayer TMDCs results in the first Brillouin zone of the reciprocal lattice also being hexagonal, as shown in fig. 2.1 (c). The blue lining indicates a trace, typically used in band structure calculations, including important high symmetry points such as the K−points at the corners of the first Brillouin zone and the Λ−points (also referred to as Q−points in a bulk crystal), located between Γ− and K−points. Due to the inversion symmetry breaking in the monolayer limit, time reversal symmetry constitutes that high symmetry points are no longer completely equivalent. Instead, opposing points in the Brillouin zone are distinguishable by different valley indices $\tau = \pm 1$, meaning only every second point is fully equivalent with the other. This is commonly distinguished by two equivalent notations, either by marking points with + or - (e.g. K+/K-), or marking one of the points with an apostrophe (e.g. K/K'). The result is a similar three-fold rotational symmetry in k-space as in real space, with the Γ−point being the rotation center, which has immediate implications for the resulting electronic structure, discussed in the following [20].

2.1.2 Electronic structure

Transition to a direct semiconductor in the monolayer limit

On the basis of such well defined real space and reciprocal lattices, the resulting electronic band structure shall be presented. Here TMDCs in bulk form are well known to be momentum-forbidden indirect semiconductors [41–44]. However, as mentioned in the previous section, the confinement of TMDCs in one dimension, meaning the transition from bulk to a two-dimensional monolayer material, has direct consequences for its electronic properties. It has been found that this confinement leads to a transition of the monolayer TMDCs' band structure from an indirect bandgap to a direct bandgap one [20, 21, 53]. This will be showcased in detail on the prominent example of MoS_2, although being analogous for the other TMDCs.

In a bulk crystal of the material the bandgap is found between valence band maximum located at the $\Gamma-$point and conduction band minimum at the Q$-$points, as depicted for a calculated band structure of MoS_2 in the left panel of fig. 2.2. For a decrease in

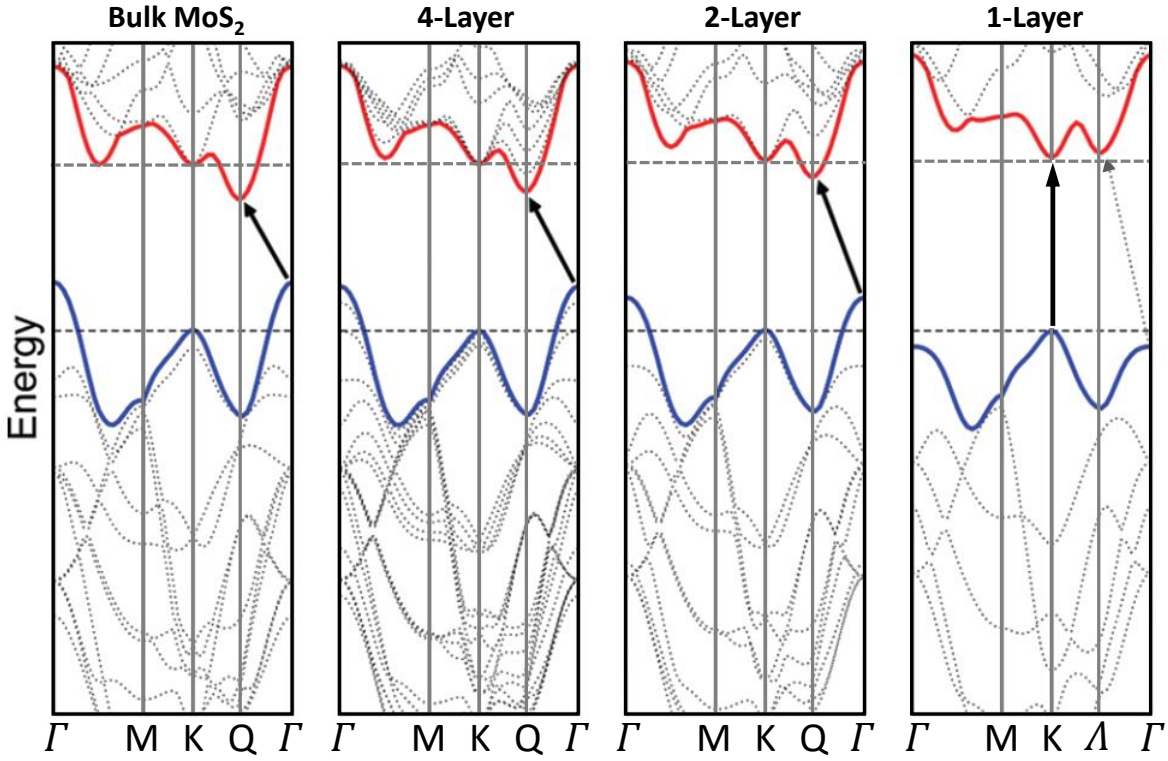

Figure 2.2: Adapted from [21]. Calculated change of the MoS_2 band structure when transitioning from bulk to the monolayer limit. While for bulk, 4-layer and 2-layer MoS_2 (left three panels respectively) an indirect transition between $\Gamma-$point in valence band and Q$-$points in conduction band is expected, the material changes to a direct semiconductor at the K$-$points in the monolayer limit (right panel).

the number of layers, the calculations show (right panels), that the considered Γ− and Q−points shift to lower and higher energy respectively. This, in the limit of a monolayer, leads to the Γ−point being lower in energy than the K−points in the valance band and at the same time the Λ−points (former Q−points) being higher in energy than the K−points in conduction band, hence making the material a direct semiconductor at the K−points.

To understand this effect, it is helpful to consider the tight binding model in a form where bands are the result of the wave function overlap of individual atomic orbitals [54, 55]. While generally different bands (at different points in k-space) can have mixed contributions of various atomic orbitals, for the case of the above-mentioned high symmetry points, the contributions from specific atomic orbitals are well defined. The Γ−point in the valence band is mainly made up by d_{z^2} orbitals and the Λ/Q−points in conduction band by p_x and p_y orbitals, all located at the chalcogen atoms on the outside part of individual layers. As a result those orbitals have a sizable overlap with orbitals of neighboring layers and can hybridize efficiently. This consequentially leads to a significant environmental sensibility of the resulting high symmetry points [21, 53, 56]. When decreasing layer numbers, this hybridization of orbitals of adjacent layers becomes smaller, which in the context of the tight binding model then leads to an energy shift for the underlying bands. Evidently such an effect is strongest when there are no more neighboring layers at all. From the consideration of such orbital hybridizations, it is thus found that a confinement in the z-direction can also have direct consequences for the electronic band structure in the x-y direction. In contrary to that, the K−points are mainly composed of hybridized $d_{x^2-y^2}+d_{xy}$ in valence and d_{z^2} orbitals in conduction band, firmly localized at the transition metals in the center of layers. Following from that, the wave function overlap of these orbitals with neighboring layers is insignificant and the K−points remain mostly insensitive to changes of the environment in the out-of-plane direction [21, 45, 53–56]. Therefor a change in layer numbers hardly affects the band structure at these points.

Spin-orbit splitting and spin-valley locking

From the intriguing finding of TMDCs being direct semiconductors in the monolayer limit, we shall take a more detailed look at this particular point of the band structure. For this we refer to ab initio calculations [57] of monolayer WS_2, as presented in fig. 2.3 (a). In analogy to the case discussed for MoS_2, the direct bandgap is located at the K−points in reciprocal space. As shown, it is found that the inclusion of spin-orbit coupling leads to a significant splitting of valence and conduction bands around the direct gap, originating from contributions of the rather heavy transition metal atoms.

Calculations of the valence band splitting Δ_v^{SOC} in WS_2 yield values on the order of 430 meV and of conduction band splitting Δ_c^{SOC} on the order of 30 meV. For WSe_2 the calculated values are slightly higher, with $\Delta_v^{SOC} \approx 470$ meV and $\Delta_c^{SOC} \approx 40$ meV [56, 58]. Since the main contribution of the spin-orbit splitting stems from the transition metal atoms, the lighter Mo atoms (compared to W) in molybdenum-based materials result in a generally lower spin-orbit splitting ($\Delta_v^{SOC} \approx 160$ meV [34] and $\Delta_c^{SOC} \approx$ 2-10 meV [56]). It shall be noted that, due to different effective masses between the two spin-split conduction bands in Mo-based materials, a resulting band crossing leads to

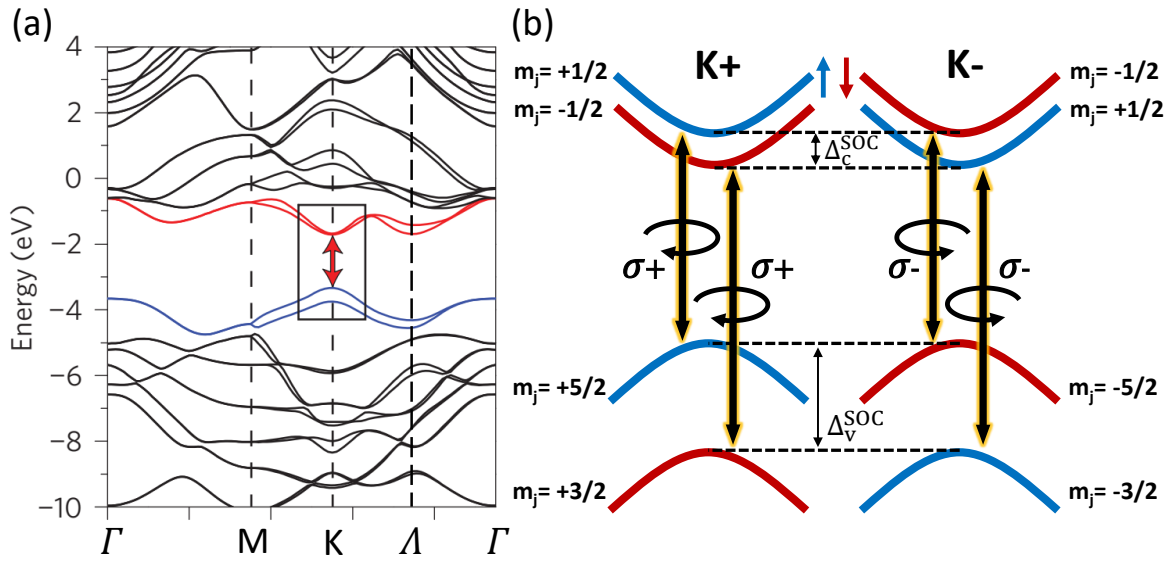

Figure 2.3: (a) Adapted from [57]. Ab initio band structure calculation of a WS_2 monolayer including spin-orbit coupling. The relevant valence and conduction bands are colored and the direct bandgap located at the K-points is indicated. (b) Schematic illustration of the bandgap around the marked region in (a) for both K+/K- valleys. Different spins are color coded and the splitting due to spin-orbit coupling in the respective bands is denoted by $\Delta_{v/c}^{SOC}$. The bands are additionally labeled by the z-component of their total angular momentum m_j and optically allowed transitions are indicated.

an inverted sign of the spin-splitting compared to the valence band [56, 58]. Additionally we find that the spin-orbit splitting has opposite signs in K+/K- valley. This is due to the inversion symmetry breaking in the monolayer limit in combination with time reversal symmetry, that demands $E_\uparrow(\vec{k}) = E_\downarrow(-\vec{k})$, where $\uparrow, \downarrow$ denote the respective spins in the band at wave vector $\vec{k}$. Now if we further consider that the K+/K- valleys are well separated in momentum space, meaning transitions between these valleys are robust against scattering, the significant splitting in the spin degeneracy from SOC implies that valley and spin index are intrinsically coupled [34, 59–62]. This so called spin-valley locking has direct consequences for optical selection rules [34, 63, 64].

Selection rules in TMDC monolayers

TMDC monolayers being direct bandgap semiconductors makes them particularly optically active as it allows direct photoinduced transitions between valence and conduction bands [20, 21]. In order to derive the optical selection rules we use a simplified picture, considering the quantum numbers in valence and conduction band. Again, this shall be exemplary studied for the case of WS_2. As mentioned above, both valence and conduction band have d-orbital character giving them identical principal and azimuthal (orbital) quantum numbers. However, their magnetic quantum number m_l, in the relevant z-axis projection, is different. The d_z orbitals of the K−points in conduction band contribute $m_l = 0$, whereas the hybridized $d_{x^2-y^2}+d_{xy}$ orbitals of valence band contribute $m_l = \pm 2$, with the sign depending on the valley index (for K+/K-) [54, 55, 65]. Considering the spin quantum number contribution ($m_s = \pm 1/2$) we get m_j, the z-component of the total angular momentum, for each of the spin-split bands. For the exemplary case of the K+ valley these yield: $m_j^{v,\uparrow} = +5/2$, $m_j^{v,\downarrow} = +3/2$, $m_j^{c,\uparrow} = +1/2$, $m_j^{c,\downarrow} = -1/2$. An optically allowed transition between states with same spins becomes possible when additionally including the hexagonal lattice symmetry. It can be shown that this symmetry, at the K−points, allows to compensate for a mismatch of value 3, or to put it more mathematically, allows transitions between states $mod\,3$ [63, 64]. As an example, this means a transition between both spin-up valence ($m_j^{v,\uparrow} = +5/2$) and conduction band ($m_j^{c,\uparrow} = +1/2$) in K+ is allowed using right-hand polarized light (Δ quantum number $= +1$), since $+5/2 + 1 = +1/2\ mod\,3$. This case can be made analogously for all valleys, obtaining the selection rules as depicted in fig. 2.3 (b), where excitations in K+ valley are driven by right-hand and vice versa in K- by left-hand polarized light. From this arises the fact that valley and spin in these systems can be selectively addressed via accurately chosen polarized excitation. This, in combination with spin-valley locking, opens up a platform for spectroscopic investigations of spin and valley phenomena [35, 36].

2.1.3 Electro-optical properties - Excitons

Coulomb interaction and exciton formation

Beside TMDC monolayers becoming direct semiconductors, their 2D-character has additional strong implications for their electro-optical properties. The two dimensional quantum confinement leads to remarkably strong Coulomb interactions [22, 23], with only weak dielectric screening of the field lines in the monolayer limit [66–69]. This is schematically depicted in fig. 2.4 (a) in a real space illustration of interacting charges in a TMDC monolayer in free space vacuum (although we note that this concept is generally valid for two-dimensional semiconductors). Most of the field lines extend out-

side of the monolayer limit with the vacuum dielectric constant ε_0 being lower than the TMDC's dielectric constant ε_{TMDC}. This leads to comparably low dielectric screening and subsequently enhanced Coulomb interactions, resulting in mainly two phenomena: A renormalization of the bandgap due to repulsive electron-electron interaction (illustrated in the top panel) [27, 70–72] and formation of strongly bound electron-hole pairs, so called excitons, due to attractive electron-hole interaction (illustrated in the bottom panel) [73–77].

In order to understand this it is helpful to first consider the band structure without Coulomb interactions, shown on the left-hand side in fig. 2.4 (b) for the relevant crystal momentum of the direct bandgap. It shall also be noted that while there are essentially two optically allowed transitions between the spin-split bands (fig. 2.3 (b)), we will only cover the energetically lower transition, referred to as A-transition, while similar arguments can be made for the energetically higher transition (B-transition). Also for simplicity only the optically accessible upper spin-split conduction band is shown. Without Coulomb interactions the transition can be fully covered in a conventional single-particle band structure, where electrons are excited from the valence into the conduction band following the selection rules, thereby leaving an empty electron state (hole) in the valence band. There the transition energy is simply given by the difference of valence and conduction band, yielding the bandgap energy without Coulomb interactions $E_g^{nc} = E_{CB} - E_{CV}$, with E_{CB} and E_{CV} as the respective valence and conduction band energies.

Let us now switch to the case where Coulomb interactions are taken into account. Here we should mention that the single-particle band structure is useful in understanding the properties of the individual charge carriers, but has strong limitations when including the coulombic interactions of the two particles that lead to a bound excitonic complex. For this purpose we switch to a two-particle model, introducing a Wannier-Mott type like exciton picture (the applicability is further discussed in sec. 4.1) with a combined center of mass momentum q_{eh} [22, 23, 73, 78], where

$$q_{eh} = q_e + q_h, \tag{2.1}$$

with electron and hole momenta q_e, q_h respectively. An energy scheme for such a two-particle band structure is depicted on the right-hand side of fig. 2.4 (b). Due to repulsive electron interactions the bandgap renormalizes to higher energies $E_g = E_g^{nc} + \Delta E^c$ (details are further discussed in sec. 2.3.1). At the same time, however, the attractive interactions between electron and hole lead to the formation of distinct excitonic states, that lie below the bandedge by an energy defined by their binding energy $E_{b,n}$, with n as the exciton's principal quantum number.

These excitonic states are commonly labeled as 1s, 2s, 3s, etc. analogously to atomic orbital theory. In fact, the comparison of excitons to a hydrogen atom with a positive core and negatively charged electron, bound together by coulombic forces, can often be a helpful one. However, one major difference of excitons lies within their mass approximation. While in a hydrogen atom the mass is usually approximated by the proton mass due to it being about four orders of magnitude higher than the electron mass, in TMDC systems electron and hole masses are quite similar in their value [56, 79–81]. On account of that a reduced effective exciton mass [23, 73, 78] is introduced as:

$$\mu_{ex} = \frac{m_e m_h}{m_e + m_h}, \tag{2.2}$$

where m_e and m_h are the respective electron and hole effective masses. This mass can therefore be theoretically estimated from the individual effective charge carrier masses of single-particle calculations. For the investigated TMDCs values around 0.15-0.2 m_0 of the electron rest mass m_0 are obtained. Note that this is not to be confused with the exciton total mass $M_{ex} = m_e + m_h$ that is a simple sum of the individual effective masses and yields values around 0.5-1 m_0 [56, 79–81].

Within such a frame we could expect the Rydberg series of excited exciton states to follow the 2D hydrogen series, with binding energies for the n-th given by [23]:

$$E_{b,n} = \frac{e^2 \mu_{ex}}{2\hbar^2 {\varepsilon_s}^2 (n - 1/2)^2}, \tag{2.3}$$

where ε_s is the dielectric constant that accounts for the screening of the Coulomb interactions. Indeed, excitons have been found to exhibit a Rydberg like series [27, 28], though the behavior deviates from such an ideal hydrogen model. As mentioned above the situation in 2D-materials is more complex. With field lines extending out of the two-dimensional limit, we can imagine that there is basically a part that is screened by the dielectric constant of the TMDC ε_{TMDC} and a part screened by the dielectric constant of the surroundings ε_{ext}. The electron-hole interaction is thus screened non-locally [27, 68, 69, 82]. This leads to the attractive potential deviating from a classical coulombic $V(r) \sim 1/(\varepsilon r)$ potential. As a consequence we can directly infer that different exciton states are also affected differently. With higher excited states having larger radii, their field lines will extend more into the surroundings. The consequence is that the part of the field lines screened by the dielectric surroundings becomes increasingly larger with higher principal quantum number, thus the overall screening being different for the different excited states. The parameter ε_s in eq. 2.3 therefore is not a constant in the two-dimensional limit. In order to take this non-local screening into account, it is

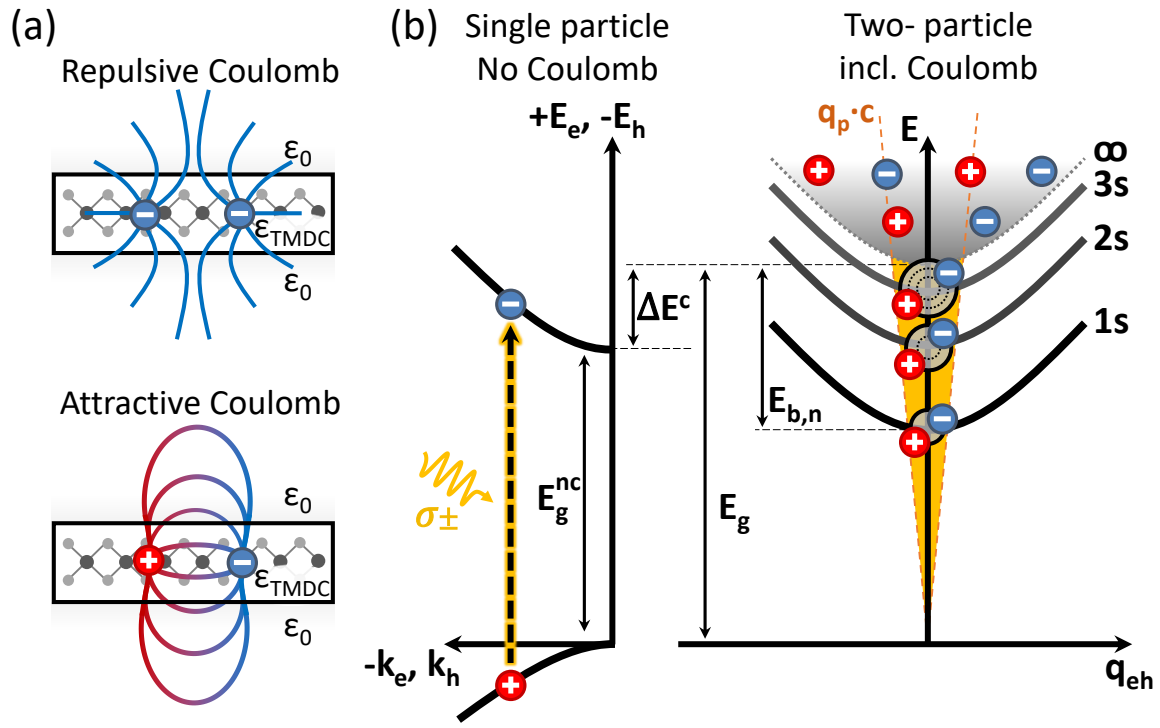

Figure 2.4: (a) Adapted from [27]. Illustration of charge carrier interactions in the two-dimensional limit due to coulombic forces, with field lines extending well outside the monolayer. (b) Left: Schematic, simplified band structure for TMDCs in a single-particle picture, explicitly excluding Coulomb interactions, where E_g^{nc} represents the bandgap without Coulomb interaction. An allowed optical excitation of an electron into conduction band, leaving a hole in the valence band, is exemplarily indicated. Right: Two-particle representation of optical excitations (forming excitons) when including Coulomb interactions with the x-axis being the two-particle center of mass momentum q_{eh}. The bandgap renormalizes to higher energies $E_g = E_g^{nc} + \Delta E^c$, with ΔE^c being the renormalization energy due to Coulomb interactions. Excitonic states are formed below the bandgap with the energy difference to the bandgap defined by their binding energies $E_{b,n}$. Yellow triangle represents the optically accessible transitions with an allowed momentum mismatch from the photon dispersion relation $\Delta q_{eh} \leq E_{photon}/c$.

common to use an approximation for $V(r)$ in form of a thin-film Coulomb potential in the ultra-thin limit [27, 28, 66, 67, 83]

$$V(r) = -\frac{e^2}{8\varepsilon_0 r_0}\left[H_0\left(\frac{\varepsilon_{ext} r}{r_0}\right) - Y_0\left(\frac{\varepsilon_{ext} r}{r_0}\right)\right]. \tag{2.4}$$

H_0 and Y_0 are the Struve and Neumann functions and ε_{ext} is the dielectric constant of the monolayer surroundings, while r_0 represents the characteristic length scale for the monolayer systems between 3 and 5 nm [69, 84]. It can also be expressed in form of the 2D polarizability χ_{2D} of the planar material as $r_0 = 2\pi\chi_{2D}$ and gives a crossover length where $V(r)$ scales as a classical $1/(\varepsilon_{ext} r)$ coulombic potential, with ε_{ext} as the

dielectric constant of the surroundings for $r > r_0$ and as log(r) for $r < r_0$ [68]. Under the assumption of such a thin-film potential, solving the Schrödinger equation then gives a way to obtain a model with a rescaled relation of eq. 2.3 to describe an excitonic Rydberg series with non-locally screened Coulomb interactions [27, 28].

Finally we focus on the lowest of these states, the A-exciton (from A-transition) ground state. In TMDCs this state exhibits extraordinarily high binding energies on the order of 0.5 eV, due to the reduced screening as well as comparably high masses and dominates the electro-optical properties of the materials even at room temperature [24, 85]. Considering the optical excitation of such an exciton with photons of energy $E_{photon} = E_g - E_{b,1s}$ and momentum $q_{photon} = E_{photon}/c$ from the photon dispersion relation, one finds that, due to momentum conservation, optically excited excitons can only have a center of mass momentum of $q_{eh} \leq q_{photon}$ [24]. Vice versa it constitutes that the recombination of a bright exciton, meaning an electron recombines with its hole under emission of a photon, has to fulfill the same momentum conserving conditions. Thus excitons can only undergo photoluminescent recombination when the electron and hole momentum mismatch can be compensated for by the photon momentum. The resulting consequence is known as the light cone (indicated by the shaded orange area in fig. 2.4 (b), right), a limitation from the photon dispersion relation, in which optically accessible excitons can be found [24].

Broadening of exciton resonances

From this understanding of excitonic states one could expect the resonances for excitons to be sharp delta-like functions, with the transition energy of the n-th state E_n defined by the state's binding energy and the renormalized bandgap energy as $E_n = E_g - E_{b,n}$. However, there are several mechanisms that can contribute to a broadening of excitonic resonances. Generally, these can be divided into the two sub-classes of homogeneous and inhomogeneous broadening.

First we can assume that upon excitation the polarization of all excitons is in phase due to being created by the same incident electromagnetic field. Now homogeneous broadening includes all effects that lead to a loss of polarization coherence of the excitons' oscillator, while the oscillator frequency, on the other hand, is not affected. Such a loss can be described by a specific coherence lifetime τ_p, the time after which $1/e$ exciton oscillators of the initial ensemble evolve still perfectly coherent in time, while the others have undergone a polarization coherence destroying event. Resulting from that the polarization coherence P is lost with time as $P(t) = P_0 \exp(-t/\tau_p)$ [23]. In turn, we can view this as a damping of the polarization coherence, that will lead to a spectral broadening of the exciton resonances with Lorentzian line shape. From another point

of view we can also understand this broadening in terms of the uncertainty principle. This tells us, the more precise the confinement of a periodical signal is in time, the less precise is the confinement in frequency space, which is interestingly also directly derived by a Fourier transform of the periodically evolving signal to frequency space for a given coherence lifetime.

The resulting broadening ΔE_{ex} in the exciton's spectral resonance, measured in its intensity broadening (where intensity $\propto$ polarization^2) due to purely homogeneous contributions, is then given by [23]

$$\Delta E_{ex} = \frac{\hbar}{\tau_p}. \tag{2.5}$$

Events that lead to such a disruption of the oscillators' periodicity can be of multiple origin. The most basic and fundamental one is that of radiative decay, when the oscillator is simply destroyed via bright recombination of electron and hole. It is a result of the finite lifetime of the exciton states inside the light cone and will therefore always contribute to the homogeneous broadening. For materials with high oscillator strength, such as TMDC monolayers, this can be particularly relevant, since here exciton lifetimes are commonly limited by rather short radiative lifetimes, on the order of ≤ 1 ps [86–90]. Such lifetimes will then constitute a broadening effect on the order of a few meV [91, 92], giving a theoretical limit for the observed linewidth known as radiative broadening. In realistic scenarios, however, there are scattering events that can occur on even faster time scales, depending on certain parameters, such as temperature, excitation density and sample quality.

These scattering events can be roughly divided into three different types of scattering. First, scattering with any lattice inhomogeneities including lattice defects, impurities, charge carriers from doping or interface roughness. Scattering events of this type are evidently due to non-intrinsic lattice inhomogeneities and are heavily influenced by the quality of the crystal. Second, scattering with other excitations, e.g., other excitons or excited free charge carriers. Here, scattering efficiency is simply dependent on the density of injected charge carriers and commonly requires high densities to have relevant effects. And third, inelastic scattering with lattice phonons, that is either absorption or emission of optic or acoustic phonons. Scattering under phonon absorption scales with the number of available phonons given by the phonon population. Since in a crystal lattice this population is temperature dependent, so will be the induced resonance broadening. This means that at sufficiently high temperatures this mechanism commonly dominates the overall broadening [23]. Note, however, that in general the scattering of phonons under emission is not strictly dependent on the availability of phonons. Thus the efficiency of these events is rather dependent on the availability of, and wave function overlap with the final state that is scattered into [92].

However, in real systems broadening of exciton resonances is often not purely homogeneous, but rather may also contain contributions from inhomogeneous broadening. This is understood in a frame of the exciton oscillators of a given ensemble not having an identical frequency. Again we can assume that initially all excited exciton oscillators are identical, however, due to certain conditions, like disorder (further discussed in sec. 2.3.2) the individual oscillators can relax and have slightly different frequencies depending on their surroundings. Such fluctuations in the frequencies then translate to slightly different emission energies, resulting in a broadened emission. Such inhomogeneous effects thus lead to a Gaussian line shape broadening, since also the distribution of frequencies is naturally given by a Gaussian distribution.

Dark excitons

Until now we have only covered the optically accessible, bright excitons. However, also so-called dark excitons, that may not be directly excited by incident light, can be formed when a system thermalizes, given their overall energy is comparable or lower than that of the bright species. In principle, two types of dark exciton states can be differentiated: Momentum-forbidden and spin-forbidden dark excitons [93–96]. In order to introduce these excitonic configurations, we shall again refer to a single-particle band structure, as depicted in fig. 2.3 for tungsten-based TMDCs. Although it shall be clearly stated that we can not fully cover binding energies in this picture due to their dependence on the reduced exciton mass (eq. 2.3), it gives an intuitive access to understanding the reasons for an exciton transition not being optically active.

The first species are those which do not fulfill momentum conservation as discussed above, meaning electron and hole have a momentum difference bigger than the photon dispersion at the given transition energy and can not recombine under the sole emission of light. Hence, these excitons are called momentum-forbidden. A common example in tungsten-based monolayers includes excitons formed from holes at K+/K- higher spin-split valence band, with the electron sitting in the opposite valley's (K-/K+) lower spin-split conduction band. Note that this transition would technically be allowed under selection rules, having the same quantum numbers as the optically allowed exciton in K+ valley (fig. 2.3 (b)). Additionally, in tungsten-based materials, another low lying momentum-forbidden dark exciton is theoretically predicted. This state is expected to form from holes in K± and electrons in the lower spin-split Λ± valleys. While in the single-particle band structure the three-fold degenerate Λ valleys are found to be higher in energy than the K valleys, electrons in these valleys also exhibit larger effective masses [56, 57, 97]. This leads to an increase of the binding energy, according to the relation of eq. 2.3, and can compensate for this energy offset, resulting in an

overall energetically favorable K − Λ exciton state, in contrast to the bright K−K state [93]. However, the exact energetic position of this excitonic state, estimated from band structure offsets, is not yet well defined and varies over 10's of meV between different calculations [56, 93, 98].

The second species of dark excitons include those, which do not fulfill spin conservation, accordingly called spin-forbidden excitons. These are excitons made up of an electron in conduction band with a different spin compared to its empty electron state in the valence band. For the example of tungsten-based TMDCs, these are excitons formed with an electron in the lower spin-split conduction band at K+/K- and the hole in the same valley's higher spin-split valence band. While this transition would be momentum-allowed, it is forbidden by selection rules. In this context though, we remark that these spin-forbidden dark excitons have an out-of-plane transition dipole moment and it has been shown that it is possible to directly probe these states via photoluminescent optical spectroscopy anyhow [63, 99, 100]. Finally, considering the dark states in tungsten-based materials that only include K−point contributions, we find that there excitons have an almost identical binding energy compared with the bright species, since the reduced effective exciton masses are very similar [35, 61]. As a consequence, these dark excitons are lower in energy than the bright states due to their electron always sitting in the lower spin-split band. In tungsten-based TMDC monolayers the energetically favorable exciton states are therefore dark.

Trions and other exciton complexes

In the context of excitons, referring back to the parallels to the concept of a hydrogen atom, we might further extend this analogy to the existence of other exciton complexes, comparable with, for example, $H^{\pm}$-ions or H_2 molecules. Indeed, such complexes have been found to stably form at low temperatures, where entropy arguments favor bound states over multiple individual states, even for rather low binding energies. The experimentally confirmed exciton complexes are depicted in fig. 2.5 (a) and charged complexes are only depicted in their negative form. These include trions, which are excitons with an additional charge (referred to as $X^{\pm}$) [29, 30, 101–105], biexcitons, which are two bound excitons (XX) [32, 106] and charged biexcitons - biexcitons with an additional charge ($XX^{\pm}$) [31, 33, 107]. The potential combinations to form such complexes increase with the number of involved particles, while at the same time becoming more and more intricate, where each individual charge can have multiple available valleys to occupy. To examine how such complexes are formed, we refer to a single-particle picture, using the example of the most basic exciton complex, the trion.

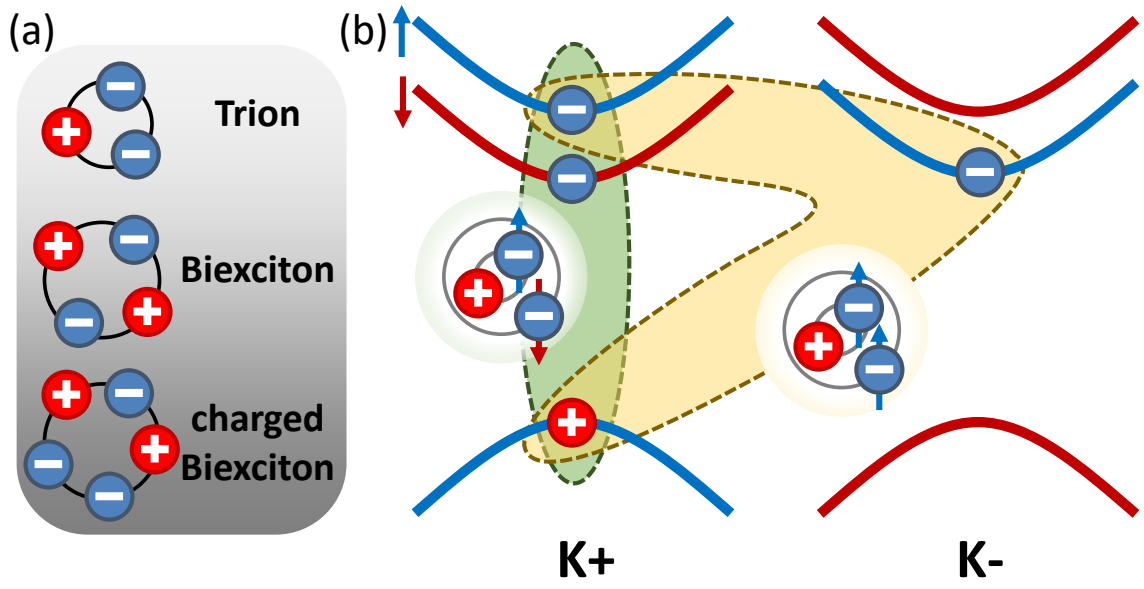

Figure 2.5: (a) Illustration of the experimentally confirmed exciton complexes. For simplicity, charged complexes are only included in their negative form. (b) Schematic of the bright trion formation in tungsten-based materials. Two different bright trion species exist, with an additional electron in one of the lower spin-split conduction band minimums of the K−valleys from doping. The resulting trions can either be in singlet (green) or triplet (yellow) spin configuration leading to different close range exchange interactions.

Depicted in fig. 2.5 (b) are the two possible configurations of electrons and holes forming the bright, negatively charged trion species in tungsten-based TMDCs. In principle, these trions are made up from a bright exciton, with an additional electron from doping sitting in the minimum of the conduction band at either K+ or K- lower, spin-split valley. The binding of an additional electron leads to the total binding energy of this complex being higher than that of a single exciton. This additional energy is the trion binding energy $E_b^{X^-}$ on the order of 30 meV [30, 69]. However, these two trion configurations are not energetically degenerate. As seen in fig. 2.5 (b), the trions can be differentiated by the spin of their second electron. The green complex shows the trion with two electrons of different spins, commonly referred to as the singlet trion. Depicted in yellow is the trion with identical electron spins, the triplet trion. This contrasting spin configuration results in a lifting of the energy degeneracy of the two species due to close range electron-electron exchange interaction, with a splitting on the order of 6 meV [103]. Also a dark trion with the two electrons sitting in each one of the lower spin-split conduction band valleys has been reported [108, 109]. Note, however, that two charges sitting in the same valley can never form an exciton complex, since they would have identical quantum numbers (Pauli exclusion principle).

As stated before, for biexcitons and charged biexcitons the possible configurations become progressively more complex, since more charges from various valleys can be involved in formation of these complexes. Therefore, a multitude of possible combinations exist, which are beyond the scope of this work and for a detailed analysis of this rather complex topic we refer to literature [32, 33, 106]. Here, we only include the binding energies for the observed optically bright complexes found in WSe_2 that are relevant for this work. The values are commonly given in form of the gain in total binding energy, as compared to the binding energy of a single ground state exciton, and for the neutral biexciton are found to be on the order of $E_b^{XX} \approx 20\,\mathrm{meV}$ [31, 104]. For the negatively charged biexciton, being a neutral biexciton combined with an additional electron, we get a binding energy of $E_b^{XX^-} \approx E_b^{XX} + E_b^{X^-} = 50\,\mathrm{meV}$ [31].

2.2 Excitons in high magnetic fields

In the first sections we have thoroughly introduced the concept of excitons and considered their pronounced importance in two-dimensional semiconductors. Now, in order to access fundamental properties of such bound electron-hole pairs, the study of excitonic resonance shifts in high magnetic fields has historically proven to be a suitable handle [42, 110–113]. In this context, it is important to note that multiple magnetic field induced effects contribute to an overall observed shift of the exciton resonances, which in turn allow to investigate different exciton properties. Here, the valley Zeeman effect allows to extract properties such as the exciton g-factor [54, 55, 65, 114–118], while diamagnetic shifts give access for the direct investigation of the exciton states' spatial extent [83, 110–112, 116]. Finally, an arising Landau level splitting at sufficiently high fields can also give rise to resonance shifts and allows estimates of properties such as the effective exciton mass [28, 119]. For this reason, understanding the origins of magneto-induced energy shifts is necessary in order to untangle the individual contributions and open a way to experimentally study the mentioned properties. With respect to that, the following sections provide a theoretical basis for the understanding of the different effects, whereas the main focus shall be on the valley Zeeman and diamagnetic shift effect. In addition, we briefly discuss the origin of an arising Landau level splitting that can affect exciton transition energies and give a limit for when this effect becomes of relevant magnitude.

2.2.1 Valley Zeeman effect

At first we discuss the valley Zeeman effect, which results in a linear splitting of exciton transition energies for bright excitons with different valley index when an external field is applied. To explain such a behavior, it is again helpful to refer to the single-particle band structure, as this effect, in a simplified way, can be understood as a combination of multiple single-particle effects. In this frame, we neglect the exciton binding energy and only consider shifts in the free-particle bandgap at the K$\pm-$points, assuming that exciton transition energies directly follow such shifts, since binding energies are not affected [65]. For this purpose, the band structure at the direct bandgap is depicted in fig. 2.6 (a) for a WS_2 monolayer. Shown are the two non-identical K+ and K- valleys and different spins are color coded in blue (up) and red (down). The dotted lines mark the valleys at zero field, while the solid lines are the shifted valleys due to an arbitrary magnetic field B>0. In an abridged model, we will consider three different mechanisms that lead to the depicted shift of the bands with applied magnetic field [65, 115].

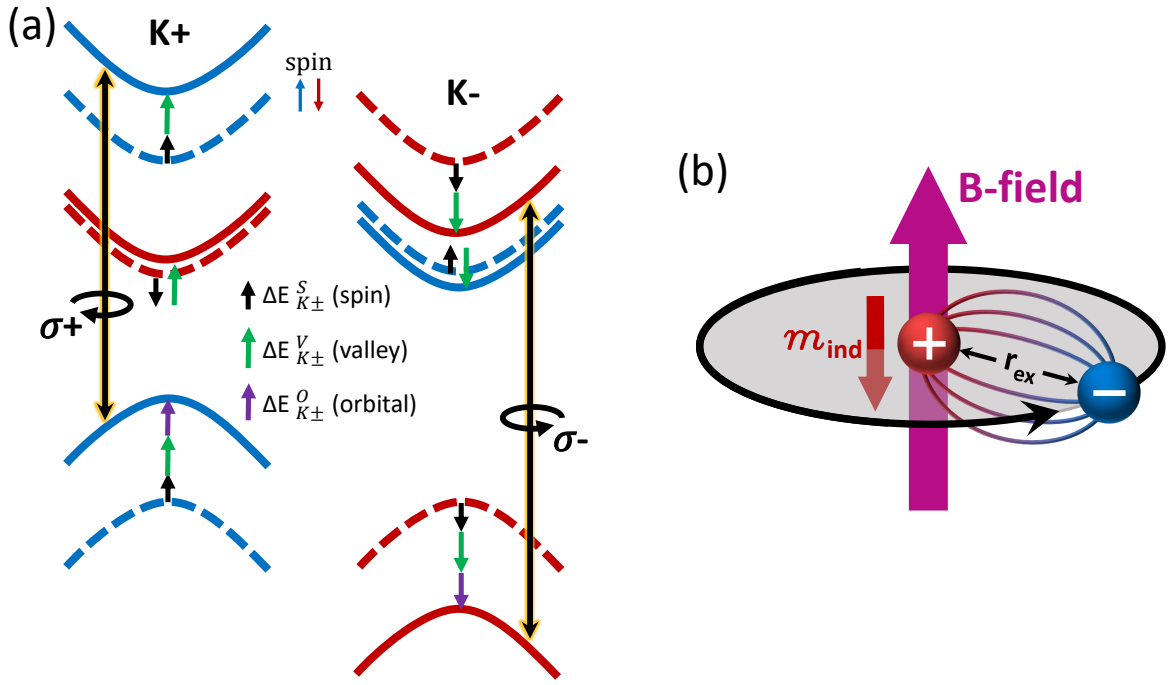

Figure 2.6: (a) Adapted from [65]. Schematic illustration of the WS_2 single-particle band structure at the K-points, where blue/red indicate spin up/down bands. Dotted lines represent the bands at zero field and solid lines the shifted bands due to an arbitrary external field B>0, while arrows indicate the individual contributions: spin $\Delta E^S_{K\pm}$ in black, valley $\Delta E^V_{K\pm}$ in green and orbital momentum $\Delta E^O_{K\pm}$ in purple. Optically allowed transitions are indicated for the lifted energy degeneracy between opposing valleys. (b) Illustration of the diamagnetic shift effect. An exciton is pinned at its hole and exposed to an arbitrary external magnetic field B. The electron's cyclotron motion creates an induced magnetic moment m_{ind}, anti-parallel to the external field.

Firstly, the well known Zeeman shift due to the electron spin (denoted by black arrows) leads to a shift of the bands, according to:

$$\Delta E^S_{K\pm} = sg\mu_B B. \tag{2.6}$$

Here, $s = \pm\frac{1}{2}$ denotes the spin quantum number, g is the electron g-factor, μ_B the Bohr magneton and B the applied magnetic field. Due to optically allowed excitations being spin conserving ($s_{VB} = s_{CB}$), the resulting shift for valence and conduction band are identical, resulting in the bandgap energy being unaffected [54, 55, 65].

Secondly, there is a contribution from the valley magnetic moment (denoted by green arrows). It follows:

$$\Delta E^V_{K\pm} = \alpha\tau\mu_B B, \tag{2.7}$$

where τ is the valley index ± 1, and $\alpha = m_0/m^*$ the valley g-factor with m^* being the effective masses in the respective bands [54, 65]. Since effective masses in both

conduction and valence band are very similar, according to $k \cdot p$ calculations [35, 61], the resulting shift is approximated as being the same for both bands, as well. Following from that, the valley magnetic moment also does, in a good approximation, lead to a change of the bandgap energy.

The third effect originates from contributions of the orbital magnetic moment (denoted by purple arrows):

$$\Delta E^{O}_{K\pm} = \mathrm{m}_l \mu_B B. \tag{2.8}$$

Here, m_l is the orbital's magnetic moment along the z-axis and, as described in sec. 2.1.2, is ± 2 in the K± valleys of the valence band and 0 in the conduction band. As a consequence, this magnetic shift is different for the two bands and leads to a net shift of the bandgap energy. Furthermore, since the sign of m_l is different for the two valleys, the shift is reversed in opposing valleys. Resulting from that, the degeneracy of the bandgap energy is lifted for the two K± valleys, which is expressed in a different exciton transition energy for $\sigma\pm$ polarized light, as follows from the selection rules in fig. 2.3.

Finally, we can write the valley Zeeman shift for the change in transition energy in individual valleys K± in analogy to the classical Zeeman shift as:

$$\Delta E^{vZ}_{K\pm} = \frac{\tau}{2} g^{vZ} \mu_B B, \tag{2.9}$$

where g^{vZ} denotes the valley Zeeman g-factor. From the individual contributions, as discussed above, this total magnetic field induced energy shift of the transition energies is dominated by contributions from the orbital magnetic moment. Following from that, the valley Zeeman g-factor is expected to be in the range of $g^{vZ} \approx -4$, with slight deviations due to minor differences in effective masses, neglected in the above-mentioned approximation of the orbital momentum contribution [120].

2.2.2 Diamagnetic shift

In contrary to the valley Zeeman effect, the resonance shift from diamagnetic effects can be covered in a fully excitonic picture and is most intuitively understood in the classical frame of an electron moving around its hole in a circular motion. Let us therefor fix the hole at an arbitrary point as depicted in fig. 2.6 (b). An external magnetic field then leads to the electron cyclotron motion aligning perpendicular to this field with a given cyclotron frequency $\omega = eB/m_e$, depending on the electron mass m_e, the applied field B, and the elemental charge e. This will in return create an induced magnetic moment $m_{ind} = e \langle r^2 \rangle \omega/2$, anti-parallel to the external field with $\langle r^2 \rangle$ being the mean squared radius of the circular motion. The result is a shift in the exciton's transition energy with $\Delta E = m_{ind} B$. The magnitude of this shift will hence directly depend on the radius

of the electron's circular motion. In the weak-field limit (further discussed in the next section), where other magnetic field induced effects are small compared to the exciton binding energy, this radius is equivalent to the average electron hole separation, or in other words, the exciton size. If we now consider the exciton's effective reduced mass and the two-dimensional character of the system, a full quantum mechanical treatment of the diamagnetic shift yields the quadratic field dependence of the energy shift [121–123]

$$\Delta E_n^{Dia} = \frac{e^2 \langle {r_n}^2 \rangle}{8\mu_{ex}} B^2 = \sigma_n B^2. \tag{2.10}$$

Here, $\langle r_n^2 \rangle$ is the exciton's mean squared radius for the n-th state and μ_{ex} its reduced effective mass, while σ_n is commonly introduced as the diamagnetic shift parameter. Note that the energy shift due to this effect is always positive, regardless of the applied field or investigated valley the exciton resides in. Additionally, from eq. 2.10, we find that the diamagnetic shift scales with the square of the exciton radius. As a result, this effect becomes stronger with increasing principal quantum number n of the exciton state, since higher excited states have a larger spatial extent.

The exciton mean squared radius in 2D is defined by $\Psi_n(r)$, its radial exciton wave function, as $\langle r_n^2 \rangle = \langle \Psi_n | r^2 | \Psi_n \rangle = 2\pi \int_0^\infty r^2 |\Psi_n|^2 r dr$. The spatial measure of an exciton in its n-th state is then characterized by its root mean square (rms) radius $\sqrt{\langle r_n^2 \rangle}$. Note that this rms is not equivalent to the Bohr radius a_B, which is often used to give estimates of exciton sizes. For a conventional 3D hydrogen wave function, this Bohr radius a_B^{3D} is defined as the peak of the radial probability function $2\pi r |\Psi_n(r)|^2$ for the ground state and is equivalent to the exponential parameter a_0^{3D} in the wave function. In contrast to that, in a 2D hydrogenic 1/r potential the Bohr radius is given as $a_B^{2D} = a_0^{2D}/2$. The rms radius of the ground state is related to this Bohr radius in the 2D case as $rms = \sqrt{6}\, a_B^{2D}$ [124].

2.2.3 Landau level splitting

As briefly mentioned before, the quadratic shift of the exciton resonances depending on the exciton radius is only valid in the weak-field limit, or more precisely, for fields in which the exciton binding energy is large compared to the cyclotron energy $E_{cyclotron} = \hbar\omega = \hbar e B/\mu_{ex}$ [111, 113, 125, 126]. At the breakdown of this approximation, where these energies become of similar magnitude, one can imagine that the charges will progressively be forced onto specific cyclotron orbits. The reason for that is the appearance of quantized Landau levels in valence and conduction band, in which optical transitions occur when applying a sufficiently high magnetic field [127–129]. This is schematically shown in fig. 2.7 (a), including the allowed optical transitions between

Landau levels denoted by N_i, for both valleys. Note that there is a 0-th Landau level pinned to the conduction bandedge in K+ and to the valence bandedge in K- valley [28, 130].

The optically allowed transition energies between discrete Landau levels are given by $\Delta E_N = (N - 1/2)\hbar eB/m_{ex}$, where N is an integer number and the splitting between adjacent Landau levels $\Delta E_{LL} = E_{cyclotron}/2$ (for a detailed analysis see refs. [28, 130]). To give a more intuitive understanding of the consequences for the excitonic transitions, let us consider the two-particle picture of excitons introduced in sec. 2.1.3, depicted in fig. 2.7 (b) for an arbitrary applied external field. Here, assuming a sufficiently high external field, also the excitonic transitions become quantized. In a simple picture, one can imagine that for low fields, where also the splitting between Landau levels is small, there is a multitude of allowed Landau level transitions for each excitonic transition, or in other words, still the majority of states in k-space can contribute to exciton formations. Therefore, effects of this quantization are negligible in the weak-field limit.

However, with increasing field and subsequently increasing energy spacing between Landau level allow transitions, less and less of these transitions are available for each excitonic state. This can be interpreted as the charges being forced on defined cyclotron orbits, as stated above. The excitonic character, where all states of the bands in k-

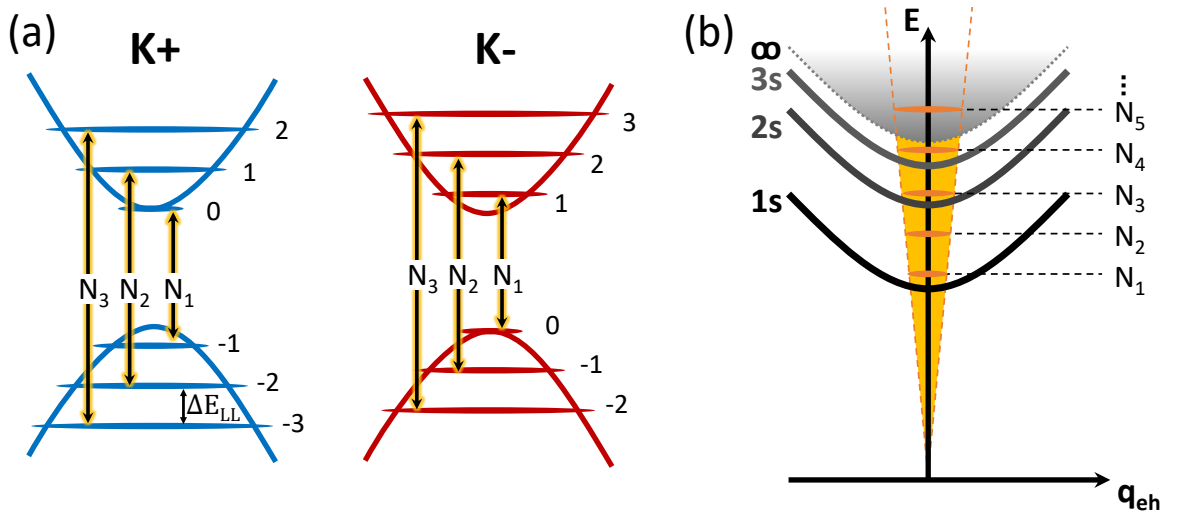

Figure 2.7: (a) Schematic illustration of the appearance of discrete Landau levels in valence and conduction band of K± valleys under an external field. Optically allowed transitions are found between Landau levels with index -$(i+1) \leftrightarrow i$. The 0-th Landau level is pinned to the conduction band minimum (valence band maximum) in K+ (K-) valley. (b) Resulting simplified two-particle picture of quantized excitonic states. The illustration visualizes the transition from quadratic to linear regime for $\Delta E_{LL} \sim E_{b,n}$ when the splitting between Landau transitions is on the same order as the n-th exciton state's binding energy.

space can contribute to an exciton formation, is progressively lost. This reaches its extreme when basically no more optically allowed transitions, given by Landau levels, are available for an excitonic state, that is $\Delta E_{LL} > E_{b,n}$. Optically allowed transitions are then only given by the splitting between Landau levels and will therefore scale linearly with magnetic field. Note, however, that the transition between quadratic and linear regime is a smooth one and, considering the high binding energies in TMDC monolayers, it requires extreme magnitudes of magnetic fields for this effect to be significant [28]. As an example, even for 100 T the cyclotron energy in a TMDC monolayer is on the order of only ∼50 meV, compared to a 1s binding energy of a few 100's of meV. Thus, in realizable experimental settings, this effect can only be found to affect higher excited states, where binding energies are reduced. Interestingly, in such a case, one can directly estimate the exciton's reduced effective mass [28, 119], due to the linear behavior of the Landau level splitting. However, we again emphasize that the above described model of a quadratic diamagnetic shift is only applicable, when staying well within the limits of the weak-field approximation.

2.3 Environmental sensitivity of exciton properties

We have already discussed the importance of coulombic forces between charges in TMDC monolayers due to its enhancements from reduced dielectric screening in two dimensions in sec. 2.1.3. Yet, so far only the idealized case of the surroundings providing a perfectly homogeneous dielectric constant has been addressed. In reality, this is hardly the case. The consequences of the environment deviating from this theoretical ideal shall be introduced in the following sections in more detail.

2.3.1 Effects of dielectric screening on exciton states

Let us first consider a scenario where the dielectric surroundings are still homogeneous but can take on different values. From the general scaling of binding energies in eq. 2.3 we can infer that the strength of the Coulomb interactions for each exciton state is proportional to ${\varepsilon_{ext}}^{-2}$ (and conversely, the dielectric screening $\propto {\varepsilon_{ext}}^{2}$). As mentioned above, a change in the Coulomb interaction strength has direct implications not only for exciton binding energies, but also for the bandedge energy. Fig. 2.8 (a) shows theoretically calculated transition energies for the bandgap, as well as the exciton ground (1s) and first excited (2s) states as a function of the Coulomb interaction strength. Here, a non-locally screened thin-film potential of eq. 2.4 for the calculations of the exciton binding energies is assumed (for details see. ref. [131]). In the case of the Coulomb interaction strength being zero, we reach a point where bandgap and exciton transition energies merge. In this trivial case, as mentioned above, no excitons would be formed and the bandgap would reach its theoretical minimum. Accordingly, for an increasing Coulomb interaction strength the bandedge shifts to higher energies. We can understand this in a frame, where an electron that is excited above the bandedge, will then 'feel' the repulsive presence of other electrons. With increasing Coulomb interaction strength, this repulsive force, known as the self energy contribution, will consequently lead to an increase of the energy needed to excite a single electron above the bandedge, or in other words, the quasi-particle bandgap becomes larger [23, 24].

It can be seen, however, that the exciton ground state is hardly affected by that. This is due to the enhanced Coulomb interaction strength also leading to a gain in the exciton binding energy. Resulting from that, the bandgap shift and the increase in binding energy for the 1s state largely compensate each other, leading to only a minor overall shift for the 1s ground state. For higher excited states, this is different, as is exemplary shown for the 2s state. Since the binding energy of the 2s state is lower than that of the 1s state to begin with, the bandgap shift is also compensated for less effectively. Therefore, the 2s transition energy is more strongly depended on the shift of the bandgap.

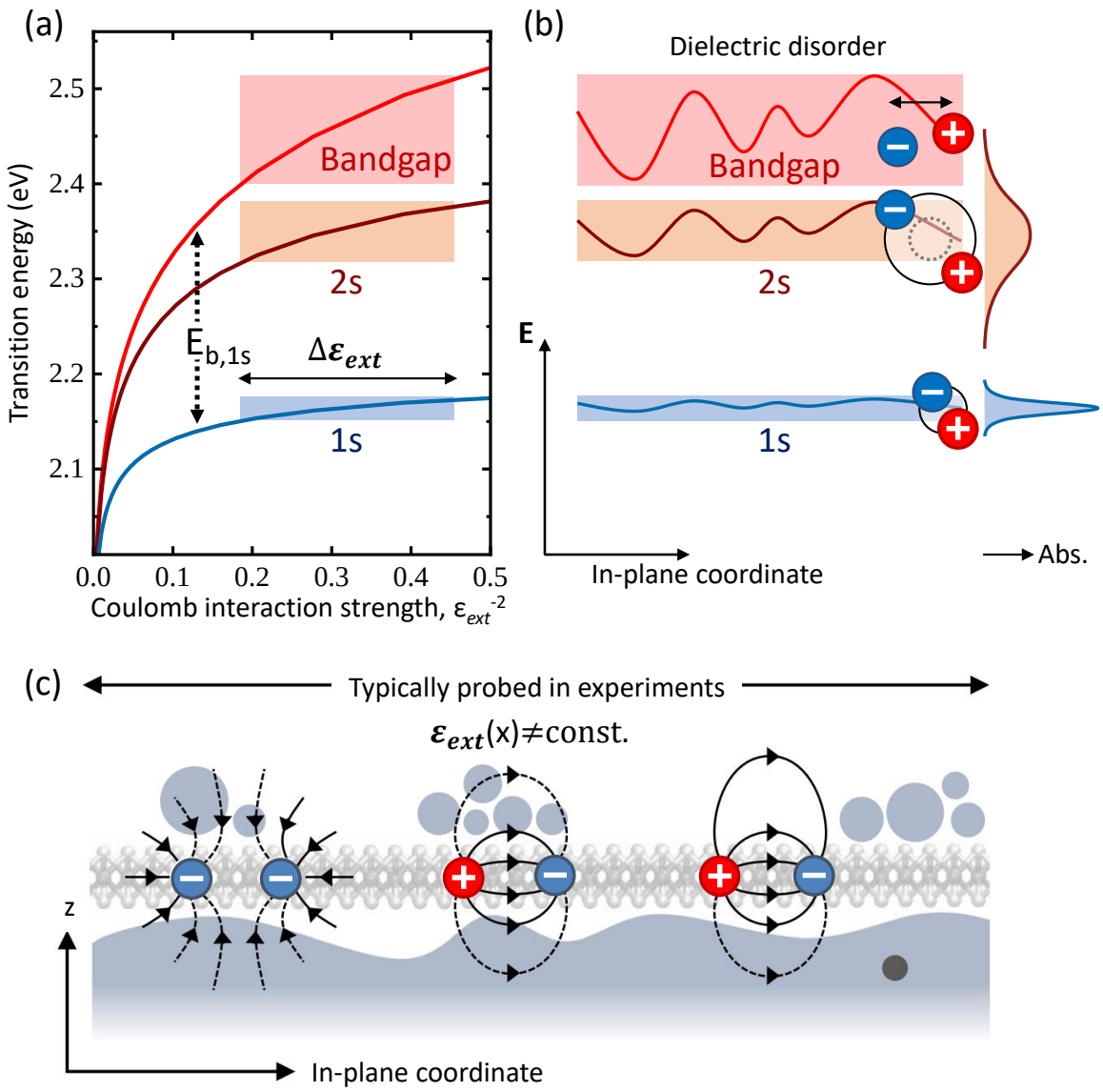

Figure 2.8: Adapted from [132]. (a) Theoretically calculated change of transition energies for 1s/2s state and the bandgap in WS_2 as a function of increasing Coulomb interaction strength, represented as the inverse square root of the dielectric constant. A binding energy of the 1s state for an arbitrary value of ε_{ext} is exemplarily included. Colored areas indicate fluctuations of the dielectric constant $\Delta\varepsilon_{ext}$ due to changes in the environment. (b) Expected spatial dependent fluctuations of the transition energies due to fluctuations in the dielectric constant. Also shown is the resulting non-equivalent inhomogeneous broadening of the 1s and 2s resonances in the absorption. (c) Schematic real space representation of charge carrier interactions in a TMDC monolayer subjected to a non-homogeneous environment, as it is commonly found under realistic conditions.

From this argumentation infers that exciton transition energies, as a function of dielectric screening strength, will behave more and more 'bandgap-like' with increasing principal quantum number, as their binding energy progressively decreases.

We convey that changes in the local dielectric environment of two dimensional semiconductors constitute significant changes in exciton binding, as well as bandgap energies. These changes can be on the order of a few 100's of meV, in the typical range of Coulomb related interaction energies [24, 85, 131, 133]. Controlling of the dielectric constant from the direct surroundings therefore opens up ways to significantly influence the bandgap and exciton transition energies in these two-dimensional semiconductor materials, as has been reported in literature [71, 134, 135]. However, this dielectric screening effect has further implications for structures realized in experiment, since systems fabricated from two dimensional materials commonly do not have a perfectly homogeneous environment, as was assumed so far. In this case, introduced inhomogeneities lead to the dielectric constant becoming a function of the spacial in-plane coordinate and the resulting consequences for an investigated exciton ensemble shall be discussed in the following.

2.3.2 Dielectric environment as a source of disorder

A more realistic picture of a monolayer's surroundings, as found under experimental conditions, is schematically illustrated in fig. 2.8 (a). As shown, monolayer structures are commonly far from the idealized system we considered before. They hardly ever have a perfectly flat or chemically pure interface contact [136], but rather are exposed to a number of surface inhomogeneities, which include adsorbed particles or fluids, roughness of the underlying substrate or polarizable defects [137]. This in turn leads to local fluctuations in the dielectric surroundings, referred to as dielectric disorder [132]. Such fluctuations of the dielectric constant $\Delta\varepsilon_{ext}$ are indicated in fig. 2.8 (a) by shaded areas for the two exciton states and the bandedge. The direct consequence is further illustrated in fig. 2.8 (b). Depending on the local variation of the dielectric constant, the transition energies will exhibit fluctuations. For the same reasons as discussed before, these fluctuations are strongest for the bandgap and less significant for excitons with decreasing principal quantum number. We can expect this to have direct consequences for the emission from excitonic resonances in experimental settings, since the obtained signal is an average over a multitude of excitons with different spatial coordinates. As for any effects associated with static disorder, it is important to distinguish two different situations. One where the fluctuations of disorder are much smaller than the area of interest and one where the fluctuations are on a bigger scale. Given that experimentally probed areas are commonly on the order of $\sim$1 μm, we refer to these as nanoscale and microscale disorder respectively.

First, we consider the case of a setting with only nanoscale disorder. Here, excitons in the probed area can have differing dielectric surroundings, depending on their spatial

coordinate. Since the transition energy of each exciton is closely coupled to its direct dielectric environment, these fluctuations also prompt variations of the resonance energies in the exciton ensemble. However, all of these excitons inside the probed area will contribute equally to the overall observed emission. This means that multiple individual energetic resonances with slightly different oscillator frequencies are overlain, resulting in an inhomogeneous broadening of the signal, as discussed in sec. 2.1.3. Since the shift in resonance energies from dielectric effects is stronger for higher excited states than for the ground state, this broadening is expected to be substantially more pronounced for higher excited states, indicated in the right of fig. 2.8 (b). Note that in this scenario, where the disorder scale is much smaller than the area of interest, a second implication follows. It can be assumed that the average dielectric constant $\overline{\varepsilon}_{ext}$ is representative for the whole system. This means that for two probed regions, at different positions x_1 and x_2, the average dielectric constant is the same ($\overline{\varepsilon}^{x_1}_{ext} = \overline{\varepsilon}^{x_2}_{ext}$). As a consequence of that, the absolute energy positions of the individual resonances should not be affected by disorder on the nanoscale, regardless of the probed position.

Now we consider a scenario of microscale disorder, where fluctuations in the dielectric surroundings are of significantly bigger scale than the area of interest. For simplicity it is assumed that here, the dielectric disorder on the nanoscale is negligible, implying that the average dielectric constant of a probed area is the same as for each point inside this area ($\overline{\varepsilon}^{x}_{ext} = \varepsilon^{x}_{ext}$). Now it has to be considered that two probed ares at different positions x_1 and x_2 have different dielectric environments, meaning $\varepsilon^{x_1}_{ext} \neq \varepsilon^{x_2}_{ext}$. The resulting consequence is the exact opposite of the previous setting. Here, the absolute transition energy of the individual resonances will be different for the two positions, while the linewidth, on the other hand, are expected to be identical, since broadening from nanoscale disorder is absent. Yet again, this energetic shift in the resonance energies, originating from different dielectrics, is expected to be more pronounced for higher lying states than for the ground state. Note, however, that while we have considered the different disorder scales separately, this does not have to be the case in real systems and contributions from both nano- and microscale disorder could be concurrent. In the presence of dielectric disorder, the obtained excitonic response of a two-dimensional structure can thus be expected to be influenced both in their energetic positions (on a microscale), as well as in their linewidth [132, 135].

2.4 Exciton Propagation

In the previous section we have introduced the concept that excitons can have different properties depending on their local in-plane coordinate. From there, it is not far fetched to turn to the fact that excitons in TMDC monolayers are additionally free to move in their two dimensional limits [39, 40, 138], in close analogy to classical quantum well systems [139–142]. In the following section we shall first introduce the classical model of particles propagating along a density gradient in a diffusive process, governed by scattering events, for the specific case of excitons. Then we will focus on a limiting case where such a model of purely excitonic propagation of electron-hole pairs breaks down, namely when the excited charge carrier system is no longer dominated by exciton formation, but also contains sizable parts of free charge carriers. To account for such a scenario, a model of compound diffusion is introduced, where the concurrent propagation of electron-hole pairs as free charge carriers and excitons is covered.

2.4.1 Diffusive propagation of excitons

In the frame of this work we consider the diffusion-like propagation of excitons along a well defined density gradient. The diffusion is a result of the fundamental second law of thermodynamics and described by Fick's second law of diffusion in two dimensions according to:

$$\frac{\partial n(\vec{x},t)}{\partial t} = D\Delta n(\vec{x},t). \tag{2.11}$$

Here, $n(\vec{x},t)$ is the two-dimensional density profile of the diffusing species as a function of its in-plane spatial coordinate $\vec{x}$ as well as time t and $\Delta n(\vec{x})$ is the generalized second derivative of the same with respect to its spatial coordinate. D then is the characteristic diffusion coefficient, an intrinsic material property that describes how efficient a particle diffuses in the given system. To give a more intuitive understanding of eq. 2.11, let us analyze the example of a two dimensional centrosymmetric Gauss distribution $n(\vec{x},t_0) = exp\left(-\frac{|\vec{x}-\vec{x_0}|^2}{w(t_0)^2}\right)$, with $|\vec{x}-\vec{x_0}|^2$ as the square of the Euclidean norm, where $\vec{x_0}$ is the center of the Gauss and $w(t_0) = w_{x_1}(t_0) = w_{x_2}(t_0)$ its centrosymmetric width at time t_0. The solution of Fick's second law for such a density profile is closely related to its fundamental solution and the density evolution with time is given by:

$$n(\vec{x},t) \sim exp\left(-\frac{|\vec{x}-\vec{x_0}|^2}{w(t_0)^2+4Dt}\right), \tag{2.12}$$

where factors for normalization of the Gauss profile are omitted for simplicity. From this we find that diffusive processes lead to a broadening of the Gauss profile with time according to $w(t)^2 = w(t_0)^2 + 4Dt$. More generally speaking, we find that the diffusion

is directed to flatten the gradient in the density, whereas the diffusion coefficient is a measurement of how efficient this process is.

In order to understand what properties and mechanisms influence this diffusion coefficient, let us refer to a more specific picture of a diffusion process for a single exciton governed by scattering events, as schematically illustrated in fig. 2.9. An exciton is excited at time t_0 and spatial coordinate $\vec{x_0}$ and propagates while scattering with potentials, until it recombines under emission of light at time t and at spatial coordinate $\vec{x}$. The average time that passes between two scattering events is the characteristic scattering time τ_s and the distance traveled is the exciton's mean free path l_{free}. Note that these two parameters are directly coupled via the exciton's kinetic energy. The overall

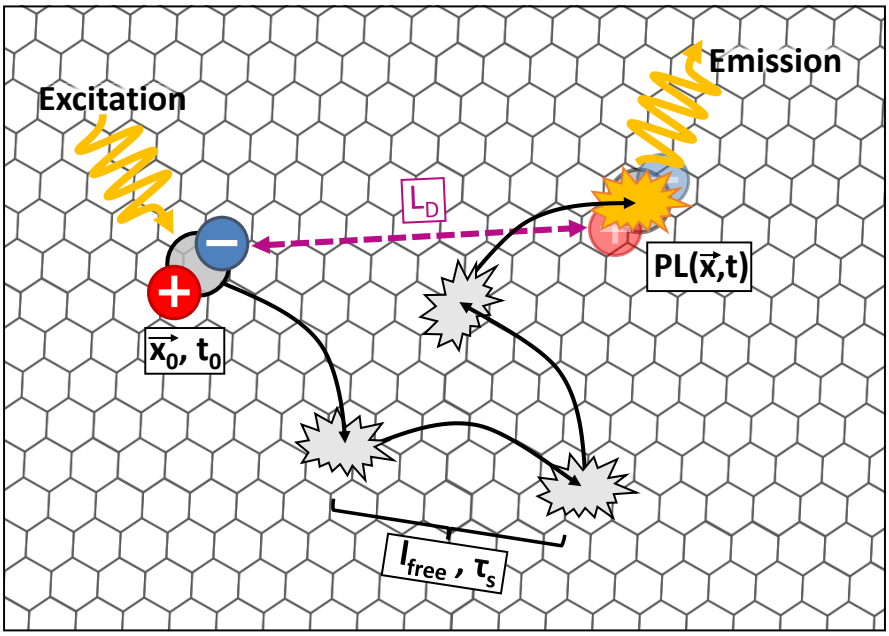

Figure 2.9: Illustration of exciton propagation in TMDC monolayers (lattice is not to scale). An exciton is excited at time t_0 and in-plane spacial coordinate $\vec{x_0}$. It travels in a scattering process, until it recombines under photoluminescent emission after time t and at spatial coordinate $\vec{x}$. The mean free path between two scattering events is denoted by l_{free} and the average scattering time by τ_s. The distance an exciton travels this way is the diffusion length L_D (magenta).

average distance that an exciton can cover this way is the diffusion length $L_D = |\vec{x} - \vec{x_0}|$ and the average time that an exciton can propagate in the material is related to its lifetime τ. Note that this lifetime is commonly defined as the time it takes for an ensemble to decay to $1/e$ of the size it was initially created with. In two dimensions these two parameters are related to the diffusion coefficient by

$$L_D = 2\sqrt{D\tau}, \tag{2.13}$$

as can be directly defined from eq. 2.12 [40, 143–145]. Note, however, that the definition of the diffusion length is also often found with the factor of 2 left out [39, 138, 146].

Now, if we consider this finite lifetime of diffusing excitons in our systems, we can readily extend eq. 2.11 to yield a more specific form of an exciton ensemble's spatial density evolution with time:

$$\frac{\partial n_{ex}(\vec{x},t)}{\partial t} = D\Delta n_{ex}(\vec{x},t) - \frac{n_{ex}(\vec{x},t)}{\tau}, \tag{2.14}$$

where the additional term describes the decay of excitons due to their finite lifetime τ and $n_{ex}(\vec{x},t)$ now is the time and position dependent exciton density. Here, we also find a limiting case for when propagation in an excitonic system can be described by a diffusive process. In a scenario where this lifetime approaches similar orders as the scattering time τ_s, the scattering events that an exciton undergoes during its lifetime become fewer and fewer. In the limit of the scattering time overcoming the excitons' lifetime, meaning $\tau_s > \tau$, we reach the regime of ballistic transport, where, on average, an exciton does no longer scatter at all, but rather propagates unhindered. The mean free path then becomes equal to the exciton's average propagation length during its given lifetime, that is $l_{free} = L_D$. In such a situation we therefore also find a breakdown of the validity of describing propagation with a diffusion-like model.

Another fundamental limitation for its applicability is given by the de Broglie wavelength, describing the wave-particle duality of the excitonic quasi-particles. For the here considered excitons it is given as

$$\lambda = \frac{h}{\sqrt{2k_B T M_{ex}}}, \tag{2.15}$$

where $\sqrt{2k_B T M_{ex}}$ is the impulse of an exciton with total mass M_{ex} and its kinetic energy defined by the exciton temperature T. Here it has to be considered that, in order to employ a classical diffusion model as detailed above, this wavelength should generally be smaller than the exciton's mean free path, so that the propagating exciton is at any point described as a well defined matter wave. Finally, when both of these conditions are fulfilled and such a model is applicable, the efficiency of the diffusive propagation in an excitonic system is given by the Einstein relation [138, 143, 147]. Assuming the excitons' kinetic energy is defined by the exciton temperature T this yields:

$$D = \frac{k_B T \tau_s}{M_{ex}}, \tag{2.16}$$

with, k_B as the Boltzmann constant and M_{ex} as the total exciton mass. We then find that for an exciton system in thermal equilibrium ($T = \text{const}$), the diffusion coefficient

is defined by the excitons' scatterings time τ_s, or in other words, by how often scattering events occur.

2.4.2 Saha equilibrium of charge carriers

In the previous section the diffusive propagation of electron-hole pairs has been analyzed for electron and holes bound in quasi-particle exciton states. While, due to the high exciton binding energies in TMDC monolayers [24], electrons and holes are commonly assumed to form excitons, there are also scenarios where they can exist as unbound, free charge carriers. One such scenario is found in the high density regime, above the well known Mott transition. Due to strong screening effects and Pauli blocking, instead of excitons, a dens electron-hole plasma is formed [148–151]. Interestingly, also in the limit of very low densities the formation of excitons is suppressed in the favor of free charge carriers. This phenomenon can be understood from a thermodynamical point of view within the need for minimization of the free energy of a system in thermal equilibrium, defined as $F = U - TS$. Here, U is the internal energy that corresponds to the energy gained by forming a bound state and therefore $U \propto -E_b$, with the exciton density n and binding energy E_b (note that here the binding energy is defined as an absolute value and the minus sign then indicates that the formation of a bound state is a way of lowering the internal energy of the system). T is the temperature in equilibrium and S the entropy of the system. This entropy is higher for free charge carriers due to a larger number of available states the system can be in. Consequently, at high temperatures and low densities, the entropy term can become dominant, resulting in the free charge carriers becoming the preferable state and leading to ionization of excitons. This is known as entropy ionization [152].

Let us now turn to the more specific case of tungsten-based TMDC materials. The free energy of the system can be derived, assuming that electrons and holes as well as excitons at room temperature and at low densities behave as ideal gases and neglecting any Coulomb renormalization effects. Note that all relevant states that can be occupied by electrons and holes, given by the band structure, have to be included. For tungsten-based materials these include states at the K± and Λ± points. The free energy for an undoped system then yields [153]:

$$F = \sum_p n_p k_B T \left(ln \frac{n_p}{D_p k_B T} - 1 \right) + n_p E_p. \tag{2.17}$$

Here, n_p denotes the density of the n-th type of particle (electron, hole and exciton) and additionally runs through all relevant valley indices for the considered particle. E_p then denotes the relative energies for the given state from band offsets or binding energies.

D_p are the density of states:

$$D_p = g_p \frac{m_p}{2\pi\hbar^2}, \tag{2.18}$$

with the respective effective mass m_p and the degeneracy of the states g_p. Considering an undoped system, the total number of any free electrons n_e^{tot} and holes n_h^{tot} is always the same, regardless of their valley index (we simply sum over all states). This is due to both exciton ionization and exciton formation either producing or destroying exactly one of each species at the same time. Furthermore, the photo-injection of charge carriers also produces electrons and holes in pairs and therefore

$$n_e^{tot} = n_h^{tot}. \tag{2.19}$$

From that we can use the total number of free electrons or holes $n_{e/h}^{tot}$ and the total number of excitons that are formed n_{ex}^{tot} (again regardless of their valley index) to relate the number of total injected electron-hole pairs in the system N_{tot} as

$$N_{tot} = n_{ex}^{tot} + n_{e/h}^{tot}. \tag{2.20}$$

Using these two conditions and introducing Lagrange parameters to minimize energy, one yields from eq. 2.17 the Saha ionization equation (also known as mass action law):

$$\frac{n_e^{tot} n_h^{tot}}{n_{ex}^{tot}} = S, \tag{2.21}$$

where S is the Saha parameter, defined by the relative energies and density of all available states for excitons and free charge carriers, as well as the temperature of the system (for a detailed derivation see [153]). Again, taking into account the condition from eq. 2.19 and defining the exciton fraction in the system to be $\alpha_{ex} = n_{ex}^{tot}/N_{tot}$, we can express this fraction as function of the Saha parameter and the total injected electron-hole pairs in the form:

$$\alpha_{ex} = 1 + \frac{S}{2N_{tot}} - \sqrt{\left(\frac{S}{2N_{tot}}\right)^2 + \frac{S}{N_{tot}}}. \tag{2.22}$$

This confirms the above stated density dependence of the exciton fraction. If we let $N_{tot} \to \infty$, in the limit of high injected exciton-hole densities, it readily follows that $\alpha_{ex} \to 1$, meaning the system will approach a state where all electrons and holes are bound as excitons. Nevertheless, as stated above, theoretical calculations show that the Mott density gives an upper limit of about $N_{tot} \sim 10^{12} - 10^{13} cm^{-1}$ where excitons can be formed [150]. In the other case of low densities, where $N_{tot} \to 0$, we find that

also $\alpha_{ex} \to 0$. In this case, formation of free charge carriers will be favored over the formation of excitons.

Since excitons and free charge carriers in general do not have the same diffusion coefficients [144], this equilibrium of excitons and free charge carriers can have major implications for transport phenomena in TMDC monolayer systems, depending on the injected electron-hole pair density and temperature. In a sufficiently high density regime, transport of charges can indeed be expected to be of purely excitonic nature. In contrary to that, however, at considerably low densities, where exciton formation is fully suppressed, transport is then expected to be fully driven by free charge carriers. In between those two regimes, where free charge carriers and excitons coexist, an averaged diffusion coefficient from concurrent contributions of excitons and free charge carriers should be expected. Note that while the position of this regime generally is a function of the injected electron-hole pair density, the equilibrium conditions are also strongly dependent on the system's temperature [150]. In the following we give a more detailed analysis of the expected diffusion dynamics in the regime of coexisting excitons and free charge carriers, where a compound diffusion of both populations is expected.

2.4.3 Coupled exciton-plasma diffusion

For the theoretical modeling of a compound diffusion of excitons and plasma we consider two coupled diffusion equations, one for the total exciton density n_{ex}^{tot} and one for the total density of the electron-hole plasma n_{eh}^{tot}. Note that the free charge carriers of the plasma can also be described as pairs of electrons and holes, since on average they should diffuse together in order to conserve electro-neutrality. We thus yield:

$$\frac{\partial n_{ex}^{tot}}{\partial t} = D_{ex}\Delta n_{ex}^{tot} + D'_{ex}\Delta n_{eh}^{tot} - \frac{n_{ex}^{tot}}{\tau_{ex}} - \frac{n_{ex}^{tot} - \nu_{ex} n_{eh}^{tot}}{\tau_i}, \tag{2.23a}$$

$$\frac{\partial n_{eh}^{tot}}{\partial t} = D_{eh}\Delta n_{eh}^{tot} + D'_{eh}\Delta n_{ex}^{tot} - \frac{n_{eh}^{tot}}{\tau_{eh}} + \frac{n_{ex}^{tot} - \nu_{ex} n_{eh}^{tot}}{\tau_i}. \tag{2.23b}$$

Here, the first and third term are analogous to eq. 2.14, while D_{ex} and D_{eh} denote the different diffusion coefficients for excitons and the electron-hole plasma (free charge carriers) respectively. In the same manner, τ_{ex} and τ_{eh} are the recombination lifetimes of excitons and electron-hole pairs in the plasma. D'_{ex} and D'_{eh} denote the respective trans-diffusion coefficients, meaning the second term covers diffusion of excitons driven by a gradient in the plasma and vice versa. Finally, the fourth term describes the change in density of excitons (or plasma) in order to sustain the Saha equilibrium, with the ionization rate τ_i and $\nu_{ex} = n_{ex}^{eq}/n_{eh}^{eq}$ as the ratio of total exciton density to total density of free electron-hole pairs, as given by the Saha equation in thermal equilibrium.

For simplicity we first assume that the densities of excitons and plasma are sufficiently small to neglect contributions of currents driven by trans-diffusion, and thus set $D'_{ex} = D'_{eh} = 0$. Furthermore, the sustainment of the Saha equilibrium by ionization has to be considered to be faster than the overall population lifetime that is $\tau_i << \tau_{ex}, \tau_{eh}$. Note that here the total momentum relaxation time of excitons and plasma constitutes a lower limit for the ionization rate. This, however, can be assumed to be rather fast compared to the population lifetime given the efficient phonon scattering in TMDCs at room temperature [154]. Now, from eqs. 2.19 and 2.20 follows that the total injected electron-hole pair density $N_{tot} = n_{ex}^{tot} + n_{eh}^{tot}$. Returning to eq. 2.23, we can additionally assume the fourth term quickly relaxing to zero compared to the longer lifetimes of the electron-hole pair population. Hence, given this fast ionization process, it can be assumed that $\nu_{ex} = n_{ex}^{tot}/n_{eh}^{tot}$ and the total densities can then be expressed as a function of the total injected density as $n_{ex}^{tot} = \nu_{ex} N_{tot}/(1+\nu_{ex})$ and $n_{eh}^{tot} = N_{tot}/(1+\nu_{ex})$. Given these relations, a diffusion equation in analogy to eq. 2.14 for the total time and position dependent density $N_{tot}(\vec{x}, t)$ can be formulated:

$$\frac{\partial N_{tot}(\vec{x},t)}{\partial t} = \Delta[D_{tot} N_{tot}(\vec{x},t)] - \frac{N_{tot}(\vec{x},t)}{\tau_{tot}}, \tag{2.24}$$

where

$$D_{tot} = \alpha_{ex} D_{ex} + \alpha_{eh} D_{eh}, \tag{2.25a}$$

and

$$\frac{1}{\tau_{tot}} = \frac{\alpha_{ex}}{\tau_{ex}} + \frac{\alpha_{eh}}{\tau_{eh}}. \tag{2.25b}$$

Here, α denotes the respective fractions of exciton and plasma with respect to the total injected electron-hole pair density, as $\alpha_{ex} = n_{ex}^{tot}/N_{tot} = 1 + \nu_{ex}$ and $\alpha_{eh} = n_{eh}^{tot}/N_{tot} = 1 + 1/\nu_{ex}$.

From this follows that the diffusion coefficient, i.e., the efficiency of diffusion of the compound exciton-plasma, is a combination of the individual diffusion coefficients of the involved species, weighted by their fractions of the total injected electron-hole pairs. We yet again emphasize that these fractions are given by the Saha equilibrium (eq. 2.22) and are thus a function of both total electron-hole pair density and temperature making this diffusion equation non-linear. Finally, we remark that while the model above is derived under specific assumptions for the case of a coupled exciton-plasma propagation, eqs. 2.24 and 2.25 can be taken as a general model for a multi-component diffusion under the assumption of fast interchange between the two components. This is of particular interest in the context that also the Saha relation of eq. 2.21 can be derived analogously for other thermodynamical formation equilibria, such as the exciton-trion or exciton-biexciton balance in a system.

2.5 Organic-inorganic 2-dimensional semiconductors: Perovskites

In the last section of this theory part we switch to a different system of two dimensional semiconductors, the hybrid organic-inorganic halide perovskites. Generally, perovskites in their 3D bulk form are well established systems that, in the past years, have been focus of broad scientific research, particularly due to their efficient light-matter coupling and high photo-voltaic conversion rates. These properties, while at the same time allowing low-cost, large scale production, have spiked interest for modern photo-voltaic applications[155–158], giving rise to the development of novel high-efficient solar cells [159–161]. More recently, also layered halide perovskites, which are subsequently stacked thin perovskite layers separated by organic parts, have been drawn back into attention for having great potential in photo-voltaic and other opto-electrical applications [161–163]. While such layered structures inherit the advantages of their bulk counter parts, the thinning down to even the limit of monolayers then also leads to arising effects of quantum and dielectric confinement. In principle, such effects have already been intensively studied in the 90s and, similar to TMDC monolayers, it was found that the formation of strongly bound excitonic states dominate their electro-optical properties [133, 164–166]. However, studies of exciton dynamics, in particular transport phenomena, remain largely unexplored, likely connected to the materials' low stability governed by rapid degradation effects at ambient conditions. In this regard, the development of novel techniques to synthesize phase-pure layered perovskites [167, 168] and of methods to suppress degradation effects [169–172] opens ways to explore such fundamental material properties. With respect to the renewed interest in theses materials in terms of potential applications, as well as evident similarities to TMDC monolayer systems, this calls for more in-depth investigations of their fundamental charge carrier dynamics. While in the experimental part of this work we show that we can use methods established for monolayer TMDC systems to access these material properties, the following section shall introduce the basic structure of these layered perovskites. Additionally, an overview of the state-of-the-art understanding of their electronic structure is presented. Finally, their electro-optical properties from empirical studies are briefly discussed.

2.5.1 Structure of layered halide perovskites

Halide perovskites in bulk form are crystalline structures with a face cubic centered (fcc) lattice and an additional atom in the lattice's free octahedron space [173, 174]. This structure is described by the general empirical formula ABX_3, where, in the case of the here considered halide perovskites, A^+ are inorganic cations, B^{2+} are divalent metal

ions and X^- are halide ions [175]. Following from this, there is a wide range of possible combinations of elements to build such crystalline structures [176, 177], giving rise to a huge variety of halide perovskite systems, with specific properties depending on their chemical composition. The unit cell of perovskite lattice is depicted in fig. 2.10 (a). Inorganic cations are positioned on the corners of the fcc unit cell, halide ions on the faces and divalent metal ions in the free octahedron space in the center of the unit cell. In general, such crystals are grown from a stoichiometrical solution of the individual components via self assembly [176]. Adjusting the composition of the solution enables to also grow more complex structures, including thin sheets down to monolayers via

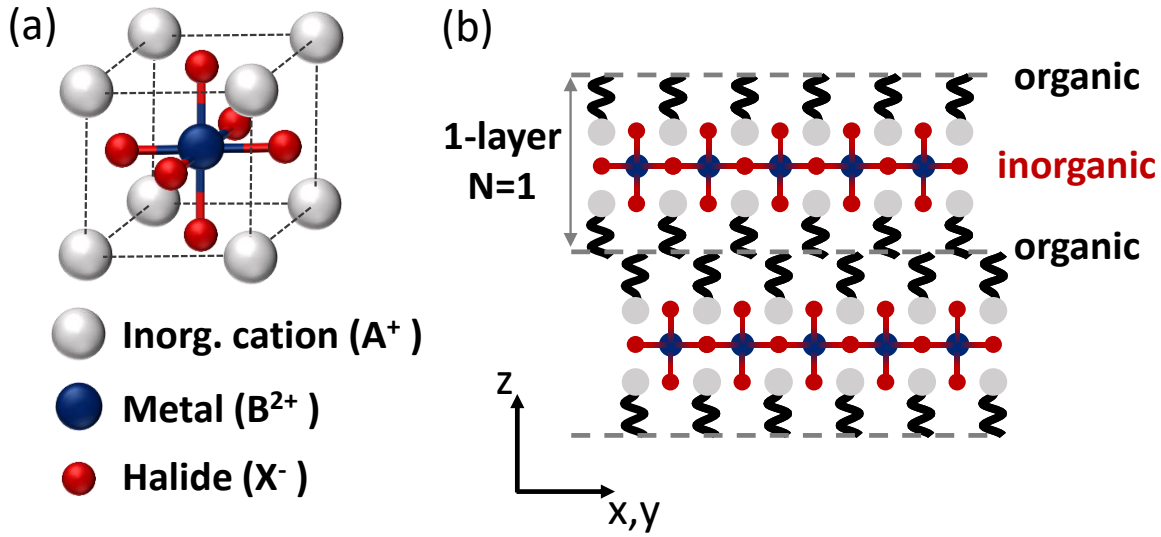

Figure 2.10: (a) Unit cell of a halide perovskite structure. A metal ion occupies the free octahedron space of a fcc lattice while halide ions sit in the face positions and inorganic cations on the corners (organic tails are omitted for clarity). (b) Schematic representation of an exemplary N=1 perovskite crystal, viewed from a cross section perpendicular to the layer-plane. N denotes the number of inorganic layers in each sheet (N=1 is the monolayer limit). Individual sheets are formed and stacked on top of each other, where inorganic parts are separated by the organic tails on the inorganic cations.

decondensation of the 3D structure [178]. The general empirical formula for such thin sheets then yields $A_{N+1}B_NX_{3N+1}$, where N is the characteristic number of individual layers of inorganic perovskite unit cells (in out-of-plane direction) per grown crystal sheet. For the limit of monolayer perovskites of N=1, the empirical formula thus is A_2BX_4. Organic parts, which are attached to the inorganic cations, lead to the self-assembled formation of layered hybrid pervoskites crystals, where adjacent perovskite sheets are separated by the out-of-plane oriented organic tails [176]. An exemplary structure of such a layered perovskite for the monolayer limit of N=1 is schematically

illustrated in fig. 2.10 (b), where the black parts resemble the organic separation layers. The resulting structures are generally highly crystalline [179–182], although they are found to be about a factor of 3-10 mechanically softer than common inorganic semiconductors [182–186]. Additionally, we note that in some systems a temperature dependent phase transition has been reported [187–189]. Furthermore, considering the general stability of the crystals, it is well known that exposure to oxygen and moisture leads to long term degradation of the materials [157, 190–192].

Yet again, turning to the growth of such layered structures, a huge variety of organic tails is available. While we remark that the choice of these chains technically allows to influence the properties of the grown crystal, a detailed discussion is beyond the scope of this work [175, 176]. However, in general, the distance between inorganic sheets is big enough to consider the individual inorganic layers as quantum confined, non-interacting systems in analogy to classical quantum well structures [164, 173, 193]. In the experimental part of this work we will focus only on such monolayer perovskites with N=1, meaning each inorganic sheet consists of only one single layer of inorganic parts in the in-plane direction, forming a purely two-dimensional structure. This can be considered as being the equivalent of a monolayer TMDC, with the interaction of neighboring inorganic sheets being suppressed. Note, however, that the self assembled growth of such stacked, well separated layers has significant practical advantages, as it makes the manual separation of single layers obsolete. At the same time, the use of multiple stacked layers allows to dramatically increase the quantum yield of these materials, since multiple individual monolayer sheets, up to a certain thickness, can contribute to the overall observed optical response.

2.5.2 Electronic structure

Similar as introduced for monolayer TMDCs in sec. 2.1.2, a precise knowledge of the electronic structure, in particular around the direct bandgap [194, 195], is most desirable for the study of electro-optical properties. However, while tremendous efforts in calculating such basic band structures are being made, obtaining accurate theoretical descriptions still turns out to be a major challenge for state-of-the-art first-principle calculations. Theoretical approaches can generally be based on modern computational methods developed for conventional semiconductors, however, the structure of (layered) perovskites demands the inclusion of some non-trivial effects. These include relativistic effects, such as efficient spin-orbit coupling from heavy metal atoms [196–198], coupling to low energy lattice excitations [175], many-body effects [199] and the complex dynamics of the organic layers [200–203]. The latter is of particular significance for lower-dimensional, layered perovskites, where the dynamics of organic parts start to

play a more important role. As a consequence, the theoretical description of ultra-thin layered perovskites is even more complex than that of 3D bulk structures. For this reason, understanding of quantum confinement effects is still at a very early stage. Therefore, while full theoretical models for an adequate description of such intricate hybrid structures are still lacking, there are a few first important findings we like to point out, specifically concerning the influences of the organic interlayers being a major difference in these systems compared to previously discussed TMDC monolayers.

It has been shown that the organic parts in layered perovskites do not have a direct influence on the bandgap, since HOMO (highest occupied molecular orbital) and LUMO (lowest unoccupied molecular orbital) of the organics are energetically well separated from the inorganics' valence and conduction bands [166, 195]. Furthermore, the spacing distance between adjacent inorganic layers, given by the chain length of the organic tails, has only very minor influence on the band structure [188, 198, 204]. On the other hand, it is evidenced that already slight distortions in the inorganic structure, e.g., tilting of the inorganic octahedrons [194, 205, 206], can significantly affect the band structure. Given that the organic chains separating the individual inorganic layers contribute to the overall structural stability, the choice of these organic tails can have non-negligible influences on the resulting band structure and even allows its tunability [207]. Note that this is especially important in terms of being a potential source for significant disorder from dynamic fluctuations in the lattice structure [208], which is absent for conventional semiconductors, and may influence charge carrier dynamics.

In summary we note that theoretical models are not yet able to produce an accurate model for the electronic structure of layered halide perovskites, although rapid progress is made and first general trends and relations transpire. We remark, however, that a general understanding of the electronic structure is even more complex, given the wide array of available perovskite compounds that may have different properties based on their chemical composition of both inorganic and organic parts. Resulting from this, the electro-optical properties in layered perovskites, such as quantum- and dielectric confinement effects, still remain in big parts based on empirical studies [175, 182].

2.5.3 Electro-optical properties

From such studies it is well agreed on that their two-dimensional character and resulting dielectric confinement, similar as in monolayer TMDCs, lead to enhanced Coulomb interactions and formation of tightly bound excitons [133, 164–166]. Since the dielectric environment in these structures is intrinsically predefined by the organic layers, binding energies are strongly dependent on the composition of the individual perovskite structure [133]. In principle, however, values comparable to those in TMDC monolay-

ers around 500 meV can be reached [189, 209, 210]. As a consequence, their optical response at room temperature, in particular in the monolayer limit, is equally strongly dominated by the formation of optically excited excitons. In contrast to TMDCs, however, an increase of layer thickness does not lead to a vanishing of their direct bandgap character. Rather, only a decrease in binding energies is observed due to a progressive loss of Coulomb enhancement from dielectric screening [210]. Furthermore, also a non-hydrogenic Rydberg series of Wannier-Mott-like exciton states has been observed [189, 210, 211], drawing further analogies to the exciton picture as described in sec. 2.1.3.

Following from these empirical studies, the general electro-optical properties of monolayer and thin-sheet perovskites bare remarkable similarities to that of their TMDC counter parts. Likewise, fundamental concepts, such as quantum and dielectric confinement effects, apply in the same fashion. However, significant differences are found in the general structure of the materials that lead to the necessity of including further complexities in their theoretical description. As a result, free charge carrier and exciton properties remain relatively unexplored and an accurate knowledge of their parameters, such as masses and band offsets from band structure calculations, are still lacking. Nevertheless we conclude that the comparability of their electro-optical properties to TMDC monolayers, being dominated by excitonic states, should allow to also apply methods, initially developed for conventional semiconductor system, to these novel hybrid structures. Thus, further empirical studies in connection with the development of more accurate models for the theoretical description are highly motivated to give a way of better understanding charge carrier dynamics in these materials.

Chapter 3
Experimental methods

In the following chapter the experimental methods, utilized in this work, shall be introduced. First, the general procedures for the fabrication of both TMDC and pervoskites samples are discussed. In the following, the two different optical setups that were used are presented and the general measurement routines are briefly discussed. Finally, we introduce the methods employed to analyze obtained data, with particular focus on the accurate evaluation of white light reflectance measurements and the extraction of diffusion coefficients from time- and spatially resolved photoluminescence measurements.

3.1 Sample preparation

All samples investigated in the scope of this work were produced using micro mechanical cleavage (exfoliation) of high-quality bulk crystals and subsequent all-dry visco-elastic stamping techniques, in analogy to a method established in ref. [26]. While the concept of this exfoliation is similar for all materials, there are some differences in the preparation processes, especially considering perovskite samples.

3.1.1 Exfoliation of monolayer TMDCs

The used TMDC materials were commercially available high-quality crystals from HQ Graphene, Netherlands. In order to obtain atomically thin monolayers of these materials, the crystals were cleaved applying the so called scotch tape method, an improved technique of the method first utilized by Novoselov et. al [17] for the preparation of graphene. The principal setup for the preparation is depicted in fig. 3.1 (a) while the individual steps of exfoliation are schematically shown in (b). In a first step, homogeneous sheets of rather thick (few 100's of µm) TMDC crystals are peeled off of the mono-crystalline substrate crystals using Scotch Magic Tape™. These thinned-down crystals are then affixed to a petri dish and can be used as the basis for following processes of further cleaving of the materials. In a second step (schematically depicted in fig. 3.1 (b) 1-3), even thinner sheets are separated from these base crystals using blue Nitto tape (Nitto Denko Corp.) with slightly less adhesion. The tape is inverted and the adhered crystal is carefully put into contact with a prepared PDMS (polydimethylsiloxane) substrate, applying only marginal pressure from the tape's weight alone. The

PDMS substrate ($\sim 1\,\mathrm{cm}^2$) is a commercially available silicone film (P/N WF-20-X4, Gel-Pack®) that is attached to the end of a microscope glass slide. The blue tape is then slowly peeled from the PDMS film in a final cleaving step. Due to the out-of-plane forces being rather weak compared to strong in-plane covalent bonds, it is possible to cleave the crystals down to a single monolayer this way, which is left on the PDMS film. While there is always a finite chance of finding monolayers, peel-off speed and strain applied during this process are the most important parameters determining the quantity and size of individual, obtained monolayer flakes.

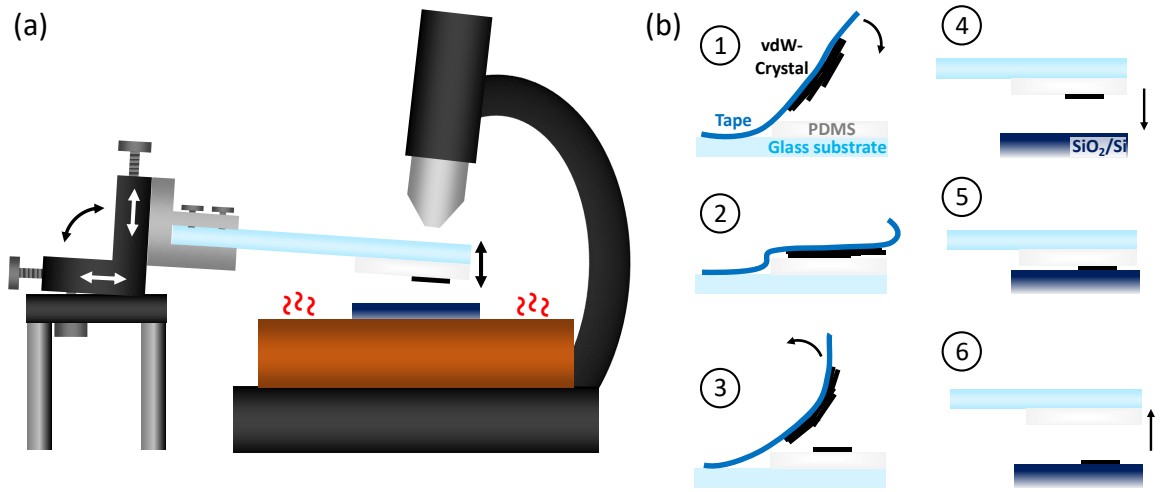

Figure 3.1: (a) Transfer Setup. A microscope glass slide with an attached PDMS film holding the sample flake is clamped into a three axis micrometer stage with adjustable tilt. The SiO_2/Si substrate is fixated via vacuum to a heatable copper chuck underneath. This whole setup is placed under an optical microscope that allows precise positioning and controlling of the sample during the stamping-like transfer process. (b) Single steps of the cleaving process. 1-3 show the transfer from blue Nitto tape to a prepared PDMS stamp on a microscope cover glass. 4-6 depict the actual stamping process that is executed in the setup of (a).

The microscope slide is put under an inverted optical microscope (Nikon Eclipse 150), as depicted in fig. 3.1 (a), and the PDMS film is searched for monolayer flakes, which can be clearly identified via their distinct and strong optical contrast. Note that it is also possible to accurately identify multi-layers, typically up to thicknesses of three layers, this way [212]. Once a monolayer has been identified, it can be transferred to a desired substrate. Common substrates include silicon (Si), thermal oxide on silicon (SiO_2/Si), quartz glass, sapphire, titanium dioxide (TiO_2) and diamond. In this work we used commercially available pieces (0.5 x 0.5 mm) of silicon wafers with a 285 nm thermal silicon dioxide on top. These substrates are cleaned in an acetone and subsequent isopropanol ultrasonic bath for 2 minutes each, to remove any residues of organic resists

that are used in the cutting process of these wafer pieces. They are then additionally subjected to an oxygen plasma for 5 minutes in order do clean off any organic adsorbents that may hinder adhesion of TMDCs [213].

In order to transfer identified monolayers onto the desired substrate, the microscope slide is turned upside down and mounted into a three axis micrometer stage. The substrate is fixated on a heatable vacuum chuck underneath the PDMS film on the microscope slide. Using the optical microscope to follow the process, the PDMS film holding the monolayer flake is slowly brought down onto the substrate. Again, the speed with which the PDMS film is brought into contact with (and removed from) the substrate is the most important parameter for a successful transfer process. Additionally, the three axis stage can be tilted to allow for the flake to get into contact with the substrate in a more controlled way and from a desired direction. During this whole process, the meniscus between PDMS film and substrate, slowly getting in contact with each other, can be observed, allowing to adjust the stamping speed when necessary. The substrate is furthermore preheated to 100°C (70°C for WS_2), assuring a better contact of the sample with the substrate. Particles and other dirt, which can accumulate on the surfaces, are more mobile at these temperatures and can be pushed out of the contact area between sample and substrate by van-der-Waals forces. When the monolayer flake is in full contact with the sample, the PDMS stamp is carefully retracted in the same way, leaving the flake on the substrate, as van-der-Waals forces between flake and substrate are stronger than between flake and PDMS.

3.1.2 Fabrication of TMDC heterostructures

Most of the samples studied in this work were heterostructures, consisting of multiple layers of two-dimensional materials stacked on top of one another. These structures were, in particular, encapsulated monolayer TMDCs, where a desired flake is sandwiched between two ultra-thin layers (typically 5-15 nm) of high-quality boron nitrite (hBN), provided by colleagues from the National Institute for Materials Science, Japan (Ack. 6). Compared to commercial substrates like thermal oxides, thin hBN layers are fabricated by likewise mechanical cleavage of bulk crystals and therefore provide atomically flat and chemically pure substrate surfaces [214–216].

The process of fabricating such samples is analogous to the method described in the previous section, with each individual layer being stamped sequentially. An exemplary structure fabricated this way is depicted in fig. 3.2 and different layers are outlined by color. The hBN layers used for encapsulation, however, do not have to be in the monolayer limit, since their main purpose lies in providing homogeneous and atomically-flat

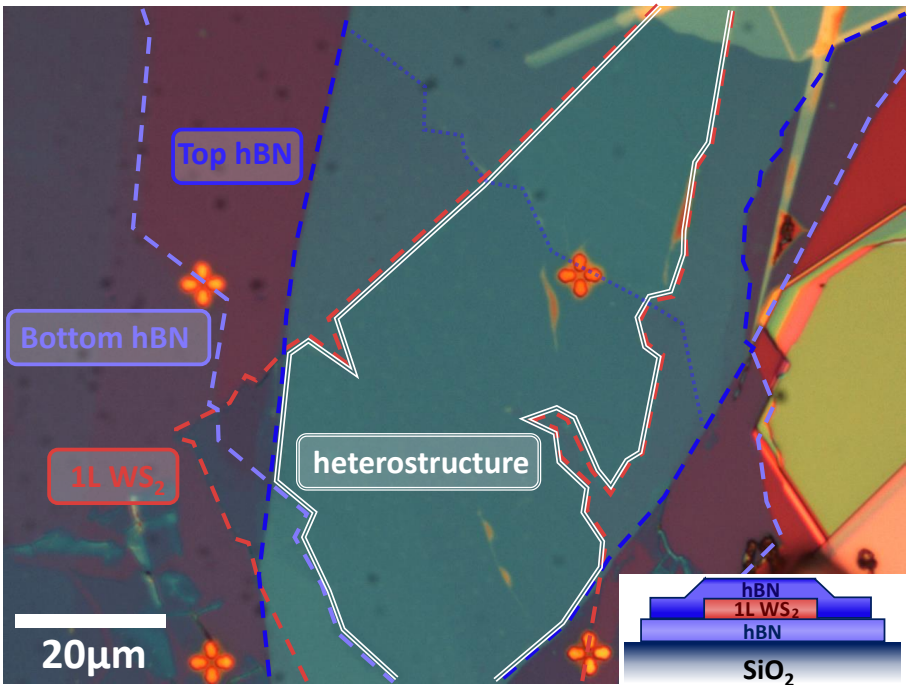

Figure 3.2: Micrograph of a hBN encapsulated WS_2 monolayer sample. Different layers are highlighted by colors and labeled accordingly. The resulting heterostructure is accentuated in white. The dotted blue line marks a step in the top hBN layer thickness. A schematic illustration of the total sample structure is included in the bottom right corner.

surroundings. For this purpose, they are cleaved down to a thickness where they have a high optical transparency (typically <20 nm) and individual steps between atomic layers become visible. After each successful transfer of a single layer, the sample is annealed under high vacuum at 150°C for 2-4 hours, further enhancing interlayer contact between hBN and TMDC layers. Similar to the heating of the substrate during transfer, leftover particles, water and other contaminants between the layers become more mobile and can be pushed to accumulate in small pockets or at layer edges (seen in fig. 3.2 as small orange spots in the heterostructure). This way the remaining contact areas are left clean and homogeneous. We remark that, due to WS_2 showing a sensitivity to temperatures above 70°C, no further annealing was applied to samples after a WS_2 flake had been transferred. Roughly 60 % of structures produced this way had areas with high-quality of interlayer contact on the order of $>50\,\mu m^2$, with this area reaching up to several 100's of μm^2 for the best samples.

3.1.3 Preparation of encapsulated perovskite samples

All of the used layered perovskite materials were provided by colleagues from the Weizmann Institute (Ack. 9). To fabricate samples, thin flakes can be cleaved from the bulk

crystals via mechanical exfoliation and stamped onto a preferred substrate, similar as described for TMDC materials. Though as stated before, they are not as sensitive to their direct (dielectric) environment, since by the nature of their structure, this is predefined by the organic separation layers. Therefore, any heat treatment during transfer, as well as annealing is omitted, which is also necessary with respect to their reported thermal sensitivity [190, 217] and observed phase transitions at elevated temperatures [187]. Additionally, they also do not have to be exfoliated down to a single monolayer, as they are readily grown from stoichometrical solutions to be well separated, stacked monolayer (N=1) crystals (see sec. 2.5.1). Samples are further fully encapsulated in high-quality boron nitride to seal them from influences of the general environment and preserve their optical quality.

Already in the preparation, contact of the perovskites with atmosphere should be kept to a minimum, due to the reported sensitivity to oxygen and moisture [157, 190–192]. In a first step, two thin hBN layers are exfoliated and one of them is stamped onto a SiO_2/Si substrate, while the other one is kept to serve as the encapsulating top layer. Then a flake of perovskite is thinned down to roughly 20-50 nm thickness to give a rather smooth surface for the top layer of hBN to adhere. We note that the overall sample thickness is hereby limited to a few 10's of nm, in order for this top layer of rather stiff hBN to be able to completely cover the sample. The flake is then transferred onto the prepared hBN flake on top of the SiO_2/Si substrate. Subsequently, it is is quickly covered with the remaining hBN while care is taken that this layer completely covers the entire flake and adheres to its bottom counterpart. Typical samples produced this way were on the range of a few 100's of μm^2, similar to TMDC heterostructure samples.

3.2 Experimental setup

In principle, two different optical spectroscopy setups have been used in the scope of this work, as measurements in high external fields were performed in the facilities of the High Field Magnet Laboratory (HFML) in Nijmegen (Ack. 1). Initially, the principal setting shall be discussed, which is largely identical for both setups in terms of the general composition. Additionally, we will briefly introduce the necessary adjustments that are required to allow for measurements in extensive external fields. Finally, also the employed measurement protocols for the individual types of spectroscopy are outlined.

3.2.1 General spectroscopy setup

The general experimental setup for optical spectroscopy measurements is depicted in fig. 3.3. In principle, it can be divided into three parts: excitation arm, sample positioning and detection arm. The excitation arm includes all light sources that can be coupled onto the samples. In this work we use a 250 W spectrally broadband tungsten-halogen lamp (Newport) for reflectance contrast measurements. A 473 nm diode laser or 633 nm Helium-Neon continuous wave laser (both Laserglow Technologies™) serves as the excitation source for steady-state photoluminescence experiments. Finally, for time resolved studies a tuneable 80 MHz Ti:Sa laser system (Coherent Chameleon Ultra II) with 100 fs pulse length is used. Its fundamental wavelength can be tuned between 680-1040 nm and a second harmonic generator can additionally be used to further widen the excitation wavelength range. All light sources are focused onto the sample using lenses and mirrors optimized for light in the visible range.

Samples are placed onto a micro-mechanical xy-stage that allows to move them with a precision of up to 100 nm in the in-plane direction. In order to allow for measurements under vacuum and at cryogenic temperatures down to 5 K, a microscope cryostat (Janis ST-500) can be affixed on top of this stage. The stage itself is mounted on top of an inverted Nikon (Nikon Eclipse Ti) microscope. Light is coupled onto the sample using a 100x magnification microscope objective optimized in the range of UV and visible light. Under cryogenic conditions a 40x magnification objective with a glass correction for the cryostat cover glass is used. Laser spots are focused down to around 0.5μm and 1.3μm full width half maximum (FWHM) with the 100x and 40x objectives respectively. The white light source yields spot sizes around 1μm and 2.5μm FHWM respectively. Light from the sample is directed out into the detection arm using a 50/50 beam-splitter inside the microscope.

It is then first guided through spectral filters to cut away the backscatter of the excitation laser (no filters were used for white light measurements) and then into a spectrometer (Acton SpectraPro SP-2300). The detected light is either spectrally

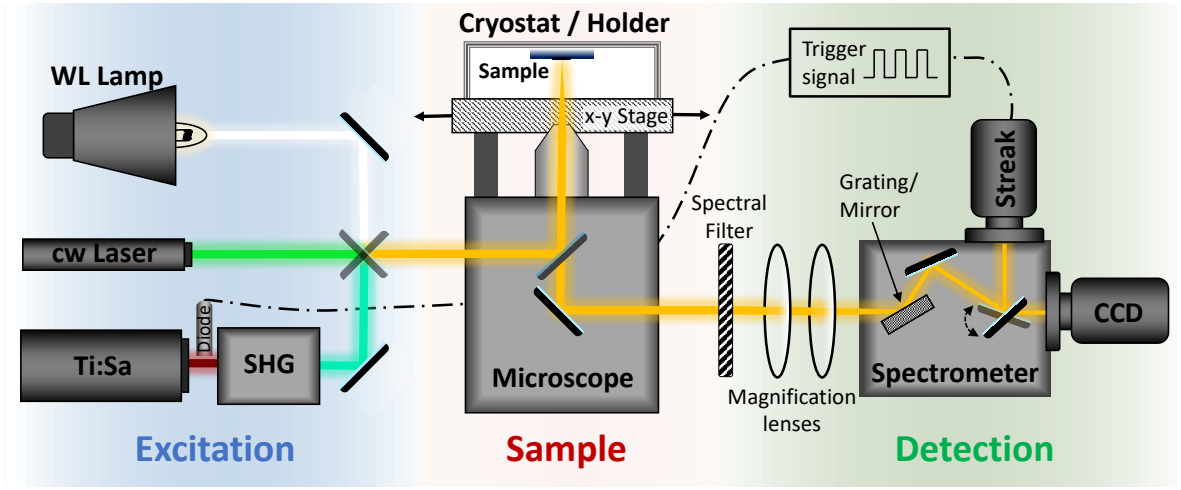

Figure 3.3: Illustration of the principal measurement setup, divided into three parts: Excitation, Sample and Detection. The excitation part includes three different light source options. A spectrally broad white light lamp, various continuous wave (cw) lasers and a tunable 80 MHz, pulsed titanium sapphire laser (Ti:Sa) with a second harmonic generator (SHG). Light is coupled onto the sample via an inverted microscope. The sample is fixed either inside a cryostat or a sample holder atop a x-y micrometer stage. Filters and lenses allow adjusting of the signal in the detection path. Inside the spectrometer, either a grating or a silver mirror is used. For detection a cooled CCD camera or a streak camera, synchronized with the pulsed Ti:Sa laser, are available.

resolved using a grating (300 gr/mm with 750 nm blaze) to yield a spectral resolution of roughly 1 meV or kept in spatial resolution using a silver mirror inside the spectrometer. Two different camera systems are available for detection. For steady state measurements a cooled CCD (Princeton Instruments Pixis 256) is used. Time resolution is achieved, using a streak camera (Hamamatsu universal streak camera C10910) with a coupled CMOS camera (Orca-flash 4.0). The streak camera is synchronized with the pulsed Ti:Sa laser using a laser diode in the fundamental laser path connected to a delay stage. The best achieved time resolution is on the order of 5 ps, although most performed measurements used longer time windows of observation, leading to a reduced resolution on the order of 15-20 ps (depending on the time window).

3.2.2 High magnetic field setup

For measurements in high magnetic fields a slightly different setup was used. While the principal setup remains similar to what is depicted in fig. 3.3, the sample has to be put into a large bath cryostat containing a continuous wave magnet with a nominal maximum field of 32.5 T. Due to the high fields used in this setting, the whole setup of excitation and detection additionally has to be in a distance of about five meters above the actual sample. Instead of a microscope, a more compact sample holder is used. To

have the same control over the sample, it is mounted onto a nanopositioner (attocube systems) located at the end of the sample holder. The sample holder itself consists of a long, double-walled, non-magnetic tube, that can be floated with helium exchange gas and includes an optical microscope lens to focus the excitation light directly onto the sample. Therefor, collimated light from the tungsten-halogen lamp is coupled into the tube via a quartz glass window at the top end, yielding a white light spot size with roughly 2 μm FWHM. The detection utilizes a spectrometer with a 1200 gr/mm grating, resulting in a spectral resolution of 0.2 meV, coupled to a liquid nitrogen cooled CCD camera. Additionally, while the excitation is non-polarized, the detection setup allows to filter the signal for different circular ($\sigma\pm$) polarizations. The sample inside the magnet can further be cooled down to 4.2 K liquid helium temperature and is positioned perpendicular to the applied magnetic field. Under this conditions, the magnetic field can be swept in arbitrary steps up to a maximum field of about 30 T.

3.2.3 Data acquisition

Any non-time resolved data was generally acquired using the CCD camera in combination with the spectrometer, if not explicitly stated otherwise. For reflectance contrast measurements the exposure time is always adjusted, so that the camera sensor is illuminated to roughly 80% of its maximum capacity to achieve maximum signal-to-noise ratio. In addition each spectrum is averaged over 100 individual frames. Three different reflectance spectra are then taken, one on the sample structure (R_S), one on the SiO_2/Si substrate that serves as reference (R_R) and one of a background (R_B), where the light source is blocked. The corresponding reflectance contrast R_C is then calculated according to:

$$R_C = \frac{R_S - R_R}{R_R - R_B} \tag{3.1}$$

Photoluminescence spectra were recorded in similar fashion. Here, the exposure time is adjusted to the emission intensity in order to minimize readouts of the CCD camera. The backscatter of the excitation laser is cut out by placing suitable high-quality edge pass filters into the detection arm. A background spectrum with the laser source completely blocked is taken separately and then subtracted from the signal spectrum.

Time resolved measurements were acquired using the streak camera in single photon counting mode for maximum signal-to-noise ratio. It is taken care that the influence of double-counts, that is two photons hitting the same pixel during a single exposure (10 ms), are kept to a minimum. Such double-counts can lead to an underestimation of the actual signal. Therefore, when necessary, the signal is reduced, using neutral-density filters in order to make sure to always keep the amount of double-counts below a threshold of 5% of the total signal. As a consequence from this, we note that a high

intensity signal is not always of advantage in measurements that incorporate the streak camera, as the intensity has to always be adjusted to keep photon counts below this threshold. Generally, five individual frames were acquired and then averaged over, with each frame having an integration time of 200s.

3.3 Data analysis

The following sections are dedicated to present the methods used in the evaluation of obtained data. First, it shall give an overview of how reflectance contrast spectra are assessed by using a transfer matrix approach under inclusion of a lorentz parameterization to approximate the TMDC monolayers' dielectric function. Additionally, the analysis of time- and spatially resolved photoluminescence measurements and the extraction of diffusion coefficients from streak camera images are discussed.

3.3.1 Analyzing reflectance spectra - a transfer matrix approach

The careful analysis of excitonic resonances from reflectance spectra is a crucial part of this work, as it gives access to not only their energetic position, but also their oscillator strength and, more importantly, their non-radiative broadening. This is done by fitting the results of a transfer matrix calculation to the measured spectra. The TMDC monolayer's dielectric function is thereby accounted for by a modeled function, parameterized from lorentzians. To allow for the evaluation of complex structures and large amounts of data, the whole analyzing procedure described in the following has additionally been written into an automated fitting algorithm, programmed in Matlab® along the lines of ref. [218].

The necessity of using a transfer matrix approach arises from our samples being a stack of multiple thin planar layers, where refraction at interfaces and subsequent interference effects have to be taken into account. In other words, additionally to light being absorbed (in layers with complex refractive indices), incident light will be refracted at each layer interface, where it is partially reflected back. This is schematically depicted in fig. 3.4 (a) for an exemplary structure of N=4 planar layers. Light coming from the bottom (layer 1) and propagating upwards in direction of layer 4 is called forwards traveling and its amplitude in the i-th layer is denoted by v_i. Accordingly, light traveling towards the bottom layer due to reflection is called backwards traveling light and its amplitude is denoted by w_i. The first and last layer are taken as semi-infinite layers, meaning there will be no backwards propagating light in the last layer (w_4=0), as there is no surface from which the light could be scattered back. At the same time, the amplitude of the forward propagating light in the first layer is defined as $v_1 = 1$, since it comes from infinity and has not been refracted yet. Light leaving the structure at the top side towards infinity is the total transmitted light, with the amplitude $v_4 = t_{tot}$, and likewise, light leaving the structure at the bottom is the total reflected light with the amplitude $w_1 = r_{tot}$. The refraction of light at each interlayer surface depends on the

refractive indices of the two materials, as well as the incidence angle. For two adjacent layers i and $i+1$ this is described as:

$$r^s_{i,i+1} = \frac{n_i cos\theta_i - n_{i+1} cos\theta_{i+1}}{n_i cos\theta_i + n_{i+1} cos\theta_{i+1}}, \qquad t^s_{i,i+1} = \frac{2n_i cos\theta_i}{n_i cos\theta_i + n_{i+1} cos\theta_{i+1}}, \tag{3.2a}$$

$$r^p_{i,i+1} = \frac{n_{i+1} cos\theta_i - n_i cos\theta_{i+1}}{n_{i+1} cos\theta_i + n_i cos\theta_{i+1}}, \qquad t^p_{i,i+1} = \frac{2n_i cos\theta_i}{n_{i+1} cos\theta_i + n_i cos\theta_{i+1}}. \tag{3.2b}$$

Here r and t are the refracted and transmitted parts when traveling from layer i to $i+1$ respectively. The indices s and p denote the polarization of the incident light. For unpolarized light we simply yield $r_u = (r_s + r_p)/2$ and $t_u = (t_s + t_p)/2$. n_i denotes the refractive function of the i-th layer with respect to wavelength (or energy). θ_i is the angle of incidence compared to the normal of the interlayer-plane. It is given for the i-th layer by Snell's law according to:

$$\theta_i = arcsin\left(\frac{n_1 sin\theta_1}{n_i}\right). \tag{3.3}$$

The refractive function can be a complex function and is related to the (complex) dielectric function ε as:

$$n^2 = \varepsilon. \tag{3.4}$$

To calculate interference effects of forward and backward traveling light we need to know the lights relative phases. For this purpose, let us consider light of wavelength λ traveling inside layer i with its wave vector k_i defined as

$$k_i(\lambda) = \frac{2\pi n_i(\lambda)}{\lambda}. \tag{3.5}$$

Depending on its wave vector we can then define the lights accrued phase $\delta_i(\lambda)$ (including absorption for complex refractive indices) when traveling through layer i of thickness d_i:

$$\delta_i(\lambda) = k_i(\lambda) d_i. \tag{3.6}$$

From this, we can use a transfer matrix approach relating forwards (v) and backwards (w) traveling light at each interlayer boundary of layers i and $i+1$ (for a more detailed derivation see ref. [218]):

$$\begin{pmatrix} v_i \\ w_i \end{pmatrix} = M_i \begin{pmatrix} v_{i+1} \\ w_{i+1} \end{pmatrix}. \tag{3.7}$$

The Matrix M_i in layer i is given by:

$$M_i = \begin{pmatrix} e^{-i\delta_i} & 0 \\ 0 & e^{i\delta_i} \end{pmatrix} \begin{pmatrix} 1 & r_{i,i+1} \\ r_{i,i+1} & 1 \end{pmatrix} \frac{1}{t_{i,i+1}}. \tag{3.8}$$

Note, however, that $i \in 2, 3...N-1$, since for the first and last layer being semi-infinite, δ_i is not really defined. However, M_0 can simply be defined as having no accrued phase (the light is coming from infinity) and therefore $\delta_i \equiv 0$. A matrix for the last layer is not needed, since the light is going to infinity again, or in other words, has left the multilayer structure. The Matrix for the full structure is then defined as the product of all individual layer matrices as:

$$M_{tot} = \frac{1}{t_{1,2}} \begin{pmatrix} 1 & r_{1,2} \\ r_{1,2} & 1 \end{pmatrix} \prod_{i=2}^{N-1} M_i. \tag{3.9}$$

Here, indices for polarization are omitted for simplicity, since the equations are identical for both. Now r_{tot} and t_{tot}, the amplitudes of light entering and leaving the stack at the front and back, as depicted in fig. 3.4 (a), are coupled via this Matrix analogously to eq. 3.8 as

$$\begin{pmatrix} 1 \\ r_{tot} \end{pmatrix} = M_{tot} \begin{pmatrix} t_{tot} \\ 0 \end{pmatrix} \tag{3.10}$$

and it follows that $t_{tot} = 1/M_{tot,11}$ and $r_{tot} = M_{tot,21}/M_{tot,11}$. Now, calculating the Poynting vector, it can be shown [218] that the total reflectance and transmission of the multilayer stack are

$$R^{s/p} = |r_{tot}^{s/p}|^2, \tag{3.11a}$$

$$T^s = |t_{tot}^s|^2 \frac{Re\left[ncos\theta\right]}{Re\left[n_1 cos\theta_1\right]}, \qquad T^p = |t_{tot}^p|^2 \frac{Re\left[ncos\theta^*\right]}{Re\left[n_1 cos\theta_1^*\right]} \tag{3.11b}$$

and again, for non-polarized incoming light, the average of s and p polarization is used. According to this transfer matrix approach, the reflectance and transmittance of any arbitrary multilayer stack can be calculated, given the refractive functions and thicknesses of each layer are known.

For structures considered in this work, the refractive functions can be taken from literature for all layers but the monolayer. In this case it is calculated from a parameterized model dielectric function using eq. 3.4. For this purpose, a sum of complex Lorentzians, one for each excitonic resonance, and a dielectric background are used to

yield the modeled dielectric function as:

$$\varepsilon_{model}(\lambda) = \varepsilon_{BG} + \sum_j \frac{f_j}{E^2(\lambda) - {E_j}^2 - iE\Gamma_j}, \tag{3.12}$$

with the index j running through the relevant excitonic resonances. The parameters defining the Lorentzians are then their oscillator strength f_j, their resonance energy E_j and their purely non-radiative broadening Γ_j while ε_{BG} is the dielectric background.

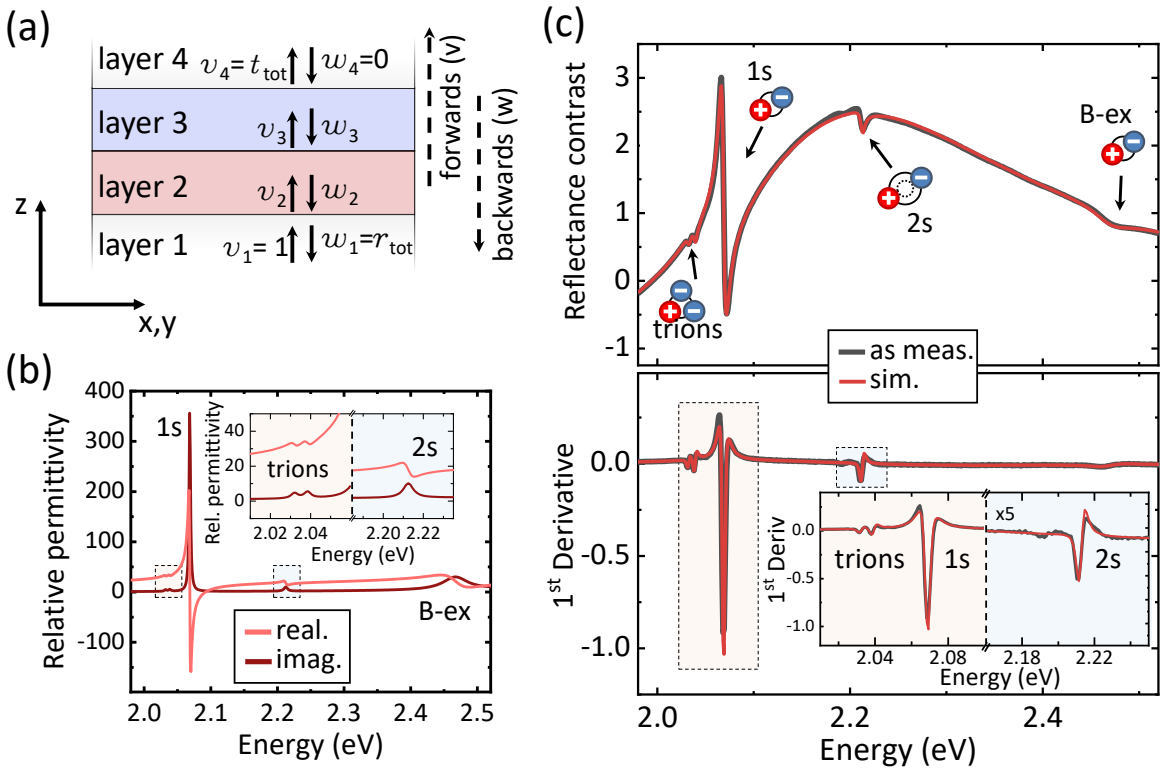

Figure 3.4: (a) Adapted from [218]. Schematic illustration of light traveling through a multilayer stack with N=4 layers. Layers are numbered along the direction of incoming light and first and last are approximated as semi-infinite. v_i and w_i denote the amplitudes of forwards and backwards traveling light in the i-th layer respectively. (b) Real and imaginary parts of a modeled dielectric function for a typical hBN-encapsulated WS_2 monolayer. The dielectric function is parameterized by complex Lorentzian functions, each accounting for one of the excitonic resonances, labeled according to its underlying state. Lorentzians with smaller oscillator strengths are enlarged in the inset for better visibility. (c) Representative reflectance contrast (gray) of an encapsulated WS_2 monolayer sample as measured is shown in the top panel and its corresponding first derivative in the bottom panel. Features from excitonic resonances are indicated by arrows. Red is the simulated spectrum, using a transfer matrix approach and the parameterized dielectric function shown in (b). Individual resonances from excitonic states in monolayer WS_2 are additionally accentuated in the inset.

Such a modeled complex dielectric function is shown in fig. 3.4 (b), including resonances for the exciton ground and excited states (1s and 2s), the trions, as well as the B-exciton transition. From this, using the transfer matrix approach as described above, a reflectance contrast spectrum can be calculated. Hereby, the thicknesses of individual layers, in a first approximation, are guessed from roughly knowing how thick the flakes were during exfoliation. The obtained spectrum is then fitted to the experimental spectrum. Thicknesses and Lorentz parameters for each of the Lorentzians of the dielectric model function are adjusted accordingly. In an iterative process the simulated spectrum can be calculated to closely represent a measured spectrum (see fig. 3.4 (c)). Note that the raw reflectance contrast spectrum of the top panel is used to approximate the thicknesses of the substrate and hBN-layers, which have a rather broad contribution to the spectrum. The first derivative is then used to closely fit the comparatively sharp excitonic transitions (bottom panel and inset). In our data analysis this is commonly done by using both spectra in a simultaneous fitting procedure.

The resulting fitted dielectric function of the monolayer TMDC (fig. 3.4 (b)) then contains complex Lorentzians for each resonance, containing information of the resonance's oscillator strength, linewidth (the actual fitting parameter does not include radiative broadening) and absolute energy position. Additionally, this dielectric function can be used to calculate the transmission of the full stack from eq. 3.11b and, following from that, also the absorption $A = 1 - R - T$ of the stack. Measurements of reflectance contrast and subsequent fitting with a dielectric model function therefore give a convenient handle in investigating basic properties of excitonic resonances. The automated fitting algorithm for this work furthermore allows to track these properties over multiple hundreds or thousands of single measurements. This in return provides the possibility to track exciton resonance shifts and linewidth broadening under changing external influences over large acquired data sets.

3.3.2 Diffusion coefficients from time resolved photoluminescense

In order to measure diffusion of excitons, we use an excitation profile where the intensity is given by a two-dimensional Gauss distribution. A representative excitation profile is depicted in fig. 3.5. Its initial squared width is then defined by the squared width of the laser spot. Following from that, the injected exciton density $n_{ex}(\vec{x})$ right after the excitation at t_0 has the same spatial distribution profile and will broaden with time due to diffusive exciton propagation according to Fick's second law (eq. 2.11). The solution of this equation with a two-dimensional profile is given in eq. 2.12 and yields that the

broadening is described by the change of its squared width with time as:

$$\frac{\partial w(t)^2}{\partial t} = 4Dt, \tag{3.13}$$

where D is the diffusion coefficient and t is time. The diffusion coefficient is linearly proportional to the change in the exciton density's squared Gauss width and can be related to its relative broadening as $D = (w(t)^2 - w(t_0)^2)/4t$.

The observed parameter under experimental conditions, however, is the photoluminescent response of the exciton ensemble. Here, we assume its intensity $I(\vec{x}, t)$ to be directly proportional to the density of the entire exciton population $n_{ex}(\vec{x}, t)$. This is reasonable, since scattering of excitons at room temperature is sufficiently fast compared to the exciton lifetime [154]. Due to that, intermixing of all exciton species (bright and dark) via scattering can be assumed, meaning that dark excitons can scatter into the

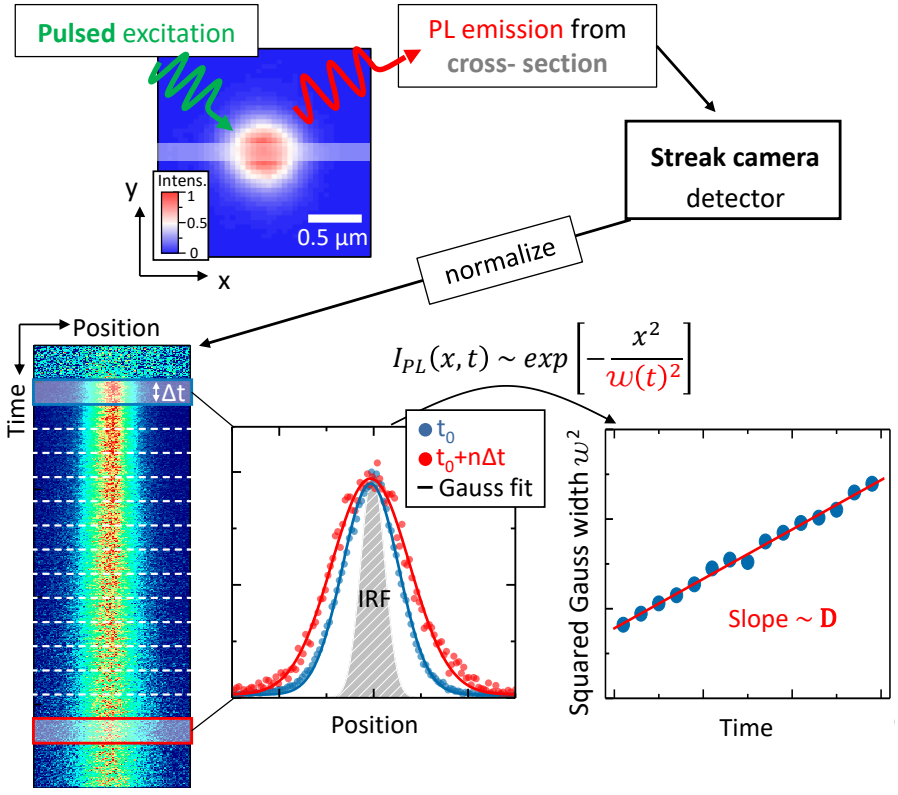

Figure 3.5: Measurement procedure for diffusion experiments. Initially, a spot with Gaussian density distribution is excited with the pulsed laser. The photoluminescence response from a cross-section of the center part is projected onto the streak camera. Time- and spatially resolved signal (shown for a representative measurement) is normalized and spatial profiles at different time steps are taken. The squared Gauss width of these is extracted from fits and plotted with respect to time. From a fit to these data the diffusion coefficient is determined.

light cone and, vice versa, bright ones can scatter out of it. The photoluminescence signal from only the bright excitons can therefore be taken as being representative of the whole exciton population. The spatial evolution of its intensity therefore also gives direct access to the change of the exciton density distribution with time. The wanted broadening of the exciton density profile can therefor be directly tracked from the corresponding broadening of the photoluminescence intensity with time.

The way this is realized is by directly projecting an approximately one-dimensional cross-section of the middle of the emission spot onto the streak camera. Since a two-dimensional Gauss is centrosymmetric, its width can be extracted from such a one-dimensional cross-section in analogy to the diameter of a circle. Therefore, the squared width of the two-dimensional exciton density distribution can be tracked from the one-dimensional cut-out of the PL signal. Using the streak camera to deflect this signal in time yields temporal resolution along the y-axis and at the same time allows to follow the Gauss width along the x-axis of the detected signal. In order to extract diffusion coefficients from such a measurement, the signal is cut into n temporal slices with an appropriately chosen constant width of Δt. For each of these temporal slices the signal is then integrated over time, yielding spatial density distribution profiles (spatials). Note that the width of the slices has to be chosen so that the signal-to-noise ratio of the spatials is reasonable. These are then fitted with a Gauss function $I_{PL}(x,t) \sim \exp(x^2/w(t)^2)$ and the squared Gauss width $w(t)^2$ is extracted. It is plotted as a function of time and the diffusion coefficient can be extracted from the slope of a linear fit to these data according to eq. 3.13.

Chapter 4
Results and discussions

This chapter focuses on the experimental studies that were performed in the scope of this work. It is structured to follow closely along the lines of the theoretical background, discussed in sections 2.2 - 2.5. For this purpose, this chapter is divided into four separate sections, thematically matching the corresponding theory part. In each of the segments the experimental setting and performed measurements are presented, followed by a detailed discussion of the obtained results, with respect to the theoretical understanding.

4.1 Excitons in high magnetic fields

In the first experimental project of this work, basic excitonic properties were investigated via magneto-optical measurements in high magnetic fields [83]. The main focus lay on the experimental determination of the exciton size of ground and excited states in the representative TMDC monolayer system of WS_2. In the context of the extraordinarily tightly bound excitons in this system, it is of interest to consider that such binding energies ($\sim 0.5\,\mathrm{eV}$) are commonly associated with Frenkel-like excitons, known from molecular crystals [219–221]. In contrast to that, experimental and theoretical findings support the applicability of a Wannier-Mott type-like model [24, 27, 78]. Therefore, knowledge of the spatial extent of the exciton wave functions can help unravel the nature and correct physical description of these excitons. At the same time, this also provides a spatial scale for any relevant fluctuations in the environment, the effects of which will be discussed in the next experimental section (see sec. 4.2). While similar experiments have been performed on WSe_2 monolayers [28, 116], our study shows that the investigated physical properties are not unique to a single material system but can rather be taken as basic properties in TMDC monolayers, confirming their general physical origin. Additionally, also the valley-Zeeman shift was measured, allowing to extract the exciton g-factors for both ground and excited state. All of the high field experiments were carried out in a collaborative work in the facilities of the High Field Magnet Laboratory (HFML), Nijmegen (Ack. 2 and Ack. 1).

4.1.1 Measurements in high magnetic fields

As described in sec. 3.2.2, the samples in this experiment were placed inside a resistive continuous wave magnet, reaching fields as high as 29 T with the field being oriented perpendicular to the sample, depicted in fig. 4.1 (a). Reflectance contrast measurements were taken in 1 T steps, where spectra on the sample were acquired in the "up-field" sweep and reference spectra on the SiO_2/Si substrate on the "down-field" sweep, in order to minimize the need for sample re-positioning. The sample was cooled to 4.2 K

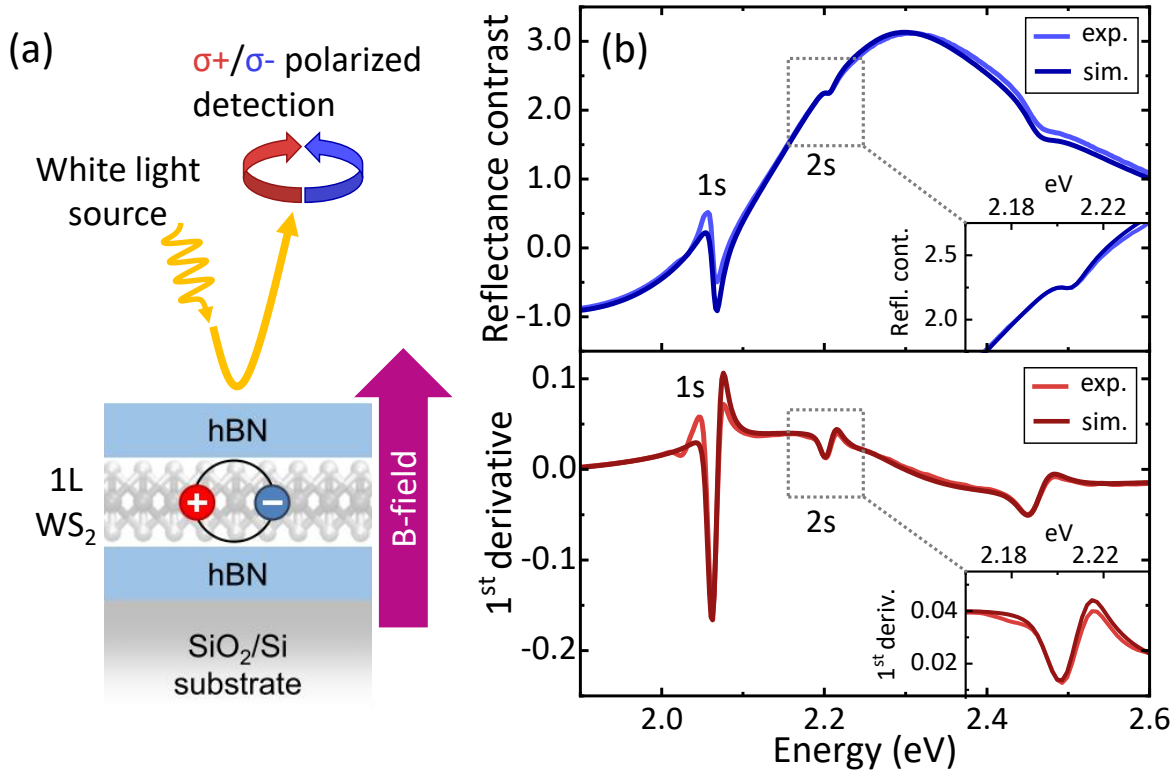

Figure 4.1: (a) Simplified illustration of the experimental setup. An encapsulated WS_2 monolayer flake is positioned perpendicular to the applied B-field. The spectrally broad white light source is used in excitation and the signal is detected while resolving for circular $\sigma\pm$ polarization. (b) Top panel: As-measured reflectance spectrum at T = 4.2 K and B = 0 T (light blue). Dark blue is a simulated spectrum fitted to the data, using the transfer matrix method described in sec. 3.3.1. Bottom panel: Corresponding first derivative of the reflectance contrast for better visibility of the excitonic resonances. The excited state 2s resonance is further enhanced in the insets.

liquid helium temperature and the 250 W broadband tungsten-halogen lamp served as the light source. Signal from the sample was resolved in circular $\sigma\pm$ detection. The sample under consideration was a fully encapsulated WS_2 monolayer and two different positions on the sample were measured. The encapsulation in high-quality boron nitride leads to a significant narrowing of the excited state linewidth [103, 222] (discussed in

detail in the next section) and allowed for a more precise tracking of resonance energy shifts. Additionally, also a non-encapsulated (bare) sample on a Si/SiO_2 substrate was measured for comparison.

An exemplary reflectance contrast spectrum, calculated from measurements according to eq. 3.1 of the sample with respect to the SiO_2/Si substrate at $B = 0\,T$, is shown in the top panel of fig. 4.1 (b). The corresponding derivative is included in the bottom panel. Simulated spectra using the method detailed in sec. 3.3.1 are included and the observed exciton resonances are labeled correspondingly. The first excited 2s state is further accentuated in the inset for better visibility. The respective energy positions of 1s ground and 2s excited state of 2.067 and 2.208 eV and the energy separation on the order of 140 meV are consistent with literature values reported for encapsulated samples [28, 71]. Note that further higher lying states $n \geq 3$ are not observed, which is most likely due to these states having low binding energies and thus merging into each other and the bandgap. We additionally remark that recent works show that these resonances can also be tracked from photoluminescence spectra, given sufficient sample quality and excitation power [223].

4.1.2 Magnetic field dependent exciton resonance shifts

The energetic shifts of resonances in the encapsulated WS_2 sample upon applying magnetic fields up to 29 T are presented in fig. 4.2. Here, only the reflectance contrast's first derivatives are shown, since there, the sharp excitonic resonances are more pronounced in contrast to the broad background, stemming mainly from interference effects of the thin hBN layers. Fig. 4.2 (a) shows a false color plot of these derivatives in the energetic range of the 1s and 2s resonance. The detected light is resolved for $\sigma+$ and σ- polarization components, stemming from either K+ and K- valley respectively, according to the selection rules detailed in sec. 2.1.2. The magnetic field induced resonance shifts are indicated by dotted lines. Corresponding spectra in the same energy range are depicted in fig. 4.2 (b). For clarity, only every third spectrum is shown. Here, the dotted line indicates the ground and excited state resonance energy E_0 at zero field ($B = 0\,T$), where both valleys and thus the resulting transition energies are energetically degenerate. The extracted relative energy shifts $\Delta E_{\sigma\pm}$ for 1s and 2s state with respect to E_0 as a function of the magnetic field are shown in fig. 4.2 (c). Measurements for a second sample position with similar overall resonance energies and linewidth are included. We further note that a second measurement on the first sample position (not shown) yielded essentially the same results. In the field induced shift of the 1s ground state we find a mainly linear field dependence with different sign for $\sigma+$ and σ- polarization. In contrast to that, the 2s resonance energy, additionally to this linear shift,

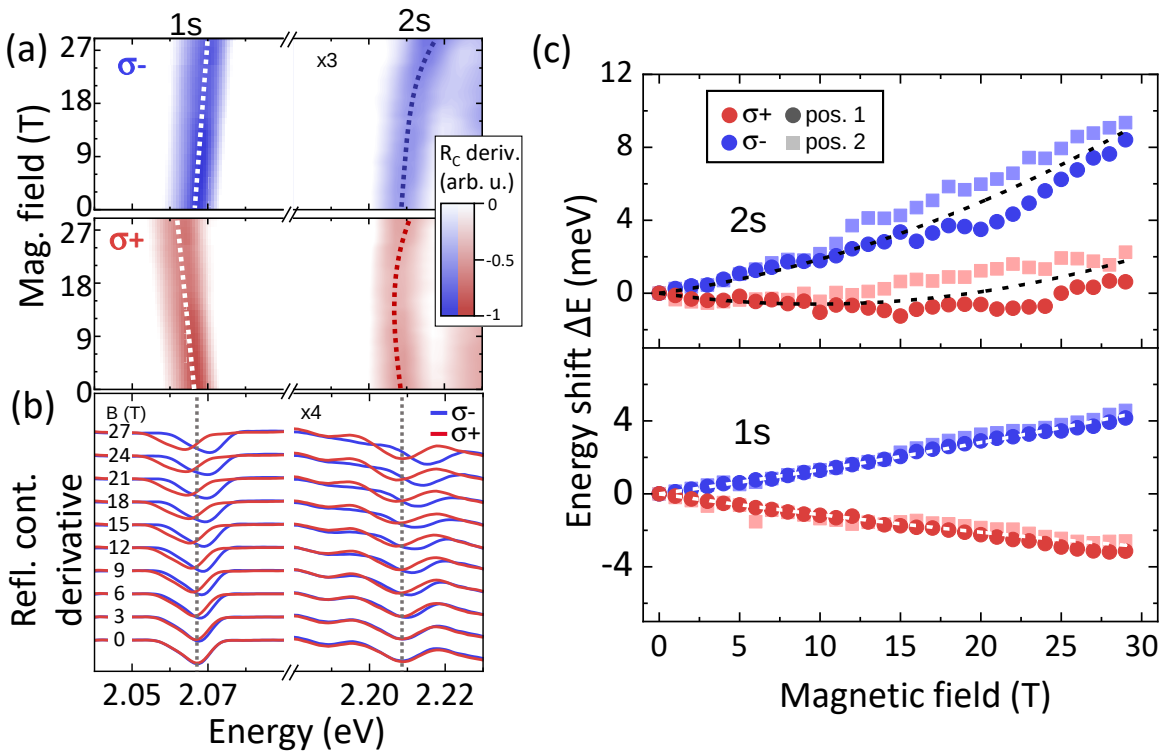

Figure 4.2: (a) First derivative of the reflectance spectra in the range of the two excitonic states in a 2D false color plot. The dotted lines are guides to the eye for tracking the magnetic field induced energy shifts. Top and bottom panel are measurements from σ- and σ+ polarized detection respectively. (b) Corresponding first derivative spectra of the measured reflectance contrast in 3 T intervals. Different polarizations are color coded and the resonance energy at 0 T is indicated by dotted lines for both resonances. (c) Extracted relative energy shift for ground (bottom) and excited state (top) with respect to the magnetic field. Measurements from two sample positions are included and the data are shown for $\sigma\pm$ detection. The dotted lines are the average energy shifts from the combination of individual valley Zeeman and diamagnetic shift contributions (detailed in fig. 4.3).

shows a clear non-linear contribution, that has positive sign for both polarizations. The linear part of the shift can be attributed to the well studied valley Zeeman shift, which splits the energy resonances of K+/K- valley linearly with magnetic field, depending on the valley g-factor according to eq. 2.9. The non-linear shift to higher energies in both polarizations is attributed to the diamagnetic shift. This shift is more pronounced in the higher excited state due to its dependence on the exciton radius, which will be discussed in more detail below.

Furthermore, we note that this gives additional confirmation of the assignment as a higher excited excitonic 2s resonance. In particular, it allows to exclude the proposed interpretation of that resonance stemming from a phonon-assisted transition related to the 1s-ground state [224], as, in this case, this resonance should closely follow the

energy shift of the ground state. The overall measured resonance energy with respect to magnetic field is shifted by a combination of both contributions from valley Zeeman effect (eq. 2.9) and diamagnetic shift (eq. 2.10) and can be written as $E_{\sigma\pm,n}(B) = E_{0,n} + \Delta E_{\sigma\pm,n} = E_{0,n} + \Delta E^{vZ}_{\sigma\pm,n} + \Delta E^{dia}_{n}$. From that, the individual contributions of the two effects can be extracted by either subtracting or averaging the polarization resolved resonance Energies $E_{\sigma+,n}$ and $E_{\sigma-,n}$:

$$\Delta E^{vZ}_{n} = E_{\sigma+,n} - E_{\sigma-,n}, \tag{4.1}$$

$$\Delta E^{dia}_{n} = \frac{1}{2}\left(E_{\sigma+,n} + E_{\sigma-,n}\right) - E_{0,n} \tag{4.2}$$

Note that ΔE^{vZ}_{n} then is the total energy splitting between transition energies of the different K± valleys, arising from the valley Zeeman effect.

4.1.3 Quantitative valley Zeeman and diamagnetic shift

The extracted valley Zeeman and diamagnetic shifts, using eqs. 4.1 and 4.2, are presented in fig. 4.3 (a) and (b) respectively for both observed exciton states. We find that the contribution from the valley Zeeman effect shows a strictly linear behavior and using $\Delta E^{vZ}_{n} = g^{vZ}_{n}\mu_B B$ (which follows from eq. 2.9) allows to extract the valley Zeeman g-factor g^{vZ} from linear fits. The obtained values for the two different excitonic resonances are $g^{vZ}_{1s} = -4.35 \pm 0.1$ and $g^{vZ}_{1s} = -4.2 \pm 0.1$ and are consistent with previous measurements on WS_2 monolayers [115–117]. Considering the experimental uncertainty, the shifts for both exciton states are essentially equivalent. This suggest that the transition energies follow the shifts of the valence and conduction bands in a single particle picture as described in sec. 2.2.1. As a consequence, we can conclude that these effects are mostly independent of the different spread of the exciton wave function in reciprocal space, which follows from their different extension in real space.

The diamagnetic shifts, on the other hand, are significantly different for the two states and almost an order of magnitude bigger for the 2s state compared to the 1s ground state. It is quantified by its diamagnetic shift parameter σ_n, which is obtained from the purely quadratic fits shown in fig. 4.3 (b) according to eq. 2.10. As discussed in sec. 2.2.3, the use of this model in a weak-field limit is well justified considering that the estimated Landau level splitting, i.e., half of the cyclotron energy, is on the order of 10meV. This is well below typical exciton binding energies for both 1s and 2s exciton states [24]. The extracted values for the diamagnetic shift parameter of the two measured sample positions are $\sigma^{pos1}_{1s} = 0.58 \pm 0.03\,\mu\mathrm{eVT}^{-2}$ and $\sigma^{pos2}_{1s} = 1.2 \pm 0.08\,\mu\mathrm{eVT}^{-2}$ for the ground state. For the first excited state the values yield $\sigma^{pos1}_{2s} = 4.9 \pm 0.14\,\mu\mathrm{eVT}^{-2}$

and $\sigma_{2s}^{pos2} = 7.9 \pm 0.22\,\mu\text{eVT}^{-2}$. From these values the average relative energy shifts $\Delta E_{\sigma\pm}$ can be numerically calculated by combining both valley Zeeman and diamagnetic contributions taken from the fits. The obtained average of the two positions with respect to the magnetic field is included in fig. 4.2 (c) by dotted lines.

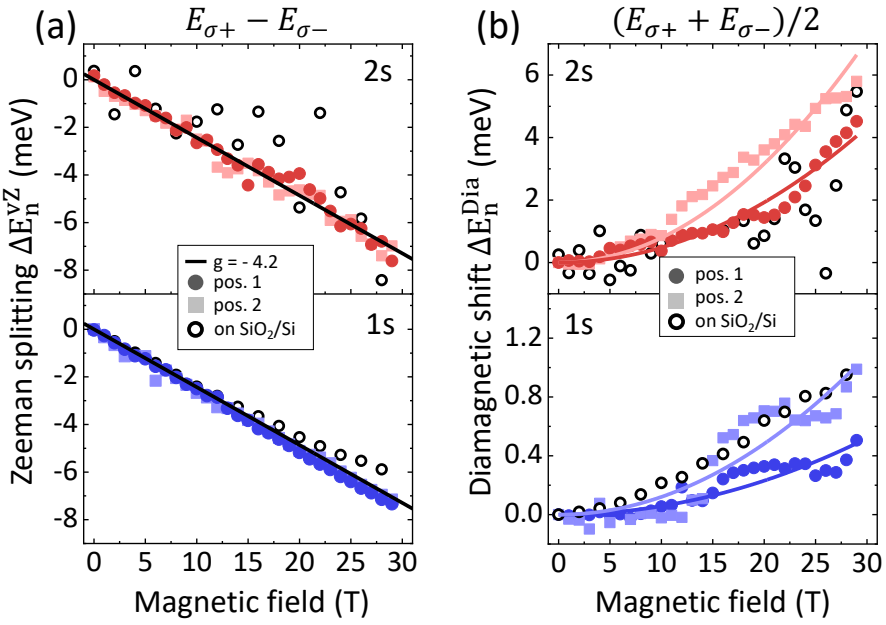

Figure 4.3: (a) Valley Zeeman shift of 2s (top) and 1s (bottom) state for both sample positions, obtained from eq. 4.1. The black line indicates a valley Zeeman g-factor of -4.2. (b) Extracted diamagnetic shifts using eq. 4.2. Solid lines are purely quadratic fits to the experimental data. Additionally values for the non-encapsulated reference sample are included as open circles.

Data, measured on the non-encapsulated sample for comparison, is presented in fig. 4.3 as open circles. The data is more noisy due to the resonances being more strongly broadened and thus harder to track. Still, the trend of the resonance shifts roughly follows the data for the hBN-encapsulated sample for both valley Zeeman and diamagnetic shift, further confirming our interpretations. The extracted diamagnetic parameter of $3.5 \pm 0.55\,\mu\text{eVT}^{-2}$, being slightly lower than for the encapsulated samples, is reasonable in a picture where the different dielectric surroundings and subsequent dielectric screening can lead to reduced exciton radii [225].

Let us now turn to the spread of the diamagnetic shift between the two different sample positions of the encapsulated sample. It is likely to be due to systematic uncertainties in the experiment, such as, for example, different average dielectric surroundings on different sample positions (further discussed in sec. 4.2.3). Additionally, we note that, in particular for the 1s state, the careful analysis of the diamagnetic shift is challenging, with the absolute shift only being in the range of 0.5-1 meV at fields up to

29 T. These shifts are close to the experimental resolution of our setup, although the detection is technically more sensitive to relative shifts, than is given by its absolute resolution. Nevertheless, this gives a potential reason for the presented values being slightly above previously reported measurements in fields up to 65 T [116].

In the further analyzing of the data we will regard the two measured positions as being equivalent, considering the similarities of their optical response, especially concerning identically narrow resonance linewidth. The relative spread from the two measurements is on the order of $\pm 20\,\%$ for the obtained diamagnetic shift parameter, which will lead to a spread of $\pm 10\,\%$ in the analyzing of the excitons' spatial extent.

4.1.4 Exciton radii from diamagnetic shifts

According to eq. 2.10, knowledge of the diamagnetic shift parameter σ_n provides a direct relation of the mean square radius $\langle {r_n}^2 \rangle$ to the reduced effective exciton mass μ_{ex} for the n-th excitonic state. This relation is given as $r_n = \sqrt{8\mu_{ex}\sigma_n}/e$. The resulting dependence of the root mean square radius $\sqrt{\langle {r_n}^2 \rangle}$ with respect to the reduced exciton mass is plotted in fig. 4.4 (a), using the values of σ_n from the magnetic field measurements. The colored, solid lines are the derived exciton radii for the two measured sample positions presented for a broad range of effective masses in values of the electron rest mass m_0. Over this whole range the obtained 1s rms radii are on the order of 2-3 nm and those of the 2s are between 5-8 nm. From eq. 2.2 we can additionally estimate a reduced effective exciton mass, using effective electron/hole masses in valence and conduction band, calculated in a single-particle band structure [56]. This yields $\mu_{ex} = 0.15\, m_0$ and is indicated in fig. 4.4 (a) by a black vertical line. The rms radii then are 2.0-2.9 nm for the ground and 5.8-7.4 nm for the first excited state. These results are in reasonable agreement with previous measurements of the 1s state radius of 1.5 nm on SiO_2 [116], where a slightly smaller radius would be expected, considering the lower dielectric screening in these structures. Reports for higher lying states had so far only been reported for WSe_2 monolayers and, with 6.6 nm rms radius, were in the same range as our values. In addition it is noted that very recent measurements up to fields of 91 T provide a better analyzing of the 1s shift due to the extended field range and yield a WS_2 1s rms radius in hBN of 1.8 nm. The experimentally determined reduced effective mass of $0.175\, m_0$ is slightly higher than the theoretically predicted mass [119].

Also included in fig. 4.4 (a) in gray shaded contours are theoretically calculated radii from effective mass models for Wannier-Mott like excitons [69, 131]. The Schrödinger equation is solved while accounting for the non-local dielectric screening by introducing a thin-film Coulomb potential in the form given in eq. 2.4. The dielectric constant of

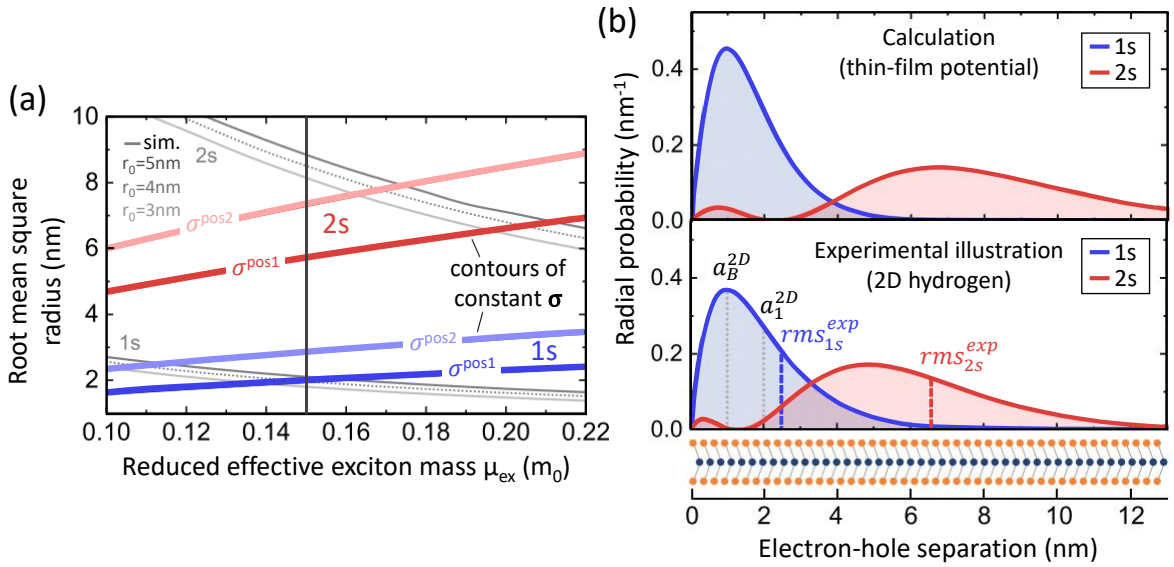

Figure 4.4: (a) Estimated exciton root mean square radii for ground and excited state as a function of the reduced effective exciton mass μ_{ex}. The solid lines are obtained using eq. 2.10, with constant values for the diamagnetic shift constant σ_n, extracted from the quadratic fits shown in fig. 4.3. Gray lines are simulated rms radii, calculated from solving the Schrödinger equation, using the thin-film potential from eq. 2.4. It is shown for three different reasonable screening length r_0 and assuming a dielectric constant $\varepsilon_s = 4.5$ for hBN, taken from literature values in the optical frequency range [226]. Reasonable agreement is obtained near the theoretically predicted reduced mass value [56], indicated by a solid black line. (b) Exciton radial probability as a function of the electron-hole separation, from the exciton envelope wave functions of 1s and 2s state. Top panel shows numerically calculated values using the thin film potential, $\varepsilon_s = 4.5$, $r_0 = 4\,\text{nm}$ and $\mu_{ex} = 0.15\,m_0$. Bottom panel shows results from purely 2D hydrogenic wave functions [124] with the rms radii fixed to the average values of 2.45 and 6.6 nm, extracted from (a) for 1s and 2s state respectively. The Bohr radius a_B^{2D} and the exponential parameter in the wave function a_1^{2D} are indicated by dotted lines. A schematic to-scale representation of the real space lattice is shown on the bottom.

the surroundings ε_{ext} is set to a value of 4.5 for hexagonal boron nitride in the range of optical frequencies [226] and r_0 is varied in a reasonable range of 3 to 5 nm [69, 84]. Note that the different dependence of the rms radius on the effective mass in the calculations, compared to the measurements, stems from the different approach of obtaining the rms radius. In the calculations a well defined potential is introduced, while the diamagnetic parameter is not defined at all, but rather varies with the calculated rms radius according to eq. 2.10. In contrast to that, the experimental approach has it the other way round, meaning that a fixed value for the diamagnetic parameter is obtained. A variation of the effective mass then leads to a varying of the underlying potential, which is not directly experimentally accessed. Thus, in these two approaches, the parameters changing as a function of the reduced effective mass are different ones,

leading to the displayed effective mass dependencies. Nevertheless, we find a reasonable agreement of theoretically calculated and measured values in the range of the estimated effective mass of $\mu_{ex} = 0.15\, m_0$.

Fig. 4.4 (b) presents the spatial extent of the excitons in encapsulated monolayer WS_2. Here, the radial probability densities, defined through the exciton envelope wave function as $2\pi r|\Psi_n(r)|^2$, are shown as a function of the electron-hole separation r. A schematic to-scale representation of the WS_2 lattice with a lattice constant of 0.315 nm is included on the bottom. The top panel shows numerical solutions of the Schrödinger equation using the aforementioned thin-film potential with r_0=4 nm and ε_{ext}=4.5, as well as μ_{ex}=0.15 m_0. As discussed in sec. 2.1.3, such a model then allows to estimate binding energies and we obtain 147 meV for the 1s and 31 meV for the 2s state. The 1s-2s separation of 116 meV thus deviates slightly from the one observed in experiment ($\sim$ 140 meV), which is attributed to possible deviations of the effective masses, the approximate Coulomb thin-film potential and experimental uncertainties. The bottom panel is an illustration using purely hydrogenic 2D radial wave functions $\Psi_n(r)$ [124] according to:

$$\Psi_{1s} \propto exp\left(-\frac{r}{a_1}\right), \tag{4.3}$$

$$\Psi_{2s} \propto \left(2 - \frac{4r}{3a_2}\right) exp\left(-\frac{r}{3a_2}\right). \tag{4.4}$$

The wave function parameters a_1 and a_2 are adjusted to fit the average rms radii of the 1s and 2s state to those obtained in experiments, i.e., $rms_{1s}^{exp} = 2.45$ nm and $rms_{2s}^{exp} = 6.6$ nm. In contrast to that, in an ideal 2D hydrogen model, as described in sec. 2.2.2, the variable in the wave function is a constant for all states and related to the Bohr radius a_B^{2D}, meaning $a_1^{2D} = a_2^{2D} = 2a_B^{2D}$. For the present case of $a_1 \neq a_2$ this further illustrates the deviation from a purely hydrogen-like description of the exciton physics in the TMDC monolayers. (Note that here also the orthogonality of the radial wave function for states with identical orbital quantum number is lost).

Interestingly, despite these differences, we find that the wave functions from the numerical solution and those of the 2D hydrogen model indeed have an overall similar shape, aside from slight details. Thus, while the description of excitons in analogy to a hydrogen model is not perfectly physically accurate, it is still a helpful illustration in understanding the general picture of excitons. In particular, it further supports the applicability of the hydrogen-like Wannier-Mott type exciton picture, considering that exciton states extend over a multitude of lattice constants. Especially higher lying states, due to their bigger radius, span over hundreds of lattice sites, taking into account their two-dimensional nature. Furthermore, a hydrogen like description of ex-

citons, when accounting for the non-local screening with a modified thin-film Coulomb potential, is found to yield an adequate approximation in comparison with experimentally obtained results. Thus, while ab initio calculations remain extremely helpful in obtaining accurate theoretical descriptions with high numerical precision, this approach can provide an appropriate tool to assess fundamental physical properties of excitons in two dimensional TMDCs monolayers.

4.2 Influence of the environment in experiments

As discussed in detail in sec. 2.3, the environment of two-dimensional semiconductors is expected to have a significant influence on its optical response. In particular, inhomogeneities in the direct layer vicinity can give rise to potential fluctuations in the dielectric surroundings, influencing the resonance linewidth and absolute energy position of exciton resonances. As also addressed in the previous segment, under most experimental conditions it is favorable to have resonance linewidth as narrow as possible. This is necessary not only to allow for accurate qualitative tracking of energetic shifts, but on the whole opens the way for an accurate study of diminutive details in the optical response. Additionally, control over such disorder, or more generally, the dielectric surroundings gives a handle to tailor excitonic properties and can also have effects on properties, such as the exciton propagation, as discussed in the next segment. Therefore a thorough understanding of effects from environmental influences and how to avoid or engineer them is of wide interest. In the following we investigate this subject via the different responses of excited states to changes in the dielectric environment.

4.2.1 Resonance broadening from nanoscale disorder

First, we study dielectric disorder on the nanoscale, that is fluctuations in the dielectric surroundings on scales that are bigger than the exciton state's average size (on the order of a few nm, as shown in the previous segment) but smaller than the average probed area (typically on the order of 0.5-2 µm). We note that excitonic resonances, in a good approximation, should not be sensitive to disorder on a scale significantly smaller than the underlying exciton state's radius. The reason for that is that we can assume the screening of Coulomb interactions to be proportional to the average dielectric constant between the two charges in consideration. Given the spatial scale of fluctuations in the dielectric constant is considerably smaller than this distance, the exciton is just not sensitive to it, as it will always be averaged over.

In order to investigate effects from nanoscale disorder we compare two different types of samples, schematically depicted in the top part of fig. 4.5. On the left is an artist's impression of a TMDC monolayer exfoliated on a typical SiO_2/Si substrate that is commonly known to have a rather rough surface on the relevant scale [215, 227, 228]. Additionally, particles and residues from sample preparation are expected to be adsorbed on top of the TMDC flake. This leads to overall non-homogeneous (dielectric) surroundings of the sample. The second sample under consideration is a hBN-encapsulated TMDC monolayer using high-quality hexagonal boron nitride. In this configuration the sample's environment is expected to be more homogeneous [214, 215, 227], as described in sec. 3.1.2.

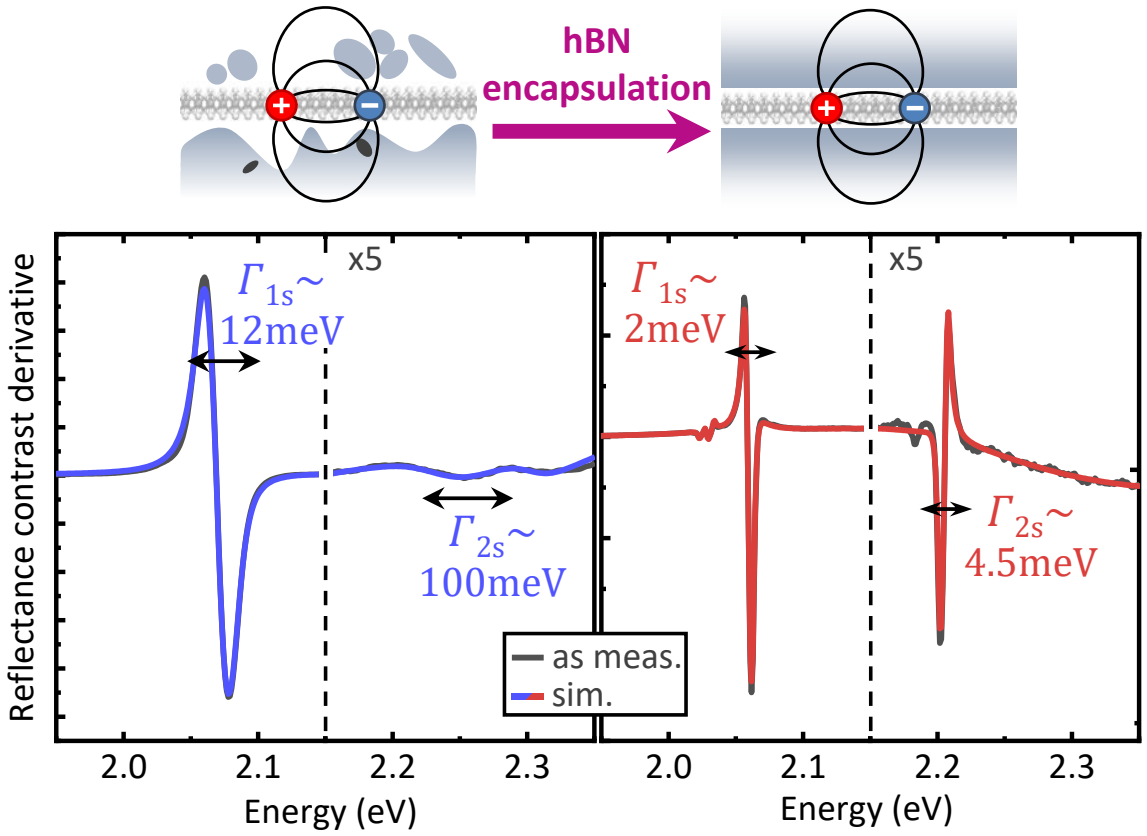

Figure 4.5: Top is an artist's impression of two different sample configurations. Left depicts a TMDC monolayer flake on a typical SiO_2/Si substrate with particles and residues adsorbed on top. Right is a hBN encapsulated sample with an idealized, perfectly homogeneous environment. Bottom shows representative first derivatives of reflectance contrast spectra, measured on WS_2 samples in the respective configuration at 4.2 K liquid helium temperature (gray). Also included are simulated spectra from a transfer matrix approach (colored). The estimated resonance broadening from non-radiative contributions is denoted by Γ_n for the respective n-th exciton state.

In our experiments we analyzed WS_2 samples of the above described configuration via linear optical reflectance spectroscopy in the energy range of the ground and first excited exciton state. The samples were additionally cooled to liquid helium temperature to drastically reduce contributions from homogeneous broadening via phonon scattering. Light from the spectrally broad tungsten-halogen lamp was focused to a FWHM of roughly 2 μm and the reflectance response was detected using the 300 gr/mm grating in combination with the CCD camera. Selected representative spectra of the reflectance contrast derivative with respect to the SiO_2/Si substrate are shown for both samples in the bottom of fig. 4.5. Also included are fitted simulated spectra using the transfer matrix approach described in sec. 3.3.1. These fits allow to estimate the purely non-

radiative broadening from the simulations, which is denoted by Γ_n for the n=1s,2s state. We find that the non-radiative linewidth of the ground state is bigger by a factor of about 6 with a difference of roughly 10 meV in the bare sample on SiO_2 (Γ_{1s}^{bare} ∼12 meV) as compared to the encapsulated sample (Γ_{1s}^{encap} ∼2 meV). Interestingly, this difference in linewidth between the samples is drastically more pronounced for the first excited state. Here, the ratio yields $\Gamma_{2s}^{bare}/\Gamma_{2s}^{encap} \approx 22$, with non-radiatively broadened 2s resonances of ∼ 100 meV and ∼ 4.5 meV for the bare and encapsulated samples respectively.

Let us first focus on the bare sample on SiO_2 and investigate the pronounced broadening of the 2s state. In the first instance such an enhanced broadening of a higher excited state can be excluded to stem from homogeneous broadening. For this purpose, we refer to a previous work, where we investigated the homogeneous broadening mechanisms in a joint theory-experiment study (Ack. 7,[92]). While this work was performed on WSe_2, we remark that due to their general similarities in the band structure, identical arguments apply for the case of WS_2. Fig. 4.6 presents theoretical calculations of the predicted purely homogeneous broadening for both the ground (left) and first excited state (right) with respect to temperature. The contributions of different scattering channels are indicated by color. The calculations are additionally supported by experimentally obtained homogeneous linewidth from white light reflectance measurements, depicted as black dots. Note that contributions of radiative broadening can be neglected for the here considered case, since the extracted broadening Γ_n only includes non-radiative broadening (see sec. 3.3.1). It is found that, in general, the 2s state has additional non-radiative scattering channels via phonon emission (i.e. into lower states), which would intuitively suggest a more pronounced broadening. However, due to these states' larger spatial extent, their k-space wave functions are narrower. This, in turn, leads to a reduced wave function overlap of initial and final state in momentum space and consequently, also a reduced phonon scattering efficiency is expected. As can be seen, this largely counterbalances the increased number of scattering channels, resulting in the predicted homogeneous broadening for 1s and 2s states being of comparable magnitude [92]. We emphasize, however, that contributions of non-radiative homogeneous broadening from scattering into energetically lower lying (dark) states still constitute a theoretical lower limit for the non-radiative linewidth in tungsten-based monolayers [24, 92].

As a result, this non-equivalent broadening of resonances can be attributed to stem from inhomogeneous contributions, in particular introduced by disorder and inhomogeneities in the environment. As discussed in sec. 2.3.2, resulting fluctuations in the dielectric constants of the surroundings are then expected to lead to an inhomogeneously broadened resonance of the exciton ensemble. Here, the observed pronounced

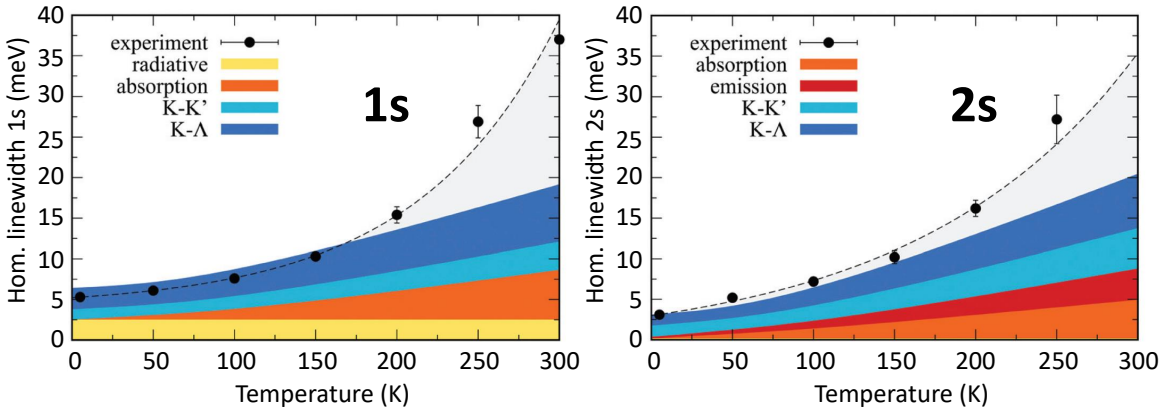

Figure 4.6: Adapted from our collaborative work [92]. Temperature dependence of the homogeneous linewidth broadening for ground (left) and first excited state (right) in WSe_2. Colored areas correspond to theoretical calculations of the contributions from different scattering channels. Yellow is the radiative broadening, blue the scattering into lower lying dark exciton states, orange and red are scattering with phonons under absorption and emission respectively. Also included are experimental data from white light reflectance measurements.

2s broadening can then be traced to the fact that such dielectric disorder has a stronger effect on higher excited states, due to their comparably lower absolute binding energies [132]. Note that other potential sources of disorder, which could induce a broadening of resonances, can be largely excluded, as further discussed in sec. 4.2.4.

In the context of this broadening mechanism having its origin in dielectric disorder, it is especially interesting to consider the measurements on the encapsulated sample. In this sample the non-radiative linewidths of both states are on similar orders. This implies that, compared to the bare monolayer, dielectric disorder is dramatically reduced, which can be understood as hexagonal boron nitride generally providing more homogeneous surroundings [214, 215, 227]. At the same time it further supports the picture of an encapsulation with high-quality boron nitride, being able to effectively suppress disorder introduced by the substrate. Furthermore, we find that the linewidths are not only of similar magnitude but in addition significantly narrowed for both resonances. This conveys that broadening from dielectric disorder constitutes a major source for observed resonance broadening and can even dominate the overall resonance broadening at low temperatures, where homogeneous broadening from phonon scattering is suppressed. From there we find motivation to further examine the possibilities to suppress such disorder in a controlled way.

4.2.2 Suppression of nanoscale disorder

To investigate the suppression of dielectric disorder more quantitatively, a systematic series of many 100's of individual reflectance contrast measurements on the encapsulated sample was performed. For this purpose, the automated stage was used to scan the sample in a predefined 25x25 μm pattern, as depicted in fig. 4.7 (a), taking reflectance spectra in equidistant 1 μm steps. However, due to time constraints from the need to keep the sample sufficiently stable under cryogenic conditions, the signal was only averaged over three individual frames for each measurement. The resulting reflectance contrast spectra and their derivatives were analyzed by using the automated fitting algorithm based on the transfer matrix approach described in sec. 3.3.1. This allows to extract parameters, such as non-radiative linewidth, energetic position and oscillator strength of each individual excitonic resonance and to plot them with respect to their spatial coordinate. Resulting 2D color plots are presented in fig. 4.7 (b) and (c) for the non-radiative linewidth of the 1s and 2s state respectively. Spectra where the fitting procedure was not applicable are left out and labeled with N/A. The reason for that is often found in these positions containing an accumulation of residues between individual layers (usually visible as orange specs, i.e., in fig. 3.2) and as a consequence they exhibit strongly disturbed spectra. Here, fitting of the 2s state is more sensitive to such disturbances due to its overall lower oscillator strength. It is found that the broadening of the two resonances is dramatically suppressed over many 10's to 100's of μm^2, indicating that hBN encapsulation can indeed provide a way to significantly suppress surface disorder on a large scale. Furthermore, it is shown that the linewidth of the two resonances is in general strongly correlated over the whole investigated area. However, some parts show a slightly more pronounced broadening, with this effect yet again more pronounced for the 2s state compared to the ground state (note the different color scales), indicating small amounts of residual dielectric disorder. This is particularly pronounced around areas where fitting was not applicable at all and residuals from the before mentioned impurity accumulations between layers might cause such effects.

To further study this, the data can be used to statistically analyze the non-radiative broadening ratio of the two states plotted in fig. 4.7 (d). Here, Γ_{2s} is plotted with respect to Γ_{1s} for each individual measurement. The 90% confidence intervals are indicated by dotted lines, yielding roughly 5 meV for the 1s and about 16 meV for the 2s state. The average values of broadening from this data set are 3.8 meV for the ground state and 10.2 meV for the excited state. The red dotted line indicates a slope of $\Gamma_{2s}/\Gamma_{1s} = 2.3$, which properly describes the broadening ratio for the majority of the measured spectra, in particular for positions with overall narrow linewidth.

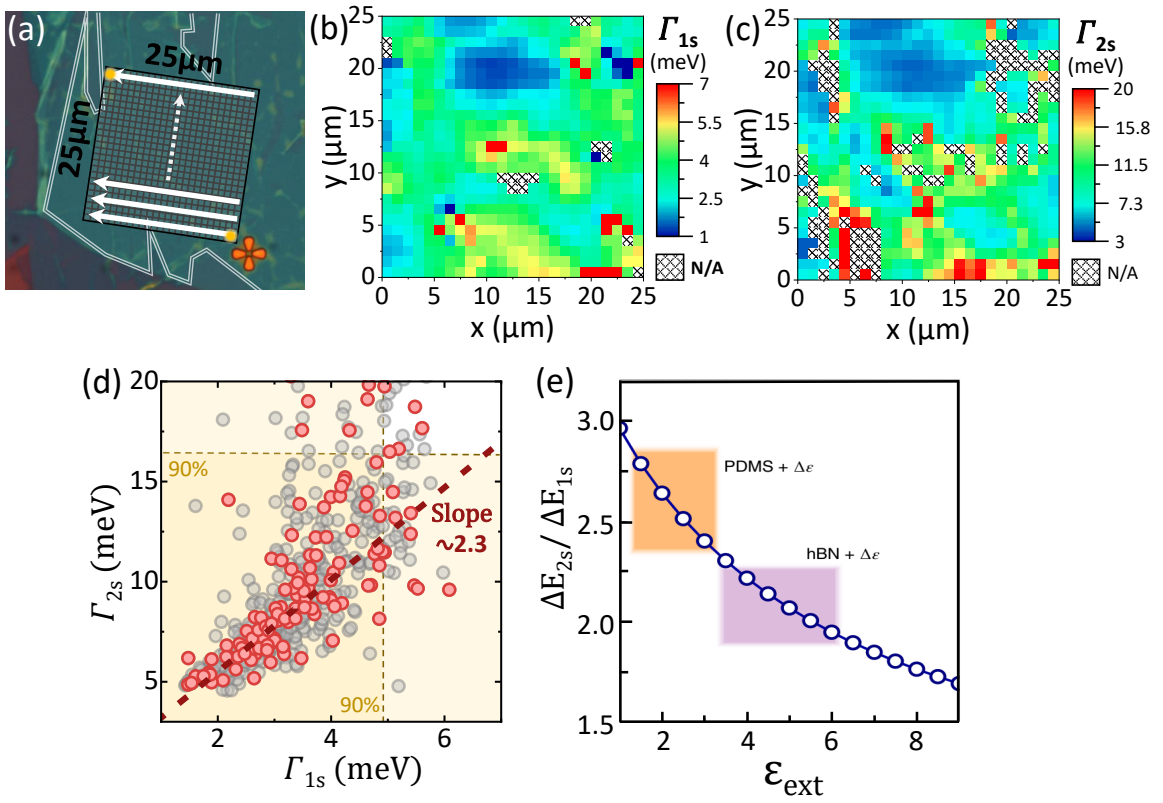

Figure 4.7: (a) The black grate illustrates a patterned measurement procedure on the hBN-encapsulated WS_2 sample (white framed area). The sample is scanned in a patterned 25x25 μm area from right to left and reflectance spectra are acquired every 1 μm. (b) and (c) are maps from analyzing each of the spectra with the automated transfer matrix fitting procedure and extracting the inhomogeneous broadening of the 1s and 2s exciton state respectively. Note the different energy scales for the color coding of the linewidth. Measurements where the fitting procedure was not applicable are denoted by N/A. (d) Statistical plot of the linewidth ratio (Γ_{2s} vs Γ_{1s}) for each individual measurement. The 90% confidence intervals for the two parameters are indicated and a linear slope with an incline of 2.3, describing the general trend of the linewidth ratio, is included. (e) Adapted from [132]. Theoretical calculation of the ratio of relative energy shifts of 1s and 2s states with respect to the dielectric constant of the environment. Typical screening ranges of hexagonal boron nitride and PDMS are indicated.

We can compare this value to theoretically predicted values for different surroundings, depicted in Fig. 4.7 (e). Presented is the calculated ratio of the resonance energy shift $\Delta E_{2s}/\Delta E_{1s}$ with respect to the dielectric constant of the environment. The plot thus indicates how much the 2s resonance would shift compared to the ground state, given a dielectric constant of the environment and then introducing fluctuations of this constant, i.e., due to dielectric disorder. Note that this ratio of resonance energy fluctuations is equivalent to the ratio of inhomogeneous linewidth broadening, since fluctuations in the resonance energies ΔE_n in an exciton ensemble are exactly the ori-

gin of such broadening (see sec. 2.1.3). Indicated by color are areas for hBN and PDMS dielectric constants. We find that the ratio of linewidth broadening of $\Gamma_{2s}/\Gamma_{1s} \approx 2.3$ from (d) indeed fits very well to the theoretically predicted value for a hBN dielectric constant slightly above 2. The average dielectric constant of the sample therefore is well described by the dielectric constant of the surrounding hexagonal boron nitride, further confirming proper interlayer contact. Slightly correlated residual broadening is thereby in good agreement as originating from leftover dielectric disorder. Here, the indicated confidence intervals for the linewidth distribution in fig. 4.7 give means to estimate its magnitude for the individual states. Finally, it is of particular interest to remark that, in considerably large areas of the sample (blue area in the top of fig. 4.7(b) and (c)), the encapsulation is able to almost entirely suppress any inhomogeneous broadening. This becomes apparent when considering that the estimated non-radiative homogeneous contributions alone should account for the observed broadening on the order of only a few meV, as can be seen in fig. 4.6.

4.2.3 Probing disorder fluctuations on the microscale

We have so far only discussed disorder fluctuations on scales below areas that are typically probed in a single measurement. However, it is important to acknowledge that suppressing disorder on the nanoscale does not mean that all disorder in the sample has to be suppressed. We thus turn to using the systematic scanning approach to allow for a comparative study of individual measurements, providing a way to investigate dielectric disorder on larger scales. However, while the resonance linewidth was a good parameter to investigate fluctuations inside the probed area, it hardly holds information on the absolute dielectric screening from the environment, especially for suppressed nanoscale disorder. In this case, as stated in sec. 2.3.2, the linewidth of each individual spectrum will be equivalent, regardless of the dielectric constant of the surroundings. For this purpose, we now track shifts in the absolute resonance energies and calculate the separation of ground and first excited state $E_{2s} - E_{1s}$ for each individual measurement. This parameter is sensitive to absolute changes in the average dielectric environment, while at the same time energy fluctuations from other effects, such as strain (see next section), which affect both states similarly, cancel out. From this parameter we therefore find access to examine fluctuations of the surroundings' average dielectric constant on the microscale.

At the same time it also gives means to estimate the exciton binding and bandgap energies. In this context, we refer to recent literature observations [28], where the energy scaling of an experimental exciton Rydberg series in hBN encapsulated WSe_2, has been closely reproduced by solving the Schrödinger equation, using an approximate thin-film

potential in form of eq. 2.4. As stated in sec. 2.1.3, such a model of accurately scaled exciton state separations then allows to extrapolate the exciton binding energy of each individual state. Here, we use these calculations to extract a prefactor that relates the 1s binding energy to the 1s-2s energy separation as $E_{b,1s} = 1.3 \times (E_{2s} - E_{1s})$. We assume that the obtained scaling-factor is comparable in the studied WS_2 system, given the scaling of excitonic states is similar to that of WSe_2, as shown in our magnetic field measurements. This is further supported by the fact that effective masses [56, 119], as well as Coulomb effects [24] are similar for both systems. Additionally, we state that, while this scaling-factor is in principle a function of the dielectric constant, it is very well approximated to be constant for only slight fluctuations of the dielectric constant. From this estimation of the 1s binding energy the optical bandgap is simply given as $E_g = E_{1s} + E_{b,1s}$.

Using these relations, fig. 4.8 (a)-(c) present the relative 1s exciton transition, as well as the relative estimated 1s binding and bandgap energies for the above investigated sample, with respect to the spatial coordinate. We find that the 1s energy generally shows only slight energy fluctuations over the whole sample. The bandgap displays closely correlated energy fluctuations, while the binding energy is very homogeneous over the whole investigated sample area. A simplified energy scheme of this finding is illustrated in fig. 4.8 (d). From the constant binding energy can be deduced that, in addition to the nanoscale disorder, disorder on a lager scale is also strongly suppressed in this sample. The result is an overall large-scale, homogeneous dielectric environment. The remaining microscale fluctuations found in the 1s transition energy are then most likely due to effects that do not effect the Coulomb interaction strength, such as strain or doping effects, that will be further discussed in the next section.

Fig. 4.8 (e)-(g) depicts the same parameters as (a)-(d) but for a different encapsulated WS_2 sample. Note that here a bigger area is investigated and the energy scale is adjusted. All individual spectra have narrow linewidth (not shown), indicating suppressed nanoscale disorder. In the first instance we find that the 1s transition energy is more or less homogeneous over the whole sample. In contrast to the previous scenario, however, the bandgap no longer has the same dependence of energy shifts with regard to the sample position, but rather shifts in accordance with the microscale fluctuations observed in the binding energy. While this indicates a locally different average dielectric constant, we do find plateau-like larger areas where the binding energy is constant. It can be followed that, also here, the encapsulation can heavily reduce the dielectric disorder on a nanoscale, but disorder on a larger scale is still present. The average dielectric constant of the environment is constant over larger areas but can still fluctuate between these regions. We also note that generally, the region amidst such plateaus

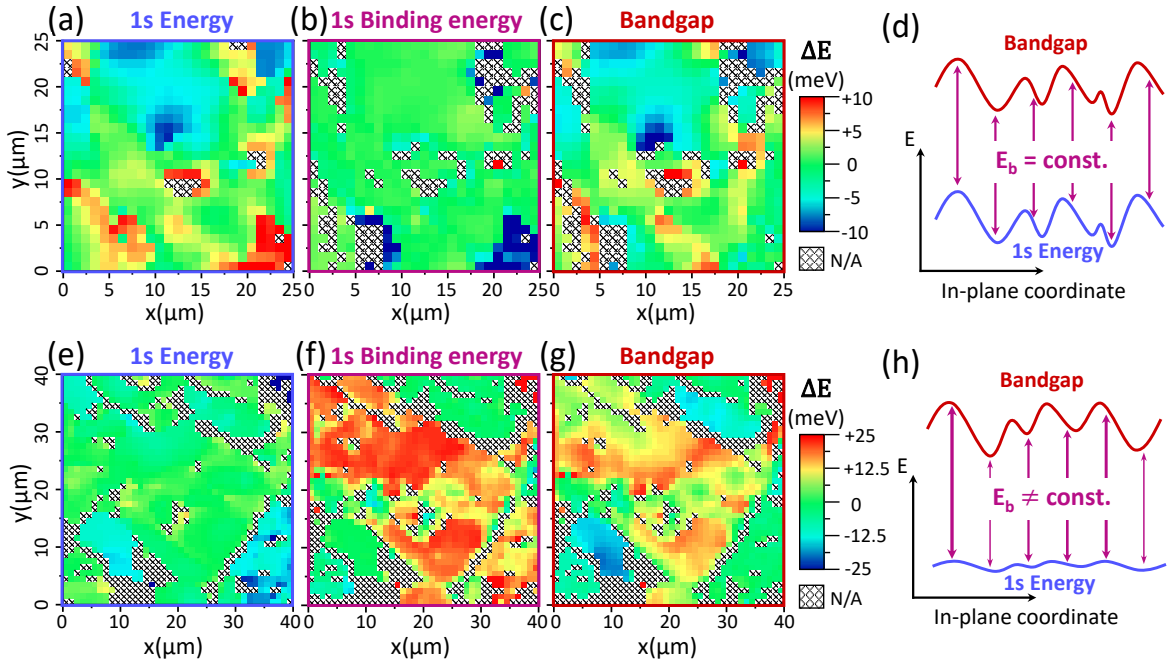

Figure 4.8: (a)-(c) 2D spatial plots of the relative 1s transition, binding and bandgap energy of the encapsulated sample depicted in fig. 4.7. Binding energy and bandgap are estimated from the 1s-2s resonance separation. (d) Schematic illustration of completely suppressed nanoscale dielectric disorder, where the bandgap essentially shifts in accordance with the 1s energy and the binding energy is constant over the whole investigated area. (e)-(g) Analog energy maps as in (a)-(c) for a different encapsulated WS_2 sample, where microscale disorder is present. Note the different size of the investigated area, as well as the different energy scale. (h) Bandgap and 1s energy now have different energy shifts depending on the sample position, due to a non-constant binding energy from micro scale fluctuations in the surroundings's dielectric constant.

can be difficult to analyze. In such cases, it is likely to find exciton resonances from both areas contributing to the overall measured signal. When these contributions are of similar magnitude, this results in two resonances from the same state being observable in the spectra, energetically split due to the different dielectric surroundings the excitons are exposed to. In the used fitting algorithm this can not be included, leading to an accumulation of 'not applicable' data points in interface areas of different dielectrics. A good example of such a region is found in the top right of fig. 4.8 (f). Furthermore, this also indicates that the transition between those regions can be rather sharp, at least below the resolution of our white light probe ($\sim 2\,\mu$m). From this we conclude that, upon hBN encapsulation, it is important to take into account that disorder on larger scales can still be present, although linewidths are significantly narrowed from suppressing disorder on the nanoscale. Considering such disorder can be particularly important when using large probing spots or investigating exciton properties, such as propagation, where a homogeneous environment on larger scales is of relevance.

4.2.4 Conventional sources of disorder

As already addressed above, there are other, more conventional sources of disorder besides the dielectric environment, that are well known to influence the energetic positions as well as the linewidth of excitonic resonances depending on their spatial coordinate. Such parameters include strain of the sample [229–234] or non-uniform intrinsic doping of the material [24, 29, 103, 235] and their relevance in the context of this work shall be discussed in the following.

Strain induced disorder

Straining of monolayer TMDCs is known to lead to shifts in the underlying free-particle band structure of the material [236–238]. The resulting shifts of exciton resonances can be as large as many 10's of meV/% [231, 232], however, all excitonic resonances are generally effected very similarly and effects on the binding energy are comparably small on the order of only 5-10 meV/% [239]. Additionally, the strain induced broadening effects on the excitonic linewidths are also expected to be comparable for all resonances and are found to be of homogeneous nature [233, 234, 240]. In contrast to that, the observed energetic shifts upon encapsulation in our experiments mainly effect the binding energy and, as stated above, the linewidth broadening is significantly different for the two observed exciton states (see fig. 4.5). To give an example, the observed resonance shift in the 1s state alone would require strain effects on the order of 0.25%. This, however, would only lead to a strain induced broadening on the order of 2-3 meV, being in stark contrast with our observations. As a consequence, we find that our observations are clearly not consistent with strain induced disorder. We can therefore exclude it to be the main source of the observed disorder effects. Note that, with analogous reasoning, strain can also be excluded as the origin for the microscale disorder of the second investigated sample. However, we remark that small effects of strain can still be present and be partially responsible for the observed residual disorder, in particular considering small correlated resonance shifts found in the samples.

Disorder from locally fluctuating doping concentrations

Substantial levels of (intrinsic) doping can lead to shifts of exciton resonances and coulombic renormalization of the bandgap [24]. Local fluctuations in the doping concentration could thus also be a source of potential disorder. In order to investigate the role of doping on the residual disorder in our experiments, we return to the analysis of reflectance measurements. Signatures we attribute to trion resonances in these spectra allow us to estimate the level and the influence of doping on the exciton resonances. Note that in literature the signals of these resonances are also labeled as attractive

Fermi-polarons, particularly in the case of significantly high doping levels [241]. Since both exciton and trion oscillator strength are influenced by the doping level [103], the ratio of trion to exciton oscillator strength f_{trion}/f_{ex} can serve as an indicator of the doping level.

We first study the sample with suppressed nano- and microscale disorder of fig. 4.8 (a)-(d). While in this sample most disorder effects are suppressed, there still is a residual amount linewidth broadening, as indicated by the confidence intervals in fig. 4.7 (d). Thus, alternative sources, such as doping fluctuations, should be considered. For this purpose, an exemplary spectrum of this sample is shown in fig. 4.9. On the low energy side of the 1s resonance a typical doublet resonance of the singlet and triplet trion [105], split due to short range exchange interactions, is clearly observed. The oscillator

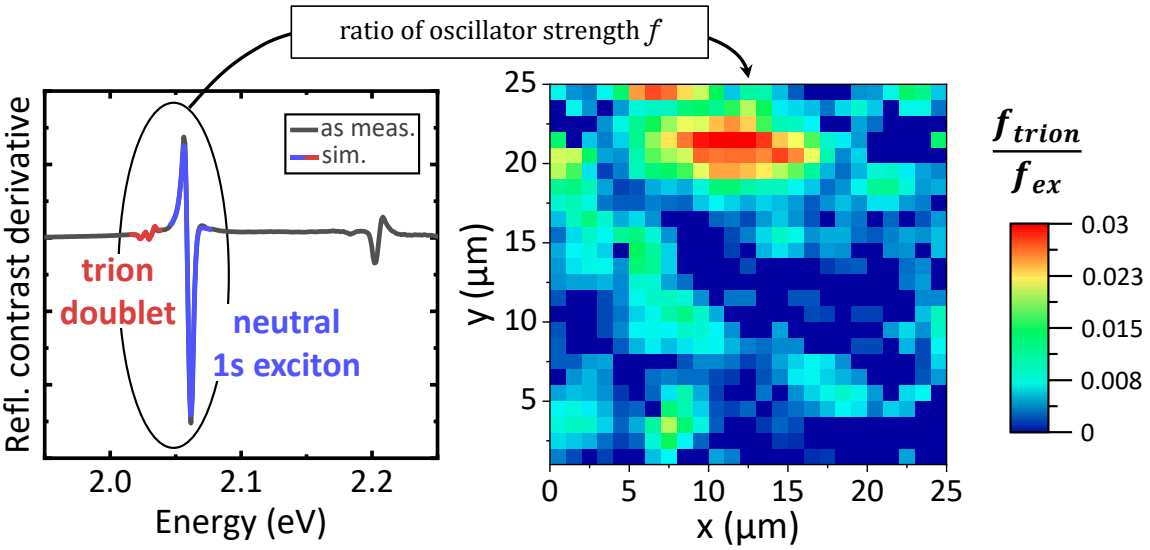

Figure 4.9: Left shows the derivative of a representative reflectance contrast measurement acquired on the encapsulated WS_2 sample with suppressed nano- and microscale disorder. Simulated fits using the transfer matrix approach are included and resonances of the trion doublet and 1s exciton are indicated by different coloring. Right shows a map of the ratio of combined trion to 1s exciton oscillator strength, extracted from the fits of each measured spectrum.

strength of trion and 1s exciton resonances (indicated by color) are extracted from the fits of simulated spectra, using the transfer matrix approach. The spatial fluctuations of the doping concentration are visualized on the right-hand side of fig. 4.9. Here, the ratio of combined trion to 1s oscillator strength with respect to the spatial coordinate is presented. First, the overall doping concentration of the sample can be considered to be rather low, with even the highest level of doping exhibiting an oscillator strength on the order of only about 3 % of the 1s exciton's. Moreover, comparing the spatial

doping fluctuations with the residual fluctuations of the bandgap (fig. 4.8 (d), we do not find any correlations. Following from that, doping in this sample can be excluded as a source of significant disorder. The residual disorder in this sample is therefore most likely to stem from effects of strain or leftover disorder in the dielectric environment.

Lastly, we consider the sample we stated to have pronounced fluctuations in the binding energy, attributed to microscale disorder in the dielectric environment. Three representative positions with different binding and bandgap energies, depicted in fig. 4.10 (a), are chosen. The corresponding reflectance contrast derivatives are shown in (b), including fits from simulated spectra, where the colors indicate contributions from different resonances. Note that the high energy part of the spectrum in the range of the 2s state is slightly smoothed for better visibility. The resonance energies are additionally indi-

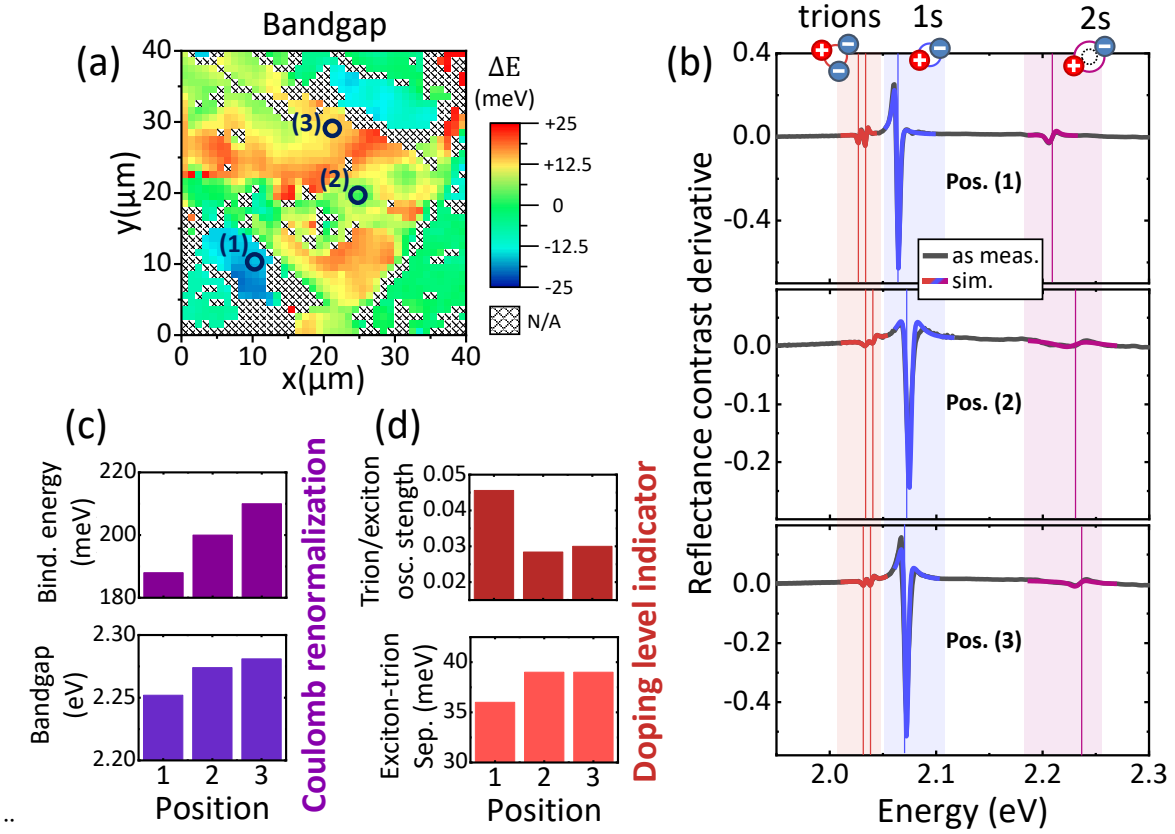

Figure 4.10: (a) Spatial map of the bandgap (same as fig. 4.8 (g)). Indicated are three representative positions with differing bandgap energies. (b) Corresponding 5K reflectance contrast derivatives of the indicated positions. Fitted simulations are included in different colors for each of the resonances. The vertical lines mark the individual resonance energies. (c) Binding and bandgap energies extracted from the fits for each of the three positions. (d) Corresponding relative oscillator strength of the trion doublet with respect to the 1s exciton resonance and energetic separation of low-energy trion and 1s resonance.

cated by vertical lines for each of the three positions, showing a more pronounced energy shift of the 2s state compared to 1s and trion resonance shifts. Fig. 4.10 (c) shows the corresponding binding and bandgap energies extracted from the fitted simulations and serve as a gauge for the Coulomb renormalization [24]. Fig. 4.10 (d) then depicts the relative oscillator strength of the trion doublet compared to the 1s exciton resonance, as well as the separation of the low-energy trion and 1s exciton resonance. Both serve as indicators for the doping level of the sample [103]. Again we find that, generally, the doping level can be considered to be relatively low. Additionally, neither of the indicators for the Coulomb renormalization and the doping level show any correlation. Thus, also in this sample the influence of doping is found to have negligible influence on the overall disorder that leads to observed local fluctuations of binding and bandgap energies.

In conclusion, having also considered alternative sources of disorder, we find further support for dielectric disorder in the environment being the main source of disorder in TMDC monolayers. Encapsulation in high-quality hexagonal boron nitride provides a convenient way to significantly suppress such disorder over considerably large areas, in particular on the nanoscale. This leads to a narrowing of the resonance linewidth, especially significant for higher excited states. Furthermore, the introduced method of systematic white light scanning of sample areas provides an efficient tool in evaluating the quality of disorder suppression, also with respect to other sources of disorder, such as intrinsic doping. In addition, it allows to investigate disorder on larger scales than the areas typically probed in photoluminescence experiments. We find that here, dielectric disorder can still be present. This can give rise to sharp interfaces of areas with contrasting dielectric surroundings, resulting in different Coulomb interaction strengths. Following from that, exciton binding and bandgap energies can vary by multiple 10's of meV over scales of only few μm, which can be of relevance for measurements that are sensitive to larger spatial scales.

4.3 Exciton transport in disorder-free structures

In the third segment of the experimental part of this work we will focus on another intrinsic property of excitons, that is their propagation. While propagation of excitons has been thoroughly investigated in conventional two-dimensional quantum well systems [35, 139, 142, 242], it has also been shown that excitons in monolayers of TMDCs can efficiently propagate over 100's of nanometers within their confined two dimensions [39, 138, 144, 146, 243]. Here, it is interesting to consider that the high binding energy of excitons in these systems allows to study their diffusive behavior at ambient conditions. Furthermore, it has been demonstrated that propagation can additionally be guided by strain and dielectric gradients [244–246], while it has also been found that exciton propagation generally is governed by intriguing non-linearities that can be attributed to efficient interaction effects [143, 147, 247–249]. In a previous work [40] we have also investigated and discussed such non-linear density dependence of exciton diffusion in bare monolayer samples deposited on SiO_2/Si substrates. Now, in the following study, we utilize the findings of the previous segment and mainly focus on the transport dynamics of excitons in disorder-free monolayer samples, where influences from and interactions with inhomogeneities in the environment are strongly suppressed.

In the first part we demonstrate that this allows to give insight into additional non-trivial density dependencies in the exciton diffusion efficiency, which were previously obscured by effects of disorder. In particular, the regime of very low exciton densities is investigated and a model for the potential influence of free charge carriers, present at sufficiently high temperatures, on a resulting composite exciton-plasma diffusion is introduced. Additionally, the narrow linewidth of the disorder-free samples allow to spectrally separate individual exciton resonances at low temperatures. This provides a way for a more detailed analysis of exciton transport by separately studying the propagation dynamics of individual exciton resonance. In the second part of this segment we make use of this by focusing on the long-lived photoluminescence emission from phonon sidebands of dark exciton states. This allows to investigate temperature dependent exciton propagation dynamics under cryogenic conditions, which were previously hard to access due to the bright excitons exhibiting extremely short lifetimes on the order of $\leq 1\,\mathrm{ps}$ at such temperatures.

4.3.1 Exciton propagation dynamics under ambient conditions

We will first turn to the investigation of exciton transport under ambient conditions in disorder-free samples. Different hBN-encapsulated WS_2 flakes were studied, where the disorder of each flake was characterized by the white-light mapping approach and subsequent analyzing of the spectra introduced in the previous segment. From that,

the flakes and spatial positions for each of the following measurements were deliberately chosen to be in regions of well suppressed dielectric disorder. For the excitation of electron-hole pairs, the 100 fs pulsed Ti:Sa laser was tuned to 2.43 eV off-resonant excitation and focused onto the sample using a 100x magnification lens. The resulting excited two-dimensional Gauss profile yielded an initial FWHM of 0.5 μm. The photoluminescence response of the samples was first spectrally resolved on the CCD camera, using the 300 gr/mm grating of the spectrometer. From the obtained spectrum depicted in fig. 4.11 (a), it is confirmed that the photoluminescence signal of an hBN-encapsulated WS_2 monolayer at ambient conditions is dominated by a single peak, corresponding to the exciton ground state transition.

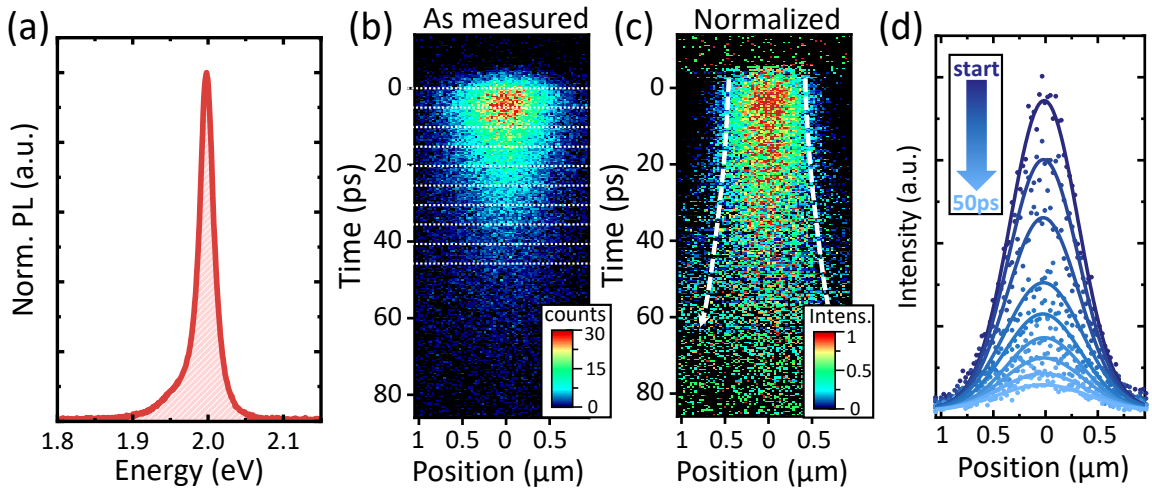

Figure 4.11: (a) Typical normalized photoluminescence spectrum of a hBN-encapsulated WS_2 monolayer under ambient conditions. The single peak at roughly 2.0 eV resembles the exciton ground state transition. (b) Streak camera image of the time- and spatially resolved photoluminescence as measured. Dotted lines indicate the temporal slices used for the Gauss fits in (d). (c) Corresponding normalized streak camera image. The dotted lines serve as guide to the eye for the spatial broadening of the signal. (d) Spatial profiles extracted from the temporal slices indicated by dotted lines in (b). Circles are the data as measured, while solid lines are Gauss fits to the data for extracting the spatial broadening.

To study the time- and spatially resolved dynamics of these exciton states, the emission response was then guided onto the streak camera sensor in spatial resolution, using the mirror inside the spectrometer. A representative streak camera image of such a measurement is shown in fig. 4.11 (b), with the spatial coordinate resolved on the x-axis and temporal resolution on the y-axis. Here, the signal is mainly dominated by the photoluminescence decay, given by the finite lifetime of the excited electron-hole pairs. To compensate for the lifetime induced signal loss, fig. 4.11 (c) presents the corresponding

streak camera image, normalized for each individual time step. This allows to visualize the spatial broadening with time as illustrated by the dotted lines, serving as a guide to the eye. Fig. 4.11 (d) then presents the spatial density profiles, extracted from temporal slices of the measurements, illustrated in (b) by dotted lines. For each of the profiles a Gauss fit is included in solid lining that allows to extract the time-dependent squared Gauss width $w(t)^2$, as described in sec. 3.3.2.

Multiple measurements on three different sample flakes for a range of various excitation powers were carried out. To calculate the corresponding excited electron-hole pair density, an absorption of 4.5 % in the relevant energy range was assumed. This value was obtained using the transfer matrix approach to extract the absorption of the encapsulated samples from simulated fits to white light reflectance measurements. From this the total densities of injected electron-hole pairs N_{tot} were estimated to be in the range of 3.2x10^8 to 6.3x10^{10} cm^{-2}. We remark that in the case of encapsulated WS_2, this range is generally below densities where significant influences of non-linear effects are expected [148, 150, 153, 250]. For every measured density the broadening of the squared Gauss width was extracted from the time- and spatially resolved photoluminescence response. The obtained results are displayed in fig. 4.12 (a).

Here, the relative broadening of this squared Gauss width is plotted as a function of time. For better visibility only selected representative measurements for each density are shown and the data are vertically offset. The straight lines are purely linear fits to the data that are used to extract the diffusion coefficients according to eq. 3.13. Already here, a trend of decreasing diffusion coefficient with injected electron-hole density can be estimated from the decreasing incline of the fits. This is better visualized in fig. 4.12 (b), where the extracted values of the diffusion coefficients from all conducted measurements are presented. Also included are the averaged values depicted as filled circles. The shaded area serves as a guide to the eye for the general density dependency of the diffusion coefficient. We find that the average value for very low densities between 3.2x10^8 and 5x10^9 cm^{-2} is roughly around 6 cm^{2}s^{-1}, with values reaching as high as 10 cm^{2}s^{-1}. For further increasing densities, the diffusion coefficient shows a tendency to decrease to an average value of around 2 cm^{2}s^{-1}. We yet again emphasize that over the here investigated density regime Auger-like exciton-exciton annihilation effects can be neglected due to this process being significantly suppressed in hBN-encapsulated samples [153, 250]. Additionally, such effects have been found to lead to an apparent increase of the effective diffusion coefficient [40], rather than the here observed decrease. This is further confirmed by the measured lifetimes depicted in fig. 4.12(c), showing only marginal density dependence up to densities of roughly 10^{13} cm^{-2}, in good agreement with literature values [250].

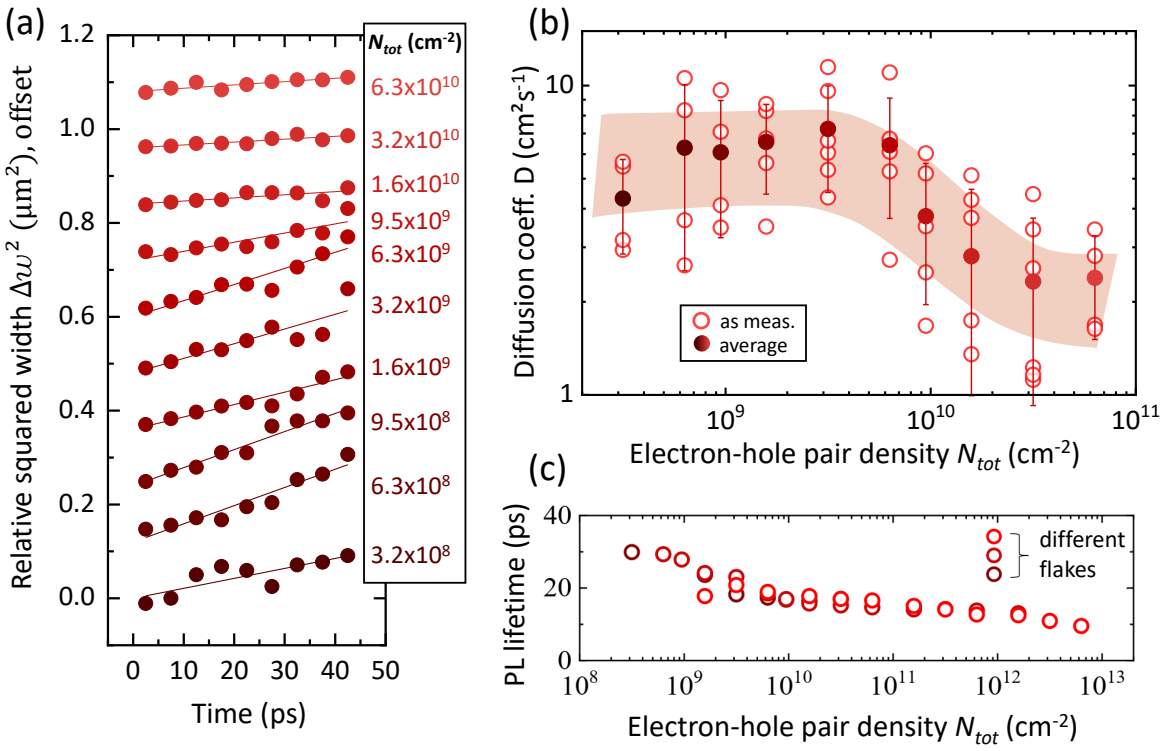

Figure 4.12: (a) Selected representative relative squared Gauss width as a function of time, extracted from time- and spatially resolved photoluminescence measurements on a hBN encapsulated WS_2 monolayer with suppressed disorder. Data for different pump densities resulting in comparably low exciton densities of 3.2x10^8-6.3x10^{1}0 cm^2 are vertically offset for clarity. Purely linear fits for the extraction of diffusion coefficients are included. (b) Diffusion coefficients as a function of electron-hole pair density. Individual measurements of several samples and different sample positions are shown (open circles) and the average values are included (filled circles). The shaded area serves as a guide to the eye for the general density dependence of the diffusion coefficient. (c) Exciton photoluminescence lifetime as a function of electron-pair density for several sample flakes. Also higher densities are included for illustrative purposes.

Before investigating this peculiar decrease of the diffusion coefficient more thoroughly, we turn our attention to the generally efficient diffusion found in these disorder-free samples. Comparing the extracted values in the range of 2-10 cm^{2}s^{-1} to our studies of disorder afflicted monolayers on bare SiO_2/Si substrates in the linear diffusion regime, this constitutes an increase in efficiency of more than one order of magnitude [40]. It is therefore found that disorder in the environment has important consequences not only for excitonic resonances but also significantly affects exciton propagation dynamics. This further implies that controlling or tailoring the dielectric environment of two-dimensional structures can provide a way to influence the transport of charge carriers in these structures. The diffusion lengths corresponding to these values can be calculated from eq. 2.13 and are on the order of 200-400 nm. Interestingly, this is

comparable to values obtained in non-encapsulated samples on SiO_2/Si substrates, although the diffusion coefficient in those samples is significantly lower [40]. At the same time, however, lifetimes then tend be be longer. From that, a correlation of decrease in lifetime and enhancement in propagation efficiency can be deduced. This, in turn, suggests that photoluminescence lifetimes in such samples are generally limited by trapping at non-radiative centers, intrinsic to the monolayer itself. As excitons in samples with suppressed disorder diffuse more efficiently, they can also encounter non-radiative trapping centers faster, leading to the observed reduction in lifetime compared to bare samples. In other words, this means that the diffusion length in our samples is generally limited by non-radiative traps, associated with lattice imperfections, which is also in good agreement with simple theoretical models that are discussed in more detail in [153].

4.3.1.1 Predicted exciton diffusion in disorder-free structures

While the possibility of enhancing diffusion by controlled suppression of dielectric disorder itself is an encouraging finding, we now turn our attention to the decrease of the diffusion coefficient in the here depicted density regime. As stated before, a non-linear behavior of the diffusion coefficient in this regime is not expected, since density depended effects, where exciton-exciton interactions start to play a more important role, should occur at higher densities. For a first approximation of a theoretically expected diffusion coefficient it is reasonable to consider a scenario where the diffusive character of the propagation is mainly defined by scattering with phonons, given their high population at room temperature [23]. In such a case the Einstein relation given in eq. 2.16 allows to roughly predict the diffusion coefficient [138, 143, 147]. Here, the exciton temperature can be assumed to be given by the lattice temperature of 300 K, with the cooling of non-resonantly injected excitons being fast compared to their lifetimes [251]. The scattering time $\tau_s = 30\,\mathrm{fs}$ is estimated from the photoluminescence linewidth using eq. 2.5. This is validated by the fact that the resonance broadening at room temperature is heavily dominated by homogeneous contributions from phonon scattering [23, 92]. Using reasonable total exciton masses between 0.5 and 1 of the free electron mass m_0 [56, 79–81], estimated diffusion coefficients between 1 and $2\,\mathrm{cm^2 s^{-1}}$ are yielded, significantly underestimating the measured diffusion coefficients of 5-10 $\mathrm{cm^2 s^{-1}}$ in the density regime below $5\mathrm{x}10^9\,\mathrm{cm^{-2}}$.

This apparent disagreement from a simple model motivates a more thorough and detailed investigation of the underlying physics. For this purpose, we resort to a more refined model, where all populated excitonic states that contribute to the observed overall diffusion of the exciton ensemble, are accounted for. In tungsten-based TMDCs

this specifically demands the inclusion of momentum- and spin-forbidden dark excitonic states. A schematic illustration of all involved exciton states is given in fig. 4.13 (a). Note that only one half of the existing relevant exciton states with the hole sitting in the K+ valley are shown. There is an identical set of exciton states with all signs flipped, from breaking of lattice inversion symmetry and the hole sitting in the K- valence band. For simplicity these states are omitted, but the same arguments apply. The observed photoluminescence stems from the spin-allowed, bright K+−K+ transition, depicted in yellow. However, in tungsten-based materials, as already stated in sec. 2.1.3, there are lower lying dark states that account for the majority of the exciton population illustrated by the shaded areas. We yet again emphasize that, due to the fast scattering of excitons compared to their lifetime at ambient conditions, the dark and bright exciton states can be assumed to be well intermixed. For this reason, emission from bright states is an adequate observable, representative for the propagation dynamics of the entire exciton ensemble.

In principle, here, one has to differentiate between the two dark excitonic states with different band structure contributions. Those, formed from K states in both conduction and valence band and heavier states formed from K states in valence and three-fold degenerate Λ states in conduction band. In both cases they are additionally split into exciton states with total spin 0 (singlets, solid lining) and with total spin 1 (triplets, dotted lining). Let us first consider the dark states solely made up from K-point contributions, that is K+−K+ triplet and K+−K- singlet states. The energetic splitting of these states compared to the bright K+−K+ singlet in WS_2 is well established from experiments [63]. Additionally, these values are in good agreement with theoretically estimated values of about 50 meV from solving the Schrödinger equation for an exciton in the thin-film approximation while taking values for the band splitting and masses from single particle calculations [56]. This splitting being larger than the thermal energy at room temperature of roughly 26 meV further supports the statement of dark states contributing the majority of the exciton population under ambient conditions. On the other hand, the splitting $\Delta_{K-\Lambda}$ between the bright exciton and the K−Λ states (that is both K+−Λ- singlet and K+−Λ+ triplet) is less precisely known, due to lack of experimental access to these states. Their energetic position in WS_2 thus relies on theoretical calculations from single-particle band structure offsets only and literature values vary over 10's of meV [56, 93, 98].

Turning to the microscopic calculations of the diffusion coefficient, we first note that singlet and triplet states of same energy are considered to be equivalent. This is due to these states' symmetry conditioning identical effective masses and energies, resulting in identical scattering and diffusion efficiency. The population of singlet states therefore

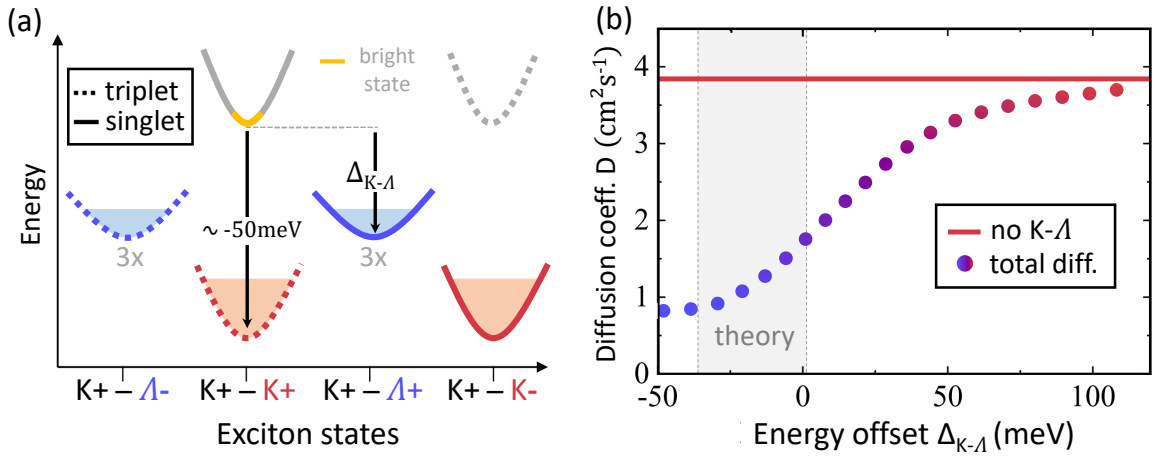

Figure 4.13: (a) Illustration of the excitonic band structure in hBN-encapsulated WS_2 monolayers. Included are the relevant excitonic states made up from electrons in the K± or Λ± valleys of the conduction band and holes in the K+ valley of the valence band of the single-particle band structure. States with total spin 0 are depicted in solid lines (singlet) and of total spin 1 in dotted lines (triplet). The expected occupation at room temperature is schematically illustrated by shaded areas and the three-fold degeneracy of the K−Λ states is denoted. $\Delta_{K-\Lambda}$ is the energy offset of these with respect to the bright K+−K+ state. (b) Filled circles are a calculation of the total exciton diffusion coefficient with respect to the energy offset $\Delta_{K-\Lambda}$. The solid line indicates the calculated exciton diffusion when only K−K (bright and dark) states are included. The shaded area illustrates the estimated values for $\Delta_{K-\Lambda}$ from conduction band offsets calculated in ref. [56].

diffuses in the same way as their energy-equivalent triplet population. Also, considering that spin-flip involving exciton-phonon scattering is expected to take place on long timescales [252], as compared to fast spin-conserving scattering [154], such processes are neglected in the calculations. The phonon modes taken into account therefore are the in-plane acoustic longitudinal and transversal (LA and TA) and optical (LO and TO) modes, as well as the out-of-plane A_1 modes at the Γ, Λ and K points [253].

The calculations were carried out by our collaborators from the Chalmers University (Ack. 7) in accordance with a previous work [254]. They were performed for a reasonable range of energy splittings $\Delta_{K-\Lambda}$, computing the total diffusion coefficient of excitons. To estimate diffusion coefficients, the calculations, in principle, follow along the same lines as the methods used in experiments (see sec. 3.3.2). Here, however, time- and spatially resolved evolution of the exciton density are obtained from evaluating equations of motion for the exciton occupation in different valleys, incorporating ab-initio parameters for the electronic [56] and phononic [253] properties of monolayer WS_2. These equations are set up by exploiting the Heisenberg equation and the many-particle Hamiltonian operator, while interactions of the carriers with phonons, photons and other carriers

are included (for details see ref. [254]). The diffusion coefficient is then extracted, from a linear fit to the temporal broadening of the squared Gauss width.

The resulting calculated total diffusion coefficient is presented in fig. 4.13 (b) as a function of the energy offset $\Delta_{K-\Lambda}$ of the K$-\Lambda$ states with respect to the bright K+$-$K+ state. In general, we find that the population of K$-\Lambda$ states can have a strong influence on the total exciton diffusion, depending on their energetic position due to their higher total exciton mass. In addition, serving as the theoretical upper limit, also the calculated exciton diffusion coefficient, neglecting any K$-\Lambda$ population, is included. Following from this model we find that the diffusion coefficient can in principle take values between 1 and 4 $\mathrm{cm^2 s^{-1}}$, depending on the energetic position of the K$-\Lambda$ state. Note that while these values can indeed slightly deviate from the simple model introduced above, they still underestimate the experimentally determined diffusion coefficients of 5-10 $\mathrm{cm^2 s^{-1}}$. This is even more so the case when considering more realistic values for the splitting of exciton states $\Delta_{K-\Lambda}$ from single-particle band offset values [56], illustrated by the shaded area.

We remark that contributions of fast, non-thermalized excitons can be excluded as a reason for the high measured diffusion coefficient, due to cooling times on the order of a few picoseconds [251, 254], being a lot shorter than the timescales for the exciton diffusion dynamics studied in the experiments. Thus, while an experimental finding of slower diffusion coefficients compared to theory can easily be attributed to effects of scattering with residual disorder or defects, the finding of a higher diffusion coefficient constitutes a discrepancy that is rather unexpected. In the following section we therefore consider an alternative source that can lead to an enhanced diffusion of optically excited charge carriers - the presence of a finite amount of free charge carriers (electron-hole plasma).

4.3.1.2 The Saha equilibrium under experimental conditions

In order to give a way of understanding the discrepancy of the experimentally determined diffusion coefficients being significantly higher than theoretically predicted values, we consider the importance that free charge carriers could have on the observed propagation dynamics. Interestingly, in these systems free charge carriers are indeed predicted to diffuse more efficiently, with a diffusion coefficient around 11 $\mathrm{cm^2 s^{-1}}$ [253]. In context of the composite diffusion model introduced in sec. 2.4.3, a sizable amount of electron-hole plasma in the total charge carrier population could therefore give rise to a potential source of this efficient diffusion as being driven by mobile free charge carriers. This puts forward the question whether such free charge carriers are expected to form under the given experimental conditions. For this purpose, we consider the scenario of an exciton-plasma equilibrium, as introduced in sec. 2.4.2, for the studied density

regime at room temperature. An exciton binding energy of around 200 meV in encapsulated WS_2 is assumed, in agreement with our experimental findings from reflectance measurements (see fig. 4.10 (c)). Additionally, we use literature values [56] for the band structure parameters and offsets and incorporate contributions of each relevant valley available for free electrons and holes, as well as the previously discussed exciton states. From this a Saha parameter of S=2.5x10^{8}cm^{-2} is obtained (for a full deviation of the mass action law and the Saha parameter in an arbitrary multi-band configuration see [153]). Utilizing eq. 2.22, the exciton fraction can then be calculated and is shown with respect to the experimentally accessed density regime in fig. 4.14 (a) as a dotted line. Also included, for illustrative purposes and considering experimental and theoretical uncertainties, are calculations where key parameters are varied in a reasonable range (10-30 %) : $\Delta M_{ex} = +0.3\, m_0$, $\Delta E_b = -20$ meV, $\Delta T = 15$ K, $\Delta_{K-\Lambda} = +23$ meV. The Saha parameter yielded from this is S=13x10^{8}cm^{-2} and the corresponding exciton fraction is shown as a solid line. Theoretical calculations in this and the next sections were performed in a collaborative work by colleagues from the Ioffe institute (Ack. 8).

It is found that for both Saha parameters the exciton fraction of the injected hole-pair ensemble is expected to change significantly over the investigated density regime. Moreover, the calculations predict that for the lowest densities of the experimental setting the charge carrier population should be almost completely dominated by the formation of free charge carriers. Over the range of roughly three orders of magnitude in density this will smoothly transition into an exciton dominated system, while for mediocre densities a coexistence of substantial fractions of both excitons and electron-hole plasma is expected. This confirms the necessity to consider a model of compound exciton-plasma diffusion to help understand the experimentally observed diffusion dynamics.

4.3.1.3 Experimental compound exciton-plasma diffusion

With respect to these findings the model of coupled exciton-plasma diffusion of sec. 2.4.3 is used to obtain a theoretical estimation of the diffusion when including the presence of free charge carriers. For that purpose the compound diffusion equation (eq. 2.24) is numerically solved with the initial starting parameters (t = 0) for the density profile and total injected charge carrier density set to those found in the experimental settings. The composite exciton-plasma diffusion coefficient is calculated from eq. 2.25. Here, the diffusion coefficient used for free charge carriers is taken as D_{eh}=11 cm^{2}s^{-1} from literature [253], as stated above. The diffusion coefficient for the exciton species is set to D_{ex}=1 cm^{2}s^{-1} from fig. 4.13 (b) for the parameter $\Delta_{K-\Lambda}$= -26 meV in the middle range of reported literature values. Density dependent exciton and plasma fractions are taken from the calculations of the previous section. The population lifetime is calculated in similar fashion. From the resulting time and position dependent density distribution

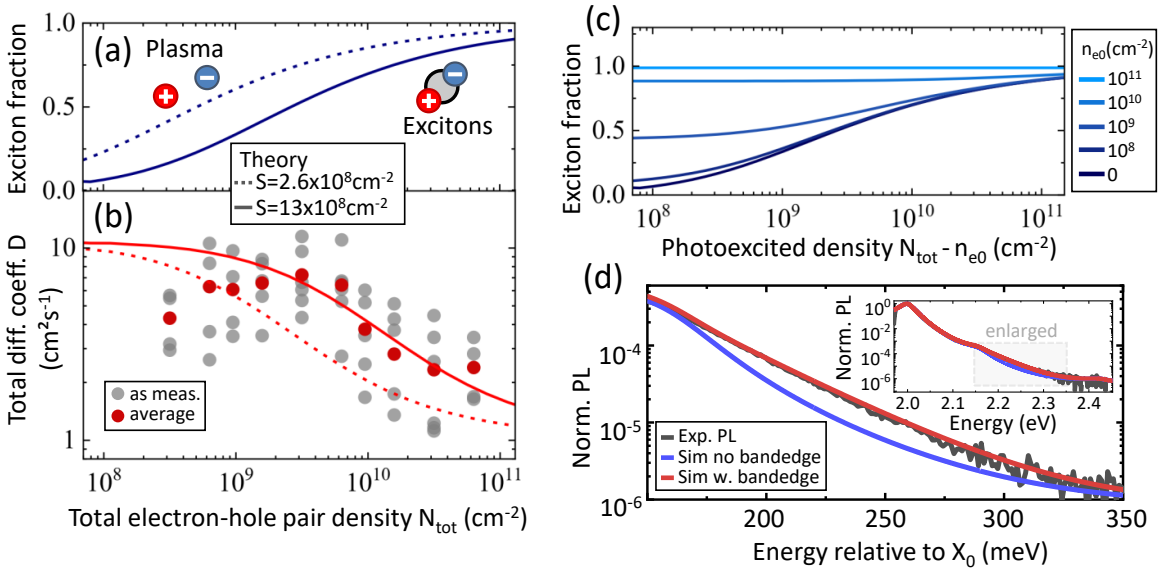

Figure 4.14: (a) Estimated exciton fraction given by the Saha equilibrium within the range of the experimentally accessed electron-hole pair density. The fraction is shown for two realistic Saha parameters S (see text for details). (b) Solid and dotted lines are the corresponding calculated composite diffusion coefficients using the exciton and plasma fractions given in (a). Also included are the measured and averaged values from the time- and spatially resolved photoluminescence measurements of fig. 4.15 (b). (c) Calculated exciton fraction including different levels of electron doping as a function of the photoexcited electron-hole pair density. (d) Long-time photoluminescence measurements in continuous wave excitation. Simulations from a transfer matrix approach fitted to the 1s and 2s resonance are additionally shown, with and without inclusion of a simple bandedge model.

$N_{tot}(\vec{x}, t)$, the diffusion coefficient can be extracted in the familiar way. Fig. 4.14 (b) presents the obtained compound diffusion coefficient with respect to the total electron-hole pair density for the two different Saha parameters. Additionally, the experimental data of fig. 4.12 (b) are included for comparison.

We find that the experimental observations are reasonably described by this model of combined exciton-plasma diffusion. Especially, considering the spread of the measured data, the theory is in good agreement with the observed general trend of the evolution of the diffusion coefficient with respect to the injected electron-hole pair density. In particular, it allows to cover the findings of a high diffusion coefficient in the low density regime, which could previously not be brought into agreement with theoretical predictions of diffusion from purely excitonic states. In conclusion, we therefore find that, given low excitation densities under room temperature conditions, a finite population of free charge carriers in monolayer TMDC could indeed influence the diffusion coefficient measured of optically excited charge carriers.

4.3.1.4 Influence of doping on the Saha equilibrium

Finally, the relevance of intrinsic doping for the above described model of the compound diffusion coefficient is discussed. As introduced in the context of disorder effects in sec. 4.2.4, such doping is commonly found in the investigated structures and may constitute an important factor to consider when evaluation the plasma-exciton equilibrium, since it introduces a finite amount of intrinsic free charge carriers n_{x0}. The doping in the here used samples is of n-type and from the low temperature white light measurements estimated to be in the range of n_{e0} $\approx 10^{10}$-$10^{11}\mathrm{cm}^{-2}$. To account for this, the relation of eq. 2.22 can be readily extended to include the presence of a finite intrinsic amount of free charge carriers [153]. This is done by accordingly changing the two conditions given in eqs. 2.19 and 2.20 to yield the total density of free electrons n_e^{tot} and electron-hole pairs N_{tot} as:

$$n_e^{tot} = n_h^{tot} + n_{e0}, \tag{4.5}$$

and

$$N_{tot} = n_{ex}^{tot} + n_h^{tot}. \tag{4.6}$$

From this follows the exciton fraction in an arbitrarily n-dope system in analogy to sec. 2.4.2:

$$\alpha_{ex} = 1 + \frac{S + n_{e0}}{2N_{tot}} - \sqrt{\left(\frac{S + n_{e0}}{2N_{tot}}\right)^2 + \frac{S}{N_{tot}}}. \tag{4.7}$$

Using this extended relation, the resulting predicted exciton fraction, including intrinsic free charge carrier densities n_{e0} in the range of 10^8-$10^{11}\mathrm{cm}^{-2}$, are presented in fig. 4.14 (c).

Already for doping levels on the order of $10^9\mathrm{cm}^{-2}$, we find that the equilibrium is strongly shifted in the favor of exciton formation, while in the range of the estimated doping densities formation of excitons is expected to completely dominate the electron-hole pair population. This can be intuitively understood in the picture of a photoexcited hole more easily finding an electron to form an exciton, given sufficient free electrons from intrinsic doping. From this can be followed that an increase of one of the species is already sufficient to significantly shift the thermodynamic balance in favor of the formation of bound states. Given these predictions and the measured doping densities, we would therefore expect that excitons in our samples should completely dominate the propagation dynamics over the whole density range. While such doping densities can not be easily argued away, it is also of worth to consider that the doping densities determined from low temperature measurements may not accurately represent the doping scenario present under room temperature. In order to get a better understanding of the influence

of doping on the plasma formation under experimental conditions at room temperature, we performed additional experiments to probe whether emission from such plasma states above the free-particle bandedge could be detected.

For this purpose, photoluminescence measurements under long-time continuous wave exposure for an injected electron-hole pair density on the order of $10^9 \mathrm{cm}^{-2}$ were performed. Two separate spectra were acquired. First, the signal was integrated over for 50 minutes in the relevant energy regime of the expected plasma emission, while the strong A-exciton emission was cut out using a suitable short-pass filter. It was then spectrally stitched together with a second spectrum, measured without filter, to yield a full emission spectrum with a signal-to-noise ratio on the order of 10^6. A spectral close-up of the obtained spectrum is presented in fig. 4.14 (d) in a logarithmic plot and normalized for the maximum intensity. The depicted relative energy range with respect to the 1s resonance is chosen to be in the range of the expected bandedge, while the full spectrum is presented in the inset. Additionally included are the imaginary parts of a model dielectric function for two different simulations of a transfer matrix approach. The simulations are broadened by a Boltzmann distribution for room temperature and fitted to the 1s and 2s resonance of the photoluminescence. We note that here, the imaginary part of a dielectric function, in a very good approximation, should resemble the photoluminescence properties of the underlying material, only neglecting effects from radiative broadening. However, this should be well justified, given the small radiative broadening in contrast to the non-radiative broadening from phonon scattering at room temperature, as can be seen in fig. 4.6. The validity is further confirmed by simulated and fitted spectra of room temperature reflectance measurements on the same sample, yielding essentially equivalent values for the exciton resonance parameters.

The blue curve is the result of a simulation, only including resonances for the 1s and 2s state in the model dielectric function. For energies of about 180 meV above the 1s resonance a clear discrepancy with the measurements is found, significantly underestimating the measured photoluminescence. The dielectric function that underlies the red curve, on the other hand, includes a smoothed imaginary heavy-side function around 180 meV above the 1s resonance. We can view this as a simplified way to account for potential higher excited states and, in particular, free charge carriers above the bandedge. The energy position hereby is in good agreement with predicted values [119] and our estimations of the 1s binding energy in sec. 4.2.4. Here, we find that the experimental data can be well approximated with an appropriately chosen size of the heavy side-function and its broadening, while all other parameters are being kept fixed. Especially the high energy tail resulting from the inclusion of such a bandedge-like function, simply given a Boltzmann distribution, well describes the experimental findings.

From this simple modeling we find confirmation that under experimental conditions at room temperature emission from states above the bandedge is observed, which can be attributed to the presence of plasma. This is further supported given the apparent consistency with a Boltzmann-like fall-off of this emission towards higher energies, that is expected from such free-particle states [255]. However, it shall be clearly stated that these results should not be taken as prove that doping can simply be neglected in the theoretical predictions of the previous section. Yet, these measurements indicate that there are discrepancies between doping levels estimated from low temperature measurements and their actual influence on the exciton-plasma equilibrium under room temperature. Under any circumstances we find that the underlying doping dynamics are rather non-trivial and motivate further investigations. In particular, experiments with well defined doping concentrations under room temperature conditions may provide a platform to more thoroughly investigate such complex charge carrier dynamics.

In conclusion of this segment we can state that, while experimental findings are not yet fully consistent, the presence of a finite amount of free charge carriers at ambient conditions provides a promising hypothesis in understanding observed propagation dynamics of electron-hole pairs. In particular, the density dependent formation of these free charge carriers through entropy ionization can help to explain unexpectedly high diffusion coefficients, which are otherwise not brought into agreement with theoretical calculations. In this context, however, predictions of the influence from estimated intrinsic doping on the exciton-plasma equilibrium still leave us with contradicting results, while first meticulous measurements of photoluminescence emission support the presence of plasma like states at room temperature. All in all this motivates a more detailed investigation of the plasma formation dynamics under ambient conditions with respect to the presence of intrinsic free charge carriers. In this context, the fabrication of more complex structures that allow for a well defined control of doping levels could help unravel the encountered inconsistencies.

4.3.2 Exciton propagation at low temperatures

In the previous section it was shown that, at elevated temperatures, the presence of free charge carriers can potentially have strong influence on the total electron-hole pair propagation. Due to the strong temperature dependence of the exciton-plasma equilibrium this would generally render the temperature dependence of the propagation non-linear. This alone straightforwardly motivates the investigation of exciton diffusion also at lower temperatures. In addition to that, scattering with lattice phonons for decreasing temperature is progressively more suppressed. In a first instance, this intuitively suggests propagation to be more efficient. On the other hand, one finds from

the Einstein relation (eq. 2.16) that the efficiency of diffusion also scales proportionally with temperature from simple relations of the excitons' kinetic energy. These counteracting temperature dependencies, predicted from classical models, further motivate a more detailed investigation.

The approach of tracking the spatial broadening of the photoluminescence intensity, however, turns out to be more challenging at low temperatures. This is due to arising additional emissions from lower energetic states and even more so due to an extremely short photoluminescence lifetime of the bright state under such conditions [86–90]. Therefore, we turn to studying a different TMDC system, namely that of WSe_2. As stated before, it is closely related to the previously investigated WS_2, especially regarding similarities in their band structures. But in contrast to WS_2 we find that here, emission from suitable lower lying states can give access to investigate exciton propagation also at low temperatures. For this purpose, we initially discuss the intricate emission spectra observed in WSe_2 under cryogenic conditions. We then turn to examining long-lived resonances and confirm their origin as being a result of phonon-assisted recombination of neutral dark states. Finally, this allows us to study exciton transport and we present first results for the exciton diffusion efficiency at cryogenic temperatures, including the dependency of propagation dynamics for a series of slightly elevated temperatures.

4.3.2.1 WSe_2 photoluminescence at low temperatures

As stated above, the TMDC monolayers investigated in this experimental section are those of WSe_2 and the reasons for the better suitability of this material system to study low temperature exciton dynamics can be found in time resolved emission spectra. In order to obtain well resolved photoluminescence spectra under cryogenic conditions, high-quality samples with preferably small resonance linewidths are of necessity. Therefore, the monolayers were encapsulated according to the methods introduced in sec. 3.1.2. Taking into account the findings of sec. 4.2, the sample flakes were cooled to liquid helium temperature and mapped by systematic white light reflectance measurements. The spectra were fitted and areas with 1s resonance linewidth as narrow as 4.5 meV, close to theoretically predicted limits of homogeneous broadening (see fig. 4.6), were identified. Furthermore, no significant shifts in the binding energy over 10's of μm^2 were detected, indicating that dielectric disorder was in general sufficiently suppressed. For time- and spectrally resolved photoluminescence measurements such positions on the flakes were deliberately chosen and excited, using the pulsed Ti:Sa laser source. The laser was tuned to the 1s exciton transition energy for resonant excitation in order to minimize effects from non-thermalized, hot excitons. The excitation spot was focused to a FWHM of about 1.5 μm using the 40x magnification microscope objec-

tive with a glass correction ring to account for distortions from the cryostat window. Furthermore, the excitation power was chosen to be in a rather low density regime of roughly 70 nJcm^{-2} per pulse. This corresponds to an injected charge carrier density of about 5.5x10^{10} cm^{-2} assuming 30% overall absorption. This was approximated from an effective resonant monolayer absorption of 50%, estimated from fitted simulations of reflectance measurements, and an overlap of the laser and absorption peak of 60%. We note that such rather low excitation densities allow to largely avoid nonlinear effects, in particular formation of biexcitons [31]. Emitted light was spectrally resolved and projected onto the CCD camera. For time resolved imaging, the streak camera is used instead. The excitation laser and 1s resonance were spectrally cut, using a tunable high-quality long-pass filter. A typical photoluminescence spectrum at 5 K is depicted in fig. 4.15 (a) top (CCD), while the corresponding time resolved spectrum (steak camera) is shown on the bottom.

First of all, it is evident that the emission spectrum is more complex in contrast to room temperature measurement, since resonances from multiple exciton complexes and states now contribute to the detected signal. This is mainly due to energetically lower laying states becoming heavily populated at cryogenic temperature, following thermodynamical arguments along the lines of sec. 2.4.2. The resonance labeled as X_0 corresponds to the 1s ground state exciton transition. Note that compared to WS_2 the resonance energies are generally lower in WSe_2 due to the smaller bandgap of this material. The two peaks, both labeled by X^-, roughly 28 meV and 35 meV below the ground state resonance, are attributed to the well-known trion doublet [105]. X^D denotes the long-lived, spin-forbidden, intravalley exciton with a separation from the 1s resonance of about 42 meV. Due to the large numerical aperture of our used microscope lens, we are sensitive to small parts of in-plane emission, allowing to observe this resonance in photoluminescence experiments [63, 100]. Note that this in-plane emission additionally allows to selectively crop signal from this resonance in the fourier-plane, since it will be focused on the outer parts of the same, giving further confirmation of its assignment. The resonance marked XX^-, about 51 meV below the ground state, has been attributed to a negatively charged biexcitonic complex, using density dependent measurements [31]. Lastly, we find two long-lived resonances labeled P_1 and P_2 with observed transition energies 58 meV and 64 meV lower than the ground state respectively. P_2 has been attributed to a phonon-assisted emission from the spin-forbidden dark X^D under simultaneous emission of a chiral E$''$ phonon [256, 257]. The attribution of the P_1 resonances, on the other hand, remains more challenging. In the following section we argue that this resonance can also be attributed to a phonon-assisted emission, however, in contrary to the P_2 resonance, it results from a momentum-forbidden intervalley exciton.

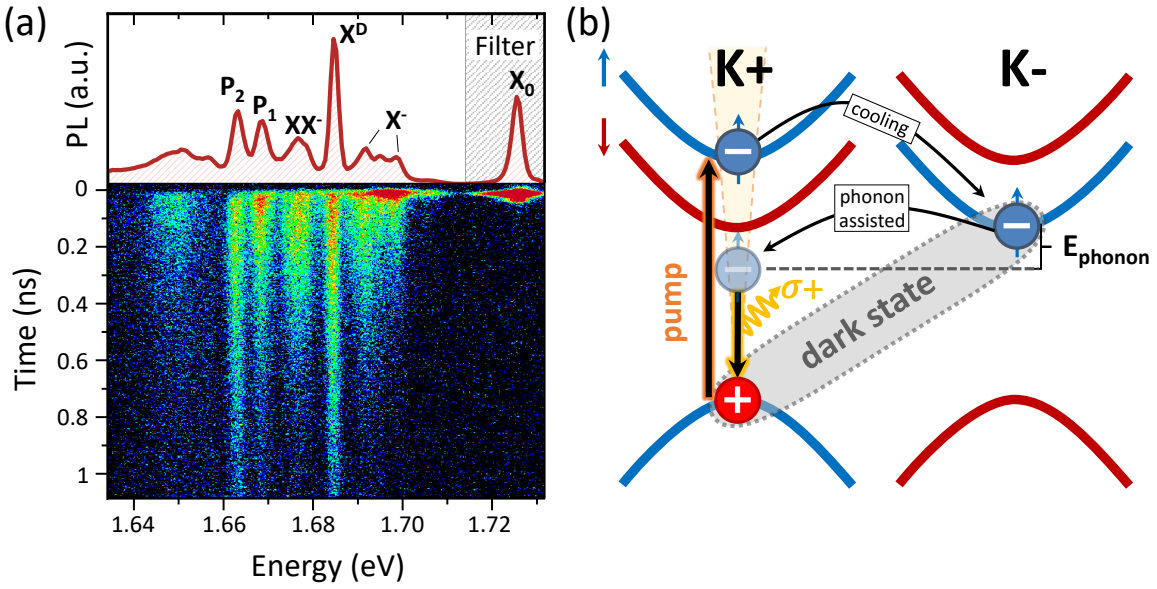

Figure 4.15: (a) Top: Photoluminescence spectrum of encapsulated WSe_2 monolayer at 5 K. Different excitonic resonances are labeled and discussed in the main text. Bottom: Corresponding time- and spectrally resolved emission spectrum using a streak camera detector coupled to the spectrometer. (b) Schematic illustration of the proposed process for the phonon-assisted emission from momentum-forbidden K+−K- states, resulting in the observed P_1 resonance.

First, however, we would like to point out the challenges in investigating exciton diffusion from time- and spatially resolved photoluminescence intensity, considering such a non-trivial spectral emission profile. In order to get a conclusive picture of exciton diffusion, it is necessary to spectrally well separate the investigated resonance. This is important in order to avoid distortions from influences of other excitonic resonances (such as trions or biexcitons), which may have deviating propagation properties. As can be seen here, the emission from the X_0 ground state would in general be spectrally well separated from other resonances to allow for the studying of propagation dynamics. However, as also confirmed by off-resonant excitation experiments, this resonance is very short lived, with our highest time resolution of about 5 ps not being able to sufficiently resolve emission from this resonance. Therefore a different approach has to be used. In principle, the resonance of the spin-forbidden dark state (X^D) provides access to a neutral exciton state, however, while this resonance is sufficiently long-lived, spectrally isolating this resonance remains challenging. Moreover, we find that under experimental conditions, it is hard to keep the measurements sufficiently stable over the required time, given the low intensity of emission from this state alone. This leaves the two resonances P_1 and P_2, attributed to phonon-assisted emission from dark exciton states. These yield sufficient intensity, while at the same time being long-lived and easily spectrally

separable. Furthermore, such phonon side bands would provide a direct access to the dynamics of their underlying parent-state. For this purpose, the assignment as phonon-assisted emissions from higher lying dark states is further investigated and, in particular, proof for the P_1 resonance also originating from such a process is given.

4.3.2.2 Phonon-assisted emission from dark exciton states

We now turn to the assignment of the P_1 resonance as being a phonon-assisted emission from a momentum-forbidden intervalley exciton. The proposed process for the emergence of the P_1 resonance is schematically depicted in the frame of a single-particle band structure in fig. 4.15 (b). Shown is the direct bandgap for both energetically degenerate K±−points in the Brillouin zone and for simplicity only the relevant higher lying spin-split valence bands are included. The different spins, resulting from spin-valley locking (sec. 2.1.2), are denoted by colors. Here, we consider excitation from incident $\sigma+$ polarized light that drives a transition between the valence and higher spin-split conduction band in the K+ valley, since selection rules in WSe_2 are identical to those of WS_2, introduced in fig. 2.3. The electron can then, via coupling (emission) to a suitable zone edge phonon [258] and under conservation of spin, scatter into the lower spin-split conduction band at K-, denoted as cooling. The reverse process, however, is strongly suppressed due to a lack of suitable phonons for absorption, given the phonon population at cryogenic temperatures. Note that even for resonant excitation, where excitons are expected to recombine fast with short radiative lifetimes on the order of <1 ps [86–90], the coupling to phonons is expected to be similarly efficient as seen in fig. 4.6, rendering it a competitive process. The result is a well populated momentum-forbidden dark exciton state, that, due to the absence of a direct radiative decay channel, is expected to be long-lived. However, involving the same phonon as for the cooling process, the electron can scatter back into a virtual state inside the light-cone at K+. Since this scattering event is again spin-conserving, a transition of this virtual state is allowed by selection rules. The momentum-forbidden, dark intervalley exciton could thus recombine radiatively under emission of a suitable phonon. Finally, we remark that while in this proposed decay scheme we have only considered scattering between K+ and K- valleys, an analogous process could in principle also be imagined, involving the Λ valley in conduction band [258]. As stated previously and depicted in fig. 4.13, a momentum-dark K−Λ exciton could have similar energies as the here considered momentum-forbidden K+−K- state [93] and thus equivalent arguments as in the above described scenario would apply.

In order to experimentally confirm this model, we make use of the spin-conserving properties of the proposed exciton phonon scattering. Due to this, the emitted light from such a phonon-assisted recombination process is expected to have the same polarization

as the initially excited state. In other words, upon resonant circular excitation the emission from this state is expected to show long-lived co-polarization. To investigate this we perform measurements with resonant polarized ($\sigma+$) excitation, while separately filtering for both $\sigma\pm$ polarizations in detection. These measurements are performed in the same manner as those described in the previous section. However, the spot size is enlarged to a FWHM of about 4 μm, while at the same time increasing the laser power to yield approximately the same energy density per pulse. This is done in order to compensate for the signal loss due to the additional filters in the detection path. The resulting spectra are depicted in fig. 4.16.

First, (a) presents a spectral closeup of the P_2 and P_1 resonances under resonant $\sigma+$ excitation, resolved for $\sigma\pm$ polarization in steady-state detection. The measured data is shown as filled circles and a double-peak fit is included in solid lining with the shaded areas indicating the intensity of the individual resonances, as obtained from the fit. For $\sigma+$ polarized excitation this allows to calculate the polarization degree P of the resonances according to:

$$P = \frac{I_{\sigma+} - I_{\sigma-}}{I_{\sigma+} + I_{\sigma-}}, \tag{4.8}$$

where I is the emission intensity for the corresponding polarization in detection. It is found that the emission of the P_1 resonance is strongly co-polarized, with a polarization degree of roughly 80 %. This is in good agreement with the predicted process of this resonance originating from a momentum-forbidden exciton state via spin-conserving phonon-scattering. Note that the P_2 resonance, on the other hand, shows only marginal polarization, additionally underlining its different origin and in good agreement with previous observations [256, 257].

To further investigate this attribution, the full polarization resolved spectra are shown in the top panel of fig. 4.16 (b), while the corresponding temporal evolution of the polarization degree is presented in the bottom panel. The high degree of polarization of the P_1 resonances is confirmed and above that shows to be remarkably stable and long-lived. An extracted polarization decay time on the order of >1 ns gives additional credibility to the proposed model. To give further confirmation of this, the energy range for the spectrum in (b) is shifted to lower energies in comparison to fig. 4.15 (a). This allows to observe two additional low energy resonances with strong co-polarization, resembling that of P_1. We attribute these resonances to phonon progression modes, that is higher order phonon-assisted emissions, considering their equidistant energetic separation from the P_1 emission and the similarities in their general decay and polarization dynamics. These peaks are therefore labeled P_1' and P_1''.

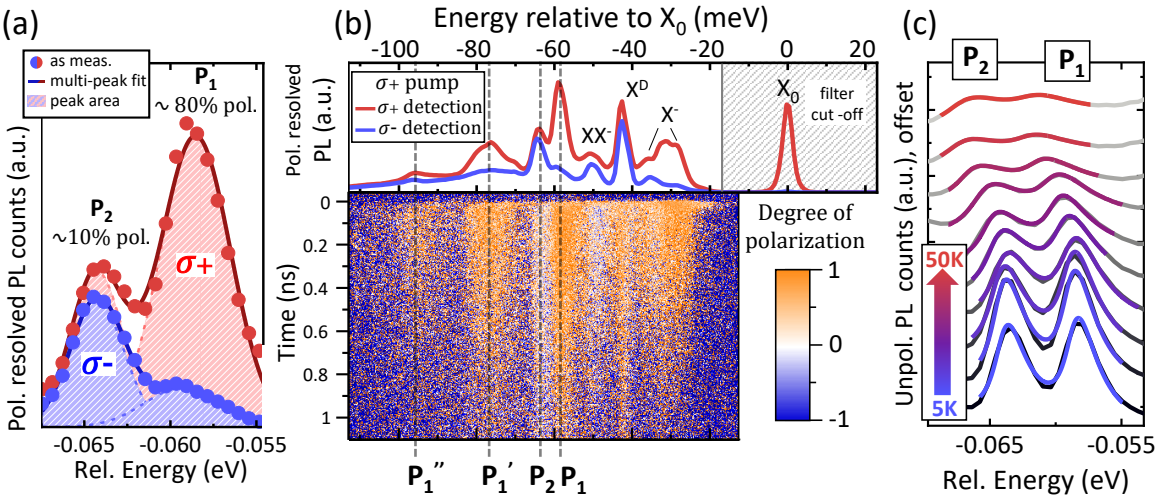

Figure 4.16: (a) Polarization resolved emission from P_2 and P_1 resonances (dots) under $\sigma+$ polarized resonant excitation, including a double-peak fit (solid lines). The shaded area is the corresponding peak area, proportional to the emission intensity and used to calculate the degree of polarization from eq. 4.8. (b) Top panel: Polarization resolved photoluminescence measurement of encapsulated WSe_2 at 5K upon resonant circularly polarized $\sigma+$ excitation. Laser and neutral exciton resonance are cut using a tunable high-quality edge pass filter. Bottom panel: Corresponding time- and spectrally resolved degree of polarization. Observed energy range includes phonon replicas P_1' and P_1'' on the low energy side of the P_1 resonance. (c) Spectral close-up of the P_2 and P_1 resonances for different temperatures and unpolarized detection (gray). The spectra are vertically offset for clarity. Double-peak fits with an asymmetrically broadened high energy flank from a Boltzmann distribution are included in color.

Furthermore, we investigate the temperature dependence of the P_1 and P_2 resonances, depicted in fig. 4.16 (c) for a temperature range up to 50 K and vertically offset for clarity. Here, the two observed resonances (gray) are fitted with a double-peak function that additionally has to be broadened with an exponential, Boltzmann-like distribution on the high energy flank to obtain a satisfactory approximation of the emission shape (color). Such a temperature induced asymmetric broadening is a typical characteristic of phonon sideband emission [259, 260] and can be clearly observed, particularly in the mediocre temperature regime, where overall broadening from phonon scattering is still weak. This is due to zone edge phonons generally being able to compensate for arbitrary exciton momenta while at the same time their energy, defined by the phonon dispersion relation, varies only slightly [261–264]. This results in phonon sideband emissions basically mirroring the Boltzmann-like distribution of exciton states at elevated temperatures, leading to the observed asymmetric broadening. Excitons that recombine without phonon assistance, on the other hand, are strictly bound to emit within the lightcone as discussed in sec. 2.1.3.

Finally, our findings are in good agreement with similar, very recent studies on the phonon-assisted emission in WSe_2 monolayers that appeared during the writing of this work [265]. In this study the authors additionally include magnetic field dependent measurements, which allow them to exclude the involvement of momentum-forbidden K-Λ states due to magnetic field induced shifts being sensitive to the valley magnetic moment, which is different for K and Λ conduction bands. Moreover, the authors give evidence of emission from its underlying parent-state that they attribute to be the momentum-forbidden intervalley K+−K- state. Such nominally forbidden optical transitions can be achieved via localization of excitons at lattice defects, where the need to conserve lattice momentum is lifted [266] and thus selection rules do not have to be strictly fulfilled. According to this work, the observed resonance is expected to lie between the two trion resonances. Indeed, our spectra also show an additional, strongly co-polarized resonance in this energy range. Interestingly, this resonance is suppressed for higher excitation densities (not shown), which is typical for defect mediated emission, since the finite defect density is quickly saturated. While this resonance in our spectra would be in good agreement with the findings of ref. [265], a quantitative analysis in our measurements remains challenging due to its significant spectral overlap with trion resonances from intrinsic doping. Additionally, we note that observed temperature dependencies in our experiments are not yet fully compatible with such an interpretation, as both P_1 and P_2 show similar intensity dependence with respect to temperature, depicted in fig. 4.16 (c). In a scenario where these two resonances result from exciton states that are separated by roughly 10 meV, this is generally not expected. From simple thermodynamical arguments, a Boltzmann-like distribution would predict the energetically lower lying state to be depopulated faster. This, in turn, should lead to a faster decrease in intensity in contrast to the higher lying state, given the phonon scattering rates are not strongly affected. Therefore, while the interpretation of this resonance being the origin of the P_1 resonance generally supports our model and is additionally in good agreement with parts of our observations, further studies are motivated to clear up remaining inconsistencies with temperature dependent observations.

In summery of these observations, we find the experimental results in strong support of the proposed scattering model, with all findings pointing towards its applicability, although the exact energetic position of the parent-state remains an item for further studies. From this we find confirmation of the assignment of the P_1 resonance as a phonon-assisted emission, resulting from the scattering of a momentum-forbidden intervalley state into a transition-allowed intravalley state. The long-lived emission from both P_1 and P_2 phonon sidebands as well as the P_1' and P_1'' phonon progression modes thus give a handle in accessing the time-dependent spatial dynamics of neutral excitons at cryogenic temperatures.

4.3.2.3 Neutral exciton propagation at low temperatures

For the study of the spatio-temporal dynamics from these phonon sideband emissions, linear excitation and non-polarized detection are used in order to maximize signal. This allows to again inject comparably low exciton densities on the order of $5\text{x}10^{10}\,\text{cm}^{-2}$ while focusing the laser to $1.5\,\mu$m FWHM to achieve maximum spatial resolution for the diffusion measurements. Such low densities are necessary to keep contributions of the energetically close biexciton state small, as the formation of such states is known to be density activated [31]. In turn, the suppression of biexciton formation can then serve as an indication that the investigated density is below regimes where non-linear effects, in particular Auger recombination, are expected to influence exciton dynamics, which is in good agreement with observations under room temperature conditions [40, 153]. The photoluminescence signal is then initially spectrally cut to yield a spectrum where only the above discussed emissions from phonon-assisted neutral dark states contribute to the detected signal. This is depicted in fig. 4.17 (a), where a representative 5 K spectrum is shown by dotted lines. The colored spectrum is obtained by spectral cropping. For this purpose, an ultra-sharp tunable long-pass filter is used in detection to finely adjust the 'cut-on' energy. The obtained tailored spectrum then allows to track the dynamics of only the phonon sidebands' underlying parent-states.

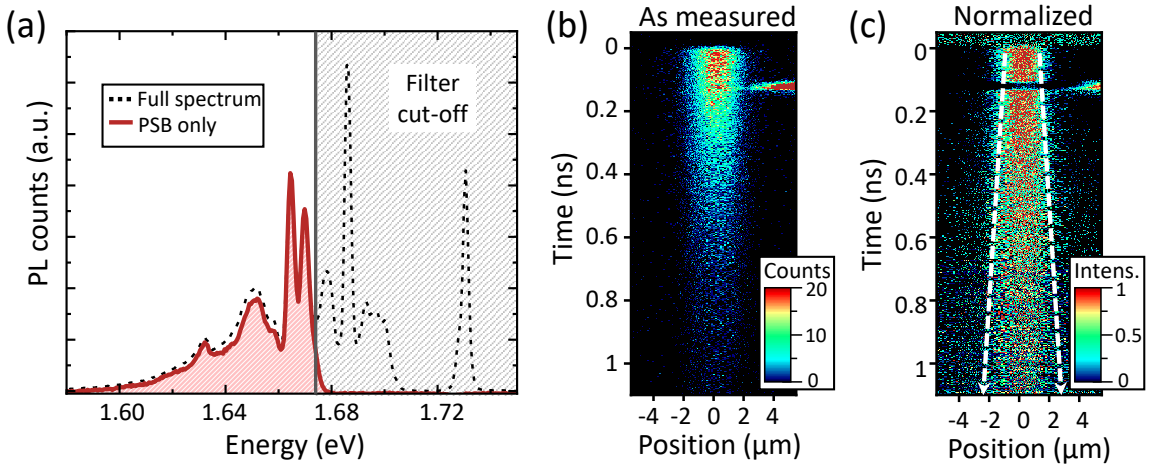

Figure 4.17: (a) 5 K photoluminescence spectrum of a hBN-encapsulated WSe_2 monolayer at comparably low excitation density, largely suppressing biexciton formation (dotted). The emission is spectrally cut using a tunable high-quality short-pass filter to selectively crop emission from only phonon sidebands (colored spectrum). (b) As-measured streak camera image of time- and spatially resolved photoluminescence from WSe_2 phonon sidebands at 5 K. The bright spot on the right-hand side around 100 ps time delay is a reflex of the laser. (c) Corresponding normalized streak camera image. Dotted lines indicate the spatial broadening with time due to propagation of excitons.

Obtained time- and spatially resolved streak camera images from this cropped spectrum are presented in fig. 4.17 (b). The short and strong signal on the right-hand side of the main emission at roughly 100 ps time delay is from a reflex of the pump laser. This is due to the tunable filter operating close to its maximum spectral range, where small parts of stray light of higher energy emission can get scattered back into the detection path. However, due to its spatial separation from the main signal, it can be easily cut out in the data evaluation process. Fig. 4.17 (c) shows the corresponding normalized spectrum. Here, already the spatial broadening of the signal from diffusion can be identified, indicated by the dotted lines.

The streak camera images are processes as described in sec. 3.3.2. Additional to the experiments at 5 K, further measurements in a temperature range up to 35 K have been performed. We note that propagation dynamics from phonon side band emission at temperatures beyond that range are more challenging to access due to temperature induced resonance broadening from phonon scattering. This leads to the individual resonances getting progressively more difficult to separate while at the same time the signal from sidebands is decreasing due to their parent-states becoming less populated with increasing temperature. The obtained exciton dynamics for the accessible low temperature range are presented in fig. 4.18. In (a), the general decay dynamics at different temperatures are presented in form of transients extracted from the individual streak camera images. Included as dark solid lines are purely mono-exponential fits to the data, while the corresponding lifetimes are depicted in (d). It is found that for all temperatures the observed population decay is well described by such a model, further supporting that non-linear effects, generally introducing non-mono-exponential dynamics [40], are of subordinate importance for the injected exciton density. Additionally, a decrease in the lifetime with temperature is observed, that is expected, since increasing phonon scattering efficiency leads to a depopulation of these low energy states. The extracted spatial broadening for the four different temperatures is shown in (b) in the form of the relative squared Gauss width $\Delta w^2(t)$ as a function of time. Additionally included are the purely linear fits that allow to extract the respective diffusion coefficients. Here, already a trend of decreasing incline for slightly elevated temperatures can be identified. The corresponding diffusion coefficients depicted in (c) confirm this trend, with these measurements yielding values of roughly $5.5\,\mathrm{cm^2 s^{-1}}$ at the lowest accessible temperature of 5 K, decreasing non-linearly to values around $2.3\,\mathrm{cm^2 s^{-1}}$ at 35 K. While the temperature dependence of the diffusion itself is intriguing, we first turn to analyzing the generally efficient exciton propagation at the lowest studied temperature of 5 K, considering a basic diffusion model as introduced in sec. 2.4.1.

In this context, we yet again emphasize that phonon scattering processes at cryogenic temperatures are strongly suppressed due to the reduced phonon population, leading

to an increase of the exciton scattering time. From that rises the important question of the validity of a diffusion like description of exciton propagation at low temperatures. This is of particular interest in the context of propagation becoming progressively more ballistic when scattering times approach magnitudes comparable to the exciton lifetime as discussed in sec. 2.4.1. We thus estimate the scattering time from the Einstein relation given in eq. 2.16 for a reasonable total exciton mass in monolayer WSe_2 around $0.8\,m_0$ [56, 79–81] and the measured diffusion coefficient at 5 K. The obtained value for the exciton scattering time τ_s is on the order of 6 ± 1 ps, considering the errorbars in the measurements. In comparison to that, the dark exciton states exhibit remarkably long lifetimes of roughly 400 ps at this temperature, as depicted in fig. 4.18 (d). With the estimated scattering times being significantly lower than the observed exciton lifetimes, we thus find that a diffusive description of propagation is well justified. Furthermore, we remark that also an evaluation of eq. 2.15 confirms the applicability of such a description with the de Broglie wavelength still being smaller than the mean free path. Finally, we note that the assumption of a purely exciton dominated electron-hole population

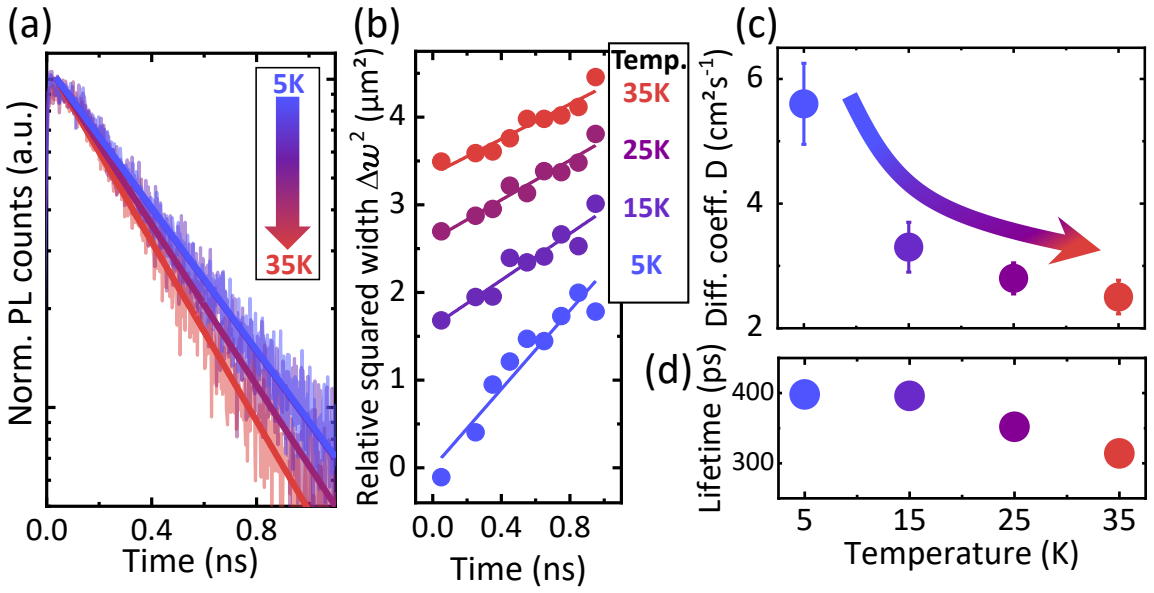

Figure 4.18: (a) Transients of the time resolved photoluminescence for four different temperatures of 5 K, 15 K, 25 K and 35 K, indicated by color. Mono-exponential fits are included in solid lines that allow to extract the lifetimes depicted in (d). (b) Relative squared Gauss width from time- and spatially resolved photoluminescence measurements of the phonon sideband emission in hBN-encapsulated WSe_2 as a function of time. Data for different temperatures in the range of 5-35 K are vertically offset for clarity. Linear fits for the extraction of the diffusion coefficients are included as solid lines. (c) Corresponding diffusion coefficients as a function of temperature. (d) Photoluminescence decay time extracted from the transients of the time resolved data.

at cryogenic temperatures is well validated, since the entropy contributions favoring formation of free particles become negligibly small. The presence of plasma and its influence on the measured diffusion coefficient can therefore be disregarded.

It is then found from eq. 2.13 that this diffusive propagation at 5 K constitutes noticeably efficient exciton transport over distances on the order of roughly 1 μm. This shows that even though bright excitons decay rapidly at low temperatures, dark excitons can still propagate significantly further than electron-hole pairs under ambient conditions, which exhibit a diffusion length on the order of roughly 300 nm, even for the highest diffusion values discussed in sec. 4.3.1. Moreover, it can be shown that the here measured diffusion efficiency suggests that localization due to residual disorder or trapping at lattice defects - against intuition - only play a minor role for the exciton propagation at low temperature. If we assume that all scattering events lead to a purely homogeneous broadening of the signal, this allows to estimate a maximum value for the homogeneous broadening from eq. 2.5, which contributes to the total observed linewidth. We note that given the long lifetimes of the dark states and the fact that these states are the energetically lowest states, contributions to the homogeneous broadening from scattering into other states can be largely excluded. For the estimated scattering times from above the evaluation of eq. 2.5 yields a maximum homogeneous broadening of around 0.1 meV. At cryogenic temperatures only linear acoustic phonons should be populated and our work on the homogeneous broadening in WSe_2, depicted in fig. 4.6, predicts a broadening from phonon scattering (absorption) to be on the order of 20-25 μeVK^{-1} [92]. Given the temperature of 5 K in our experiments this would constitute a homogeneous broadening from phonon scattering alone, that is on the order of the maximum predicted value derived from the scattering during diffusive propagation. As a consequence we can infer that scattering events of excitons occurring during diffusive propagation, even at low temperature, are largely dominated by the scattering with lattice phonons. On the other hand, this implies that other effects, such as residual disorder after encapsulation or localization at defects hardly influence the exciton propagation at cryogenic temperatures.

Turning back to the temperature dependence of the propagation, we find a nonlinear decrease of diffusion efficiency with increasing temperature. Following the same argumentation as before, such behavior is not easily expected. As already discussed above, the phonon population and consequently also the scattering time should increase linearly in the investigated temperature regime. Regarding the expected diffusion coefficient, we find from the Einstein relation that this linear temperature dependency cancels out, assuming also the excitons kinetic energy scales linearly with the temperature. This is reasonable since excitons are expected to quickly reach thermal equilibrium with the lattice due to fast cooling rates compared to their lifetime [251]. Thus, in the

given temperature range, a simple model would predict the diffusion to be constant. Experimental findings, on the other hand suggest, a more complex scenario and understanding such non-trivial behavior calls for a more thorough investigation of the underlying physics. In principle, temperature activated interactions with or trapping of excitons at defects could lead to a reduction of the propagation efficiency. Such trapping, however, is generally reflected in the observed lifetime dynamics deviation from a strictly mono-exponential decay, which is not observed. A more promising model is given by a recently proposed mechanism of quantum interference effects in excitonic systems, affecting transport properties at low temperature [267]. Such a model would indeed be in agreement with the observed trend of a decrease of the diffusion efficiency, particularly in the range of the investigated temperature. This motivates a more detailed and thorough investigation of this temperature dependent non-linearity in the diffusion coefficient, to find whether these observations can be brought into agreement with such theoretical models.

In conclusion of this section we note that the phonon mediated emission from dark states in WSe_2 allows to study the diffusion of excitons in a monolayer TMDC system also at cryogenic temperatures. From first studies of this, we find that exciton propagation at such temperatures can be remarkably efficient. Moreover, such efficient diffusion suggest that influences of defects and other inhomogeneities only have minor effects on the propagation dynamics. This intriguing finding contrasts intuitive expectations of trapping centers generally playing a more important role at low temperatures. Finally, the observations of a decrease in diffusion efficiency for only slightly elevated temperatures introduce further unexpected non-linearities and call for a more detailed investigation of these phenomena. This is in particular motivated by recent theoretical predictions of quantum interference effects that are expected to influence exciton transport at low temperatures in a similar fashion and could thus help to understand the experimental observations [267].

4.4 Exciton transport in 2D perovskite systems

In the last segment of the experimental work we investigate a different system of two-dimensional semiconductors, that of layered hybrid halide perovskites in their monolayer (N=1) configuration. As stated in sec. 2.5, these systems show similar efficient exciton formation as TMDC monolayers, while having a fundamentally different structure, founded in their hybrid organic-inorganic nature. While this has made these materials particularly interesting in terms of potential applications, it has sprung wide interest in the scientific community in recent years, as well. However, exciton dynamics, in particular transport phenomena, remain hardly explored. To the author's best knowledge only two studies on exciton propagation in these systems, which appeared during the writing of this work, are available at present [145, 268].

Here we show that methods, initially developed for monolayer TMDC systems, are also applicable to these hybrid organic-inorganic systems and, moreover, allow the study of fundamental charge carrier dynamics that were previously hard to access. More importantly, however, we show that efficient exciton transport under ambient conditions is not limited to TMDC systems. This part of the work can thus be understood as giving a first proof of principle that concepts found in TMDC monolayer systems can have important relevance for other, similar systems. At the same time it shall also serve as a motivation for a more in-depth investigation of exciton transport dynamics beyond the field of TMDC monolayers, with layered halide perovskites introducing novel ways of influencing and tuning electro-optical properties.

In this context, we first focus on the advantages of using the method of encapsulating samples in high-quality boron nitride, as a way to preserve optical properties of volatile perovskite systems and thus facilitating studies under ambient conditions. This then allows to conduct similar transport experiments as for the TMDC monolayers, discussed in the previous sections, and obtain first results on the exciton propagation dynamics in ultra-thin perovskite systems. As the halide perovskite system of choice we use the widespread prototypical compound of butyl-ammonium-lead-iodine $(C_4H_9\text{-}NH_3)_2PbI_4$ (BAPbI) in its monolayer N=1 form, synthesized by colleagues from the Weizmann Institute (Ack. 9).

4.4.1 Stability of perovskites

The low stability of halide perovskites under ambient conditions, leading to rapid degradation and the subsequent loss of optical properties, is a well known issue of this material class. In particular, the exposure to oxygen and moisture constitutes one of the major challenges for both experimental accessibility of properties and potential applications [157, 190–192]. Additionally, considering that the degradation is strongly enhanced un-

der focused light exposure [217, 269], this volatility stands as one of the main obstacles in studying exciton dynamics via optical spectroscopy, especially given the rather long exposure times necessary in the here performed experiments. However, recent studies show, that encapsulation in high-quality hexagonal boron nitride can help overcome problems from oxygen- and moisture-induced degradation effects [167, 168, 171]. The layers of hBN are able to function as an efficient seal, conserving sample properties and additionally heavily suppressing oxygen diffusion through the subjacent substrate, as found in the commonly used SiO_2/Si [172].

To characterize the hBN-encapsulation with respect to its capability of preserving optical properties, we have performed reflectance measurements under focused white light exposure for both a bare and an encapsulated perovskite sample. The white light spot was focused to a FWHM of roughly 1 μm and spectra were acquired in 0.4 s intervals over a time period of 2 minutes, using the spectrometer and CCD camera for detection. For the bare sample a freshly cleaved macroscopic BAPbI crystal was transferred onto a SiO_2/Si substrate, depicted in fig. 4.19 (a), outlined in white. The crystal was chosen to be sufficiently thick (on the order of 100's of μm) to suppress interference effects. At the same time, this allows to probe to which extent the outer layers of a thick crystal can function as self-passivating layers for protecting optical properties of deeper lying layers [145]. Fig. 4.19 (b) presents selected reflectance contrast spectra over the measured period of 2 minutes, vertically offset for clarity. The rapid decay of an initial excitonic resonance around 2.4 eV [189] is observed, which is attributed to degradation of the material. We additionally note that the here used white light intensity is generally much less intense than any exposure from the pulsed Ti:Sa laser source, which is needed to obtain sufficient signal to resolve exciton dynamics. Thus, finding a complete vanishing of the exciton resonance after only 2 minutes of weak exposure conveys that the self passivation from outer layers is not sufficient to preserve optical properties. In particular, given the comparably long integration times of 10-20 minutes necessary in our experimental setup, this puts paid to any reasonable measurements of time resolved exciton dynamics in such pristine samples.

Analogous measurements were performed on an encapsulated BAPbI flake under identical experimental conditions. The sample was produced as described in sec. 3.1.3 and a micrograph of it is shown in fig. 4.19 (c). Outlined in white is the perovskite flake, while the teal and blue parts are the top and bottom hBN sheets respectively, entirely covering the flake and sealing it from atmospheric influences. Selected reflectance contrast spectra taken over the duration of 2 minutes with identical parameters as mentioned above are presented in fig. 4.19 (d). Here it is found that the spectrum does not change over the entire measured time window, with the strong excitonic resonance around 2.4 eV readily observable. We note that also for longer white light exposure,

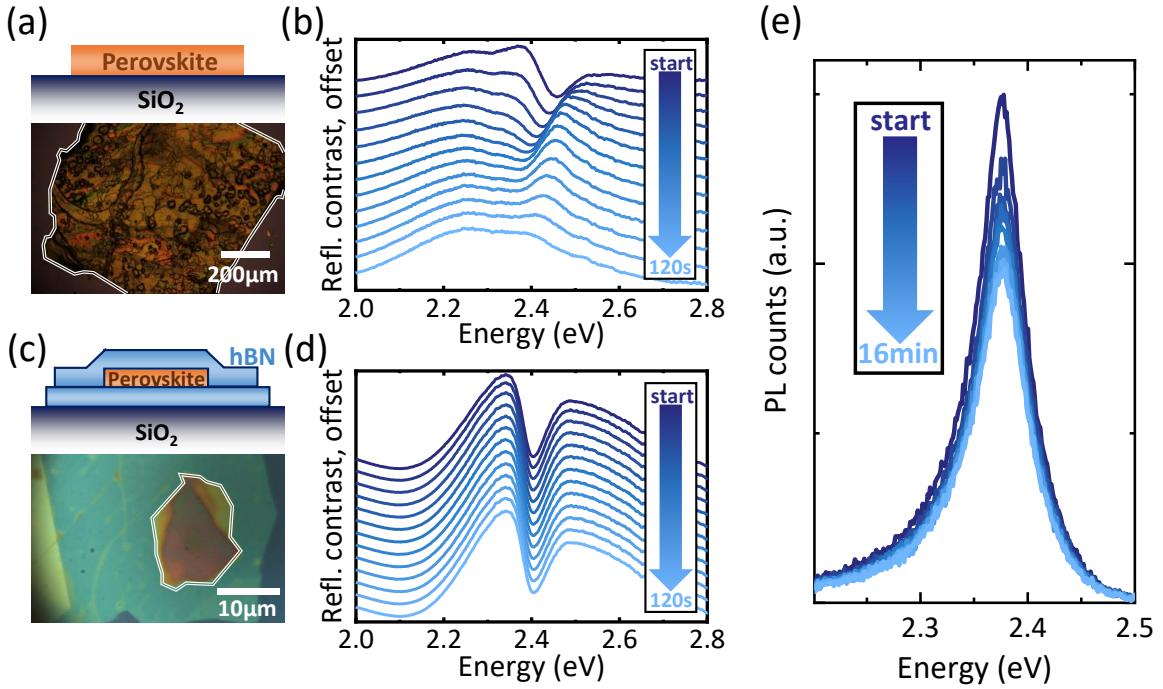

Figure 4.19: (a) Micrograph of a macroscopically thick bare BAPbI (N=1) crystal (outlined in white) on a SiO_2/Si substrate. (b) Corresponding decay of the optical response under white light exposure, measured in reflectance configuration on the freshly cleaved flake over a period of 120 s. (c) Thin BAPbI crystal of the same mother crystal as (a), encapsulated in high-quality hexagonal boron nitride. The illustrated sample structure is shown on top. (d) Corresponding response to white light exposure over a period of 120 s, analogous to (b). (e) Stability of the photoluminescence response of the encapsulated sample over the typical exposure time in transport experiments. The spectra correspond to the highest excitation densities used in sec. 4.4.3.

on the order of many minutes (not shown) no change in the optical properties was found. From this we conclude that hBN encapsulation can indeed drastically improve the optical stability of the samples under ambient conditions.

To also confirm sufficient optical stability under experimental conditions used in transport measurements, additional photoluminescence measurements under pulsed excitation were performed. The Ti:Sa laser source was tuned to 2.817 eV off resonant excitation and focused to a FWHM spot size of 0.6 μm. Emission spectra were recorded on the CCD camera in 1 s intervals over a period of 16 minutes, in accordance with the typical integration time used in transport experiments. The resulting spectra are shown in fig. 4.19 (e). Under such exposure conditions a light induced decrease of the photoluminescence intensity, related to degradation effects, can still be observed. However, no change in the emission energy or the linewidth, that would be indicative of an induced phase transition, is found [187–189]. Given the decrease in emission intensity of roughly 30 % over the whole measured time window, we define the here used exci-

tation density of 4.4 nJcm^{-2} as an upper excitation limit, where effects of degradation are still low enough to yield sufficient emission signal over the whole integration time. Additionally, we note that effects of degradation on such long time scales should not have significant influence on dynamics observed on the sub-nanosecond scale. Resulting from these initial material characterizations, we convey that the encapsulation of layered halide perovskites provides a way to sufficiently preserve their optical properties under ambient conditions. This allows to conduct rather long-time exposure measurements, necessary to investigate exciton transport phenomena.

4.4.2 Exciton dynamics in monolayer perovskites

We now turn to the investigation of time resolved exciton dynamics. For this purpose, encapsulated samples are excited using the same experimental settings as introduced for the photoluminescence measurements of the previous section, while the excitation density is varied in a range between 0.44 to 4.4 nJcm^{-2}. In order to yet keep effects of remaining light induced sample degradation to a minimum, each individual measurement was performed on a new, pristine sample position and two different perovskite flakes were investigated. The emitted photoluminescence was directed onto the streak camera in spatial focus and resolved in time. Furthermore, each measurement is subdivided into five single frames that are subsequently taken over the whole exposure time. This allows to further exclude effects of degradation by comparing the dynamics of each individual frame before being averaged over to yield a single frame with sufficient signal-to-noise ratio to analyze propagation dynamics. A representative streak camera image of such a measurement is presented in fig. 4.20 (a). The corresponding normalized image is shown in (b) and the spatial broadening of the signal with time is indicated by dotted lines. Here, we find that the overall observed dynamics are reminiscent of those of TMDC monolayers. The signal decay is dominated by the finite lifetime of excitons, while the normalized image allows to identify a spatial signal broadening with time, indicative of efficient propagation.

First, we shift our attention to the general dynamics of the photoluminescence decay. Fig. 4.20 (c) presents the transients for one representative set of different excitation densities, extracted from the time- and spatially resolved measurements. Additionally included is a mono-exponential fit over the first 100 ps that allows to estimate an average exciton lifetime. We note that the decay in general is not purely mono-exponential, which is commonly attributed to trapping at defect states [270, 271]. However, for the here studied dynamics an estimated average decay time from the mono-exponential fit shall be sufficient. More importantly we point out that there is no observed density dependence of the decay dynamics, indicating that density driven phenomena,

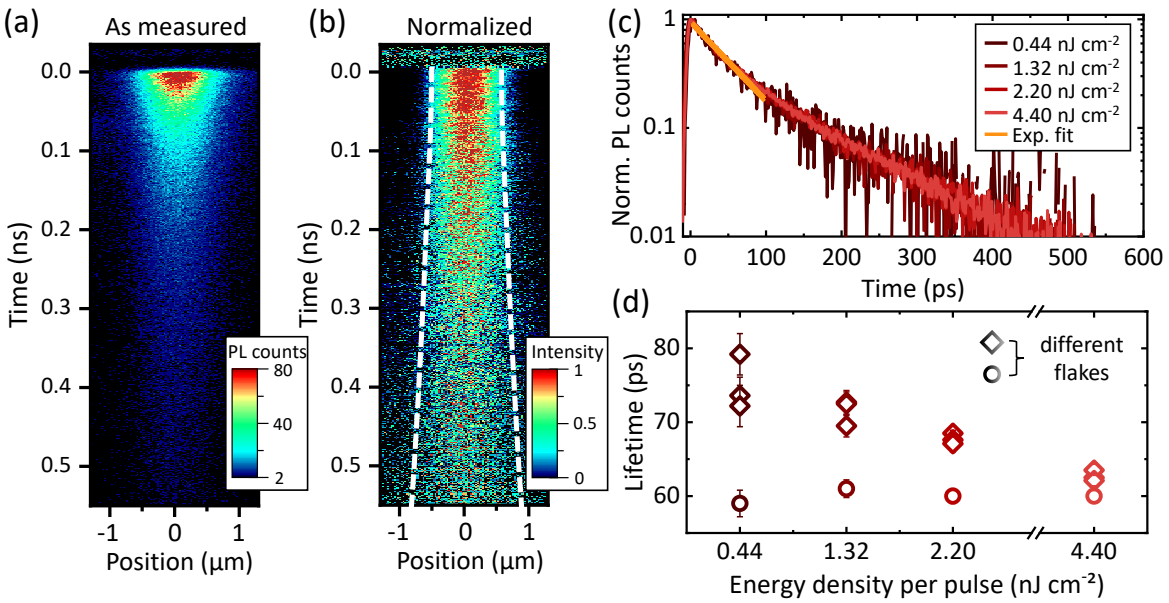

Figure 4.20: (a) As-measured streak camera image of the time- and spatially resolved photoluminescence response for a representative encapsulated perovskite sample. (b) Corresponding normalized streak image. The spatial signal broadening with time due to exciton propagation is indicated by dotted lines. (c) Transients of the photoluminescence decay for different excitation densities. A mono-exponential fit over the first 100 ps for an estimation of the lifetime is included. (d) Extracted lifetimes for two different samples at several individual sample positions with respect to the investigated excitation density regime.

in particular Auger recombination [40, 143], can be neglected. The extracted exciton lifetimes for both investigated samples are presented in fig. 4.20 (d). We find that excitons at ambient conditions show relatively long lifetimes of 60-80 ps over a multitude of investigated sample positions. For one sample a slight dependency of the lifetime on the injection density may be observed. This could be due to a finite amount of trap or defect states playing a more important role for lower excitation densities, but such considerations are a topic for further and more detailed investigations. Here it shall suffice to state that, given the averaging over a generally non-mono-exponential signal decay, these fluctuations are well within the experimental errors and should not be of significance in the further evaluations.

4.4.3 Exciton propagation in monolayer perovskites

Finally, the time- and spatially resolved measurements allow us to track the spatial broadening of the signal with time along the lines described in sec. 3.3.2. The corresponding relative change of the Gauss width $\Delta w(t)^2$ is depicted in fig. 4.21 (a) and the purely linear fits to the data are included. A representative set of data for the

investigated density regime is shown and vertically offset for clarity. Extracted diffusion coefficients for all measurements on both samples are depicted in fig. 4.21 (b) with respect to the excitation density. The extracted diffusion coefficients yield values in the range of 0.4 - 0.8 cm^2s^{-1}, with no observable density dependence, considering the experimental uncertainties. This yet again confirms that degradation effects, more pronounced for higher densities, while negligible for low densities, do to not influence exciton dynamics on the sub-nanosecond scale. Lastly, fig. 4.21 (c) is a summary of the statistical distribution of the extracted diffusion coefficient in form of a histogram. Included are all values from each of the 19 individual measurements. It is found that the measured diffusion coefficients are statistically centered around an average diffusion value of $0.6 \pm 0.05\,cm^2s^{-1}$. From this, taking a rather conservative exciton lifetime of

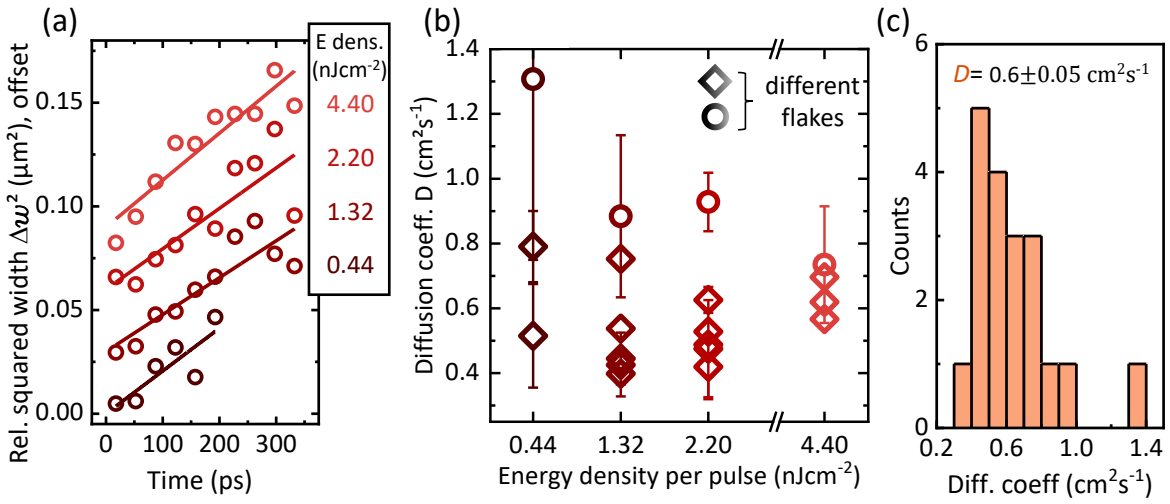

Figure 4.21: (a) Broadening of the relative squared width as a function of time from Gauss fits to the time- and spatially resolved photoluminescence experiments. A representative set of data is shown and vertically offset for clarity. (b) Extracted diffusion coefficient for two different encapsulated sample flakes and different excitation densities. Individual measurements were taken at different sample positions to reduce influence of sample decay. (c) Statistical distribution of the extracted diffusion coefficients shown in a histogram, including the results of 19 individual measurements.

around 60 ps, eq. 2.13 allows to estimate the average diffusion length to be around 120 nm, underlining that excitons can effectively diffuse over hundreds of lattice sites. We therefore find that efficient exciton diffusion in two-dimensional structures under ambient conditions is not limited to TMDC monolayers. This is particularly noteworthy in the context of perovskite structures being softer, and by nature more prone to disorder from dynamic fluctuations, than conventional semiconductor materials [182–186, 207]. Following from that, such efficient exciton transport is not easily expected

and stands as an encouraging finding, motivating broader investigations of propagation dynamics in these layered perovskite structures.

Furthermore, following inverse reasoning as in sec. 4.3.2.3, a measurement of the diffusion coefficient in principle allows to give estimates for the total exciton mass, using the Einstein relation (eq. 2.16). In order to estimate a value for the scattering time τ_s, we assume that the observed resonance linewidth broadening is dominated by scattering of excitons with lattice phonons and thus mainly homogeneously broadened. This, in general, is a reasonable consideration given the high phonon population at room temperature [23]. From eq. 2.5 we can then estimate the scattering time. Fits to the spectra of fig. 4.19 (e) yield the broadening to be around 60 meV, which corresponds to a scattering time $\tau_s \approx$11 fs. Finally, using an average diffusion coefficient of 0.6 $\mathrm{cm^2 s^{-1}}$, the Einstein relation gives a value for the total exciton mass of around 0.85 m_0. We remark that this estimation has to be taken with care, considering that for such a total mass, the expected values of the de Broglie wavelength and the mean free path approach similar values, in which case a classical diffusive description of propagation reaches its limits, as discussed in sec. 2.4. However, it should also be acknowledged that estimations and calculations for values of effective charge carrier and total exciton masses generally remain scarce, due to a lack of an accurate modeling of the electronic band structure (see sec. 2.5.1). The here presented estimations shall therefore serve as a prove of concept, that transport measurements can, in principle, provide means for an empirical approach to this problem. Furthermore, we note that for electron and hole effective masses on similar orders, our value of the total mass is in good agreement with measured reduced effective masses of 0.22 m_0 [210]. This is additionally supported by approximate calculations using a rescaling approach, that yielded 0.23 m_0, [175, 272, 273] for the here investigated BAPbI (N=1) perovskite compound.

In summary of this segment we find that full encapsulation of layered halide perovskites in hexagonal boron nitride provides a way to dramatically reduce light induced degradation of the material. This allows to investigate exciton propagation dynamics, where efficient diffusion of over more than 100 nm at ambient conditions is observed. These interesting findings stand as a proof of principle that the material class of ultrathin layered perovskites provide a platform for efficient propagation of optically excited charge carriers. Additionally, we demonstrate that precise measurements of exciton diffusion dynamics can also give a handle for accessing fundamental excitonic properties, such as their total mass. Finally, it is emphasized that the here conducted studies are just a first glimpse into a potentially wide field of exciton propagation dynamics in layered perovskites, where our findings shall be taken as motivation that such transport is generally remarkably efficient.

Chapter 5
Summary and outlook

In the frame of this work, various fundamental properties of excitons in two-dimensional, single layers of semiconducting materials have been studied. The first three segments thereby focused on the representative and prominent material system of monolayer transition metal dichalcogenides, specifically on tungsten based ones (WX_2). In context of the introduction, in particular the influences of the direct environment were taken into account. For this purpose it was initially shown, that high external magnetic fields can be used to investigate a very fundamental and intrinsic exciton property, which is of general interest for any physical system: their size. Monolayers of WS_2, encapsulated in hexagonal boron nitride, were investigated under magnetic fields up to 29 T in the facilities of the High Field Magnet Laboratory in Nijmegen. This first of all allowed to extract a valley Zeeman g-factor on the order of $g^{vZ} \approx -4.2$ for both ground and first excited exciton states, in good agreement with literature values. Moreover, such extensive fields allow to sufficiently resolve a diamagnetic shift that scales with the square of the magnetic field and is dependent on its underlying exciton state's size. Thus, the accurate tracking of this shift provided a way to estimate the radius of the observed exciton ground and first excited state to be on the order of 2 and 6-8 nm respectively. From that, the modeling of the exciton wave functions in a hydrogen-like framework confirmed the Wannier-Mott type exciton character, with the exciton wave functions extending over a multitude of lattice constants. In this context, it was further shown that such a 2D hydrogen model, while adequately accounting for the non-local screening of the environment, can provide an easy handle to appropriately describe basic excitonic properties in such two-dimensional materials.

From this knowledge of the exciton spatial extent, influences of disorder from fluctuations in the material's environment were studied. Here, two different scales of fluctuations were distinguished, that on the nano- and that on the microscale, whereas the lower limit of any relevant disorder was given by the exciton size. Therefore, two different WS_2 sample structures were studied. In one case, the flake was placed on a common SiO_2/Si sample, known to be afflicted by substantial disorder on the nanoscale from surface roughness. In the other case, the flake was encapsulated in high-quality boron nitride with an atomically flat surface. It was shown that disorder in the material's surroundings on the nanoscale, much smaller than typically probed areas, significantly influences observed exciton resonances. This was found to be due to resulting dis-

order in also the dielectric environment, giving rise to substantial fluctuations in the binding energies and free-particle bandgap. That in turn resulted in significant inhomogeneous broadening of the exciton resonances, particularly pronounced for higher excited states. Such dielectric disorder was further confirmed to be the origin for the majority of observed resonance broadening in bare monolayer samples at low temperatures. Motivated by such findings, detailed studies on the suppression of disorder in the encapsulated samples were conducted. Here, an approach of systematic white light scanning in combination with an automated fitting algorithm provided a way to analyze 100's of individual measurements. This, gave way to statistically analyze the enhancement of optical properties, gained from the encapsulation of samples and confirmed that nanoscale disorder can be suppressed in a controlled way over 100's of μm^2.

Furthermore, this method was found to be a powerful tool in investigating larger sample areas. It allowed to reconstruct spatial maps of excitonic transition energies or linewidth by tracking the resonances over the individual spectra obtained from systematic sample scanning. Here, tracking of the 1s-2s resonance separation in combination with a modified 2D-hydrogen model, gave way to construct spatial maps for estimated exciton binding and bandgap energies. Sharp transitions between areas of differing dielectric environment were found, with bandgap energies varying over multiple 10's of meV on spatial scales of only a few μm. This conveyed that large scale disorder can still be present, despite a satisfying suppression of disorder on the nanoscale. In particular, with respect to studies of propagation dynamics, such results have to be considered carefully. Lastly, this approach allowed to investigate influences from alternative sources of disorder, especially that of intrinsic doping, where it provided a way to track its spatial distribution from trion resonances. This can also be used to statistically analyze such trion resonances and shine light on the general properties of the two trion states. Here, ongoing studies find that one of the trions has a higher oscillator strength than the other, suggesting that trion dynamics are more complex than they might seem at a first glimpse. From this, incentive for a more thorough investigation is given and we remark that by including theoretical models provided by our collaborators (Ack. 8), progress in understanding such effects is already being made.

With access to well characterized structures of suppressed disorder, the spatial exciton propagation dynamics were studied. It was found that the diffusion efficiency is in general drastically enhanced, with diffusion coefficients as high as $10\,cm^2s^{-1}$ being more than one order of magnitude larger than in monolayers on disorder afflicted substrates. Furthermore, the concept of compound exciton-plasma diffusion was introduced in order to model an observed diffusion, which was too efficient to be brought into agreement with theoretical predictions of purely exciton-like propagation. It was shown that the inclusion of free charge carriers, potentially present under the experimental conditions,

can give rise to efficient propagation of electron-hole pairs. Viewing propagation as being driven by mobile free charge carriers, the predictions of such a model were in good agreement with experimentally obtained diffusion coefficients and it thus presents a promising hypothesis to explain the observed dynamics. However, such a model is yet found to be in contradiction with substantial amounts of doping, estimated to be present in the investigated structures, which is expected to suppress any formation of free charge carriers. While first measurements give indications that an electron-hole plasma can still be formed under room temperature conditions, these conflicting findings motivate a more thorough investigation of the underlying charge carrier dynamics. Here, novel gated sample structures fabricated in our laboratory can provide a way to unravel these discrepancies. Such devices allow the defined control of doping levels and thus open the way for a systematic study of the exciton-plasma equilibrium with respect to the influence of intrinsic free charge carriers. At the same time the resulting consequences for the propagation dynamics of the electron-hole pair ensemble can then be directly studied.

Motivated by the non-trivial findings in exciton diffusion at room temperature, studies under cryogenic conditions were performed to shine more light on the general propagation dynamics. However, an extremely short lifetime of the bright A-exciton state generally made investigations of exciton transport more challenging. Therefore, we switched to a different, but overall very similar TMDC system, that of WSe_2, where long lived emission on the low energy side of the photoluminescent spectrum was observed. Using polarization resolved spectroscopy as well as studying temperature dependency of the emission, the origin of these resonances was determined. It was found that these resonances are linked to long lived neutral and momentum-forbidden dark exciton states, which can scatter into the radiative cone via coupling to zone edge phonons. This phonon sideband emission provided a handle to track the dynamics of the underlying long-lived parent-states under cryogenic temperatures. First time- and spatially resolved photoluminescence measurements conveyed that excitons under such conditions can propagate extremely efficiently, with diffusion lengths on the order of $1\,\mu$m. Such high mobilities further suggest that defects and trap states only play subordinate roles at low temperatures, since the scattering times corresponding to such diffusion are already given by scattering with linear acoustic phonons alone. Finally, a non-linear decrease of the diffusion coefficient for slightly elevated temperature was observed, contradicting intuitive predictions from simple models. Such intriguing findings, yet again, motivate further studies. This is especially emphasized by a recently proposed model of quantum interference effects in exciton transport dynamics [247], which predicts a comparable trend of decreasing diffusion efficiency in similar temperature regimes. In this context this system provides a platform for the study of such

non-intuitive physical effects. In addition, it shall be noted that control over the intrinsic doping can help to understand the general exciton dynamics here as well. Tuning the structures to a neutral regime can provide a much more simple emission spectrum, since resonances from charged states can effectively be turned off. This would then give ways to study density dependent dynamics from phonon sidebands, since disturbing effects of especially the density dependent charged biexciton resonance could be dramatically suppressed. Finally, doping control can also open up a way in the other direction: Signals of charged exciton species can be enhanced and their dynamics can be studied and potentially even controlled or influenced by a second in-plane field.

In the last segment, a different material system was investigated, that of layered halide perovskites in their monolayer (N=1) form. Although having a structure entirely different from monolayer TMDCs, these materials show remarkably similar optical properties with extraordinarily high exciton binding energies. However, these systems are known to be susceptible to oxygen and water, in particular under the exposure of focused light, leading to a rapid degradation of their optical properties as was also shown in this work. Here, using the methods of encapsulation in high-quality boron nitride, it was confirmed that the volatile optical properties of these materials can be efficiently preserved, by effectively sealing them off from influences of the atmospheric surroundings. This allowed the study of exciton propagation dynamics that were previously hard to access. Applying the method established for the TMDC monolayers to the prototypical BAPbI compound, it was shown that excitons can, technically, propagate over substantial distances of more than 100 nm under ambient conditions. Such findings are particularly motivating considering the wide interest in these materials for potential applications. More importantly, however, these materials in general provide an interesting platform for the investigation of exciton propagation dynamics, with these measurements still being only a first proof of concept. Layered perovskites provide a huge diversity of compounds with direct access to their well defined dielectric environment in form of the organic layers, that can possibly allow for a tailoring of the propagation dynamics in a similar way as presented for TMDCs. Motivation is readily found from ongoing studies, demonstrating that a compound with interchanged organic separation layers can be substantially more stable, while at the same time also enhanced exciton diffusion is observed. Furthermore, first studies of temperature dependency provide insight into intriguing non-linearities, yet calling for a more thorough investigation. Lastly, the availability of optically accessible perovskites of multilayer structure (N>1), provides an alluring platform for the study of transport dynamics as well. In conclusion, our findings of efficient diffusion therefore should really be taken as an encouraging incentive for further research of exciton transport within the class of ultra-thin layered perovskites.

Acknowledgements

I sincerely thank our colleagues for fruitful collaborations and helpful discussions. Entries are in no particular order.

1. *High Field Magnet Laboratory (HFML), Radboud University Nijmegen, Netherlands*
   Anatoli A. Mitioglu
   Mariana V. Ballottin
   Peter C. M. Christianen

2. *Department of Physics, University of Regensburg, Germany*
   Johannes Holler
   Philipp Nagler
   Tobias Korn

3. *National High Field Laboratory, Los Alamos, New Mexico*
   Andreas V. Stier
   Scott A. Crooker

4. *Molecular Foundry, Berkeley National Laboratory, Berkeley, USA*
   Archana Raja

5. *Department of Applied Physics, Stanford University, Stanford, USA*
   Lutz Waldecker
   Tony F. Heinz

6. *National Institute for Materials Science, Ibaraki, Japan*
   Takashi Taniguchi
   Kenji Watanabe

7. *Department of Physics, Chalmers University of Technology, Gothenburg, Sweden*
   Raül Perea-Causin
   Samuel Brem
   Roberto Rosati
   Ermin Malic

8. *Ioffe Institute, Saint Petersburg, Russian Federation*
   Marina Semina
   Mikhail M. Glazov

9. *Department of Materials and Interfaces, Weizmann Institute of Science, Rehovot, Israel*
   Omer Yaffe
   Matan Menahem

Bibliography

[1]B. Lojek, *History of semiconductor engineering* (Springer, 2007) (cit. on p. 6).

[2]W. A. Atherton, "Miniaturization of Electronics", in *From Compass to Computer* (Macmillan Education UK, 1984), pp. 237–267 (cit. on p. 6).

[3]W. S. Wong and A. Salleo, eds., *Flexible Electronics* (Springer US, 2009) (cit. on p. 6).

[4]J. F. Wager, D. A. Keszler, and R. E. Presley, *Transparent Electronics* (Springer, 2007) (cit. on p. 6).

[5]M. Zou, Y. Ma, X. Yuan, Y. Hu, J. Liu, and Z. Jin, "Flexible devices: from materials, architectures to applications", Journal of Semiconductors **39**, 011010 (2018) (cit. on p. 6).

[6]H. Haug, *Quantum Theory Of The Optical And Electronic Properties Of Semiconductors (5Th Edition)* (Wspc, 2009) (cit. on p. 6).

[7]K. Hess, *Advanced Theory of Semiconductor Devices* (Wiley-IEEE Press, 1999) (cit. on p. 6).

[8]R. Thew, T. Jennewein, and M. Sasaki, "Focus on quantum science and technology initiatives around the world", Quantum Science and Technology **5**, 010201 (2019) (cit. on p. 6).

[9]H.-J. Warnecke and H.-J. Bullinger, *Kunststück Innovation: Praxisbeispiele aus der Fraunhofer-Gesellschaft (German Edition)* (Springer, 2013) (cit. on p. 6).

[10]H. Lüth, "Electronic Surface States", in *Surfaces and Interfaces of Solid Materials* (Springer Berlin Heidelberg, 1995), pp. 254–315 (cit. on p. 6).

[11]P. Szuromi, "Control and Use of Defects in Materials", Science **281**, 939–939 (1998) (cit. on p. 7).

[12]H. L. Tuller and S. R. Bishop, "Tailoring Material Properties through Defect Engineering", Chemistry Letters **39**, 1226–1231 (2010) (cit. on p. 7).

[13]A. K. Geim and I. V. Grigorieva, "Van der Waals heterostructures", Nature **499**, 419–425 (2013) (cit. on p. 7).

[14]P. K. Nayak, ed., *Two-dimensional Materials - Synthesis, Characterization and Potential Applications* (InTech, Aug. 2016) (cit. on p. 7).

[15]Y. Lu, *Two-Dimensional Materials in Nanophotonics: Developments, Devices, and Applications* (Jenny Stanford Publishing, 2019) (cit. on pp. 7–8).

[16]S. Haastrup, M. Strange, M. Pandey, T. Deilmann, P. S. Schmidt, N. F. Hinsche, M. N. Gjerding, D. Torelli, P. M. Larsen, A. C. Riis-Jensen, J. Gath, K. W. Jacobsen, J. J. Mortensen, T. Olsen, and K. S. Thygesen, "The Computational 2D Materials Database: high-throughput modeling and discovery of atomically thin crystals", 2D Materials **5**, 042002 (2018) (cit. on p. 7).

[17]K. S. Novoselov, "Electric Field Effect in Atomically Thin Carbon Films", Science **306**, 666–669 (2004) (cit. on pp. 7, 11, 47).

[18]K. S. Novoselov, A. K. Geim, S. V. Morozov, D. Jiang, M. I. Katsnelson, I. V. Grigorieva, S. V. Dubonos, and A. A. Firsov, "Two-dimensional gas of massless Dirac fermions in graphene", Nature **438**, 197–200 (2005) (cit. on pp. 7, 11).

[19]P. Ajayan, P. Kim, and K. Banerjee, "Two-dimensional van der Waals materials", Physics Today **69**, 38–44 (2016) (cit. on p. 7).

[20]K. F. Mak, C. Lee, J. Hone, J. Shan, and T. F. Heinz, "Atomically thin MoS 2: a new direct-gap semiconductor", Physical Review Letters **105**, 136805 (2010) (cit. on pp. 7, 11–12, 15).

[21]A. Splendiani, L. Sun, Y. Zhang, T. Li, J. Kim, C.-Y. Chim, G. Galli, and F. Wang, "Emerging photoluminescence in monolayer MoS2", Nano Letters **10**, 1271–1275 (2010) (cit. on pp. 7, 12–13, 15).

[22]H. Haug and S. Koch, "Semiconductor laser theory with many-body effects", Physical Review A **39**, 1887–1898 (1989) (cit. on pp. 7, 15–16).

[23]C. Klingshirn, *Semiconductor Optics*, 3rd (Springer, Berlin Heidelberg New York, 2007) (cit. on pp. 7, 15–17, 19–20, 31, 90, 117).

[24]G. Wang, A. Chernikov, M. M. Glazov, T. F. Heinz, X. Marie, T. Amand, and B. Urbaszek, "Colloquium : Excitons in atomically thin transition metal dichalcogenides", Reviews of Modern Physics **90**, 021001 (2018) (cit. on pp. 7, 19, 31, 33, 38, 63, 67, 75, 80, 82, 85).

[25]K. S. Novoselov, A. Mishchenko, A. Carvalho, and A. H. C. Neto, "2D materials and van der Waals heterostructures", Science **353**, aac9439 (2016) (cit. on p. 7).

[26]A. Castellanos-Gomez, M. Buscema, R. Molenaar, V. Singh, L. Janssen, H. S. Van der Zant, and G. A. Steele, "Deterministic transfer of two-dimensional materials by all-dry viscoelastic stamping", 2D Materials **1**, 011002 (2014) (cit. on pp. 7, 47).

[27]A. Chernikov, T. C. Berkelbach, H. M. Hill, A. Rigosi, Y. Li, O. B. Aslan, D. R. Reichman, M. S. Hybertsen, and T. F. Heinz, "Exciton binding energy and nonhydrogenic Rydberg series in monolayer WS2", Physical review letters **113**, 076802 (2014) (cit. on pp. 8, 16–19, 63).

[28]A. V. Stier, N. P. Wilson, K. A. Velizhanin, J. Kono, X. Xu, and S. A. Crooker, "Magnetooptics of Exciton Rydberg States in a Monolayer Semiconductor", Physical Review Letters **120**, 057405 (2018) (cit. on pp. 8, 17–19, 25, 29–30, 63, 65, 79).

[29]K. F. Mak, K. He, C. Lee, G. H. Lee, J. Hone, T. F. Heinz, and J. Shan, "Tightly bound trions in monolayer MoS2", Nature Materials **12**, 207–211 (2012) (cit. on pp. 8, 22, 82).

[30]J. S. Ross, S. Wu, H. Yu, N. J. Ghimire, A. M. Jones, G. Aivazian, J. Yan, D. G. Mandrus, D. Xiao, W. Yao, and X. Xu, "Electrical control of neutral and charged excitons in a monolayer semiconductor", Nature Communications **4**, 10.1038/ncomms2498 (2013) (cit. on pp. 8, 22–23).

[31]Y. You, X.-X. Zhang, T. C. Berkelbach, M. S. Hybertsen, D. R. Reichman, and T. F. Heinz, "Observation of biexcitons in monolayer WSe 2", Nature Physics **11**, 477–481 (2015) (cit. on pp. 8, 22, 24, 100, 106).

[32]Z. Ye, L. Waldecker, E. Y. Ma, D. Rhodes, A. Antony, B. Kim, X.-X. Zhang, M. Deng, Y. Jiang, Z. Lu, D. Smirnov, K. Watanabe, T. Taniguchi, J. Hone, and T. F. Heinz, "Efficient generation of neutral and charged biexcitons in encapsulated WSe2 monolayers", Nature Communications **9**, 10.1038/s41467-018-05917-8 (2018) (cit. on pp. 8, 22, 24).

[33]P. Nagler, M. V. Ballottin, A. A. Mitioglu, M. V. Durnev, T. Taniguchi, K. Watanabe, A. Chernikov, C. Schüller, M. M. Glazov, P. C. Christianen, and T. Korn, "Zeeman Splitting and Inverted Polarization of Biexciton Emission in Monolayer WS2", Physical Review Letters **121**, 10.1103/physrevlett.121.057402 (2018) (cit. on pp. 8, 22, 24).

[34]K. F. Mak, K. He, J. Shan, and T. F. Heinz, "Control of valley polarization in monolayer MoS 2 by optical helicity", Nature Nanotechnology **7**, 494 (2012) (cit. on pp. 8, 14).

[35]X. Xu, W. Yao, D. Xiao, and T. F. Heinz, "Spin and pseudospins in layered transition metal dichalcogenides", Nature Physics **10**, 343–350 (2014) (cit. on pp. 8, 15, 22, 27, 86).

[36]K. F. Mak, K. L. McGill, J. Park, and P. L. McEuen, "The valley Hall effect in MoS2 transistors", Science **344**, 1489–1492 (2014) (cit. on pp. 8, 15).

[37]D. Jariwala, V. K. Sangwan, L. J. Lauhon, T. J. Marks, and M. C. Hersam, "Emerging Device Applications for Semiconducting Two-Dimensional Transition Metal Dichalcogenides", ACS Nano **8**, 1102–1120 (2014) (cit. on p. 8).

[38]D. Z. Mingxiao Ye and Y. K. Yap, "Recent Advances in Electronic and Optoelectronic Devices Based on Two-Dimensional Transition Metal Dichalcogenides", Electronics **6**, 43 (2017) (cit. on p. 8).

[39]N. Kumar, Q. Cui, F. Ceballos, D. He, Y. Wang, and H. Zhao, "Exciton diffusion in monolayer and bulk MoSe2", Nanoscale **6**, 4915–4919 (2014) (cit. on pp. 8, 35, 37, 86).

[40]M. Kulig, J. Zipfel, P. Nagler, S. Blanter, C. Schüller, T. Korn, N. Paradiso, M. M. Glazov, and A. Chernikov, "Exciton Diffusion and Halo Effects in Monolayer Semiconductors", Physical Review Letters **120**, 10.1103/physrevlett.120.207401 (2018) (cit. on pp. 8, 35, 37, 86, 88–90, 106–107, 115).

[41]R. Frindt, "The optical properties of single crystals of WSe2 and MoTe2", Journal of Physics and Chemistry of Solids **24**, 1107–1108 (1963) (cit. on pp. 10, 12).

[42]B. Evans and P. Young, "Exciton spectra in thin crystals: the diamagnetic effect", Proceedings of the Physical Society **91**, 475 (1967) (cit. on pp. 10, 12, 25).

[43]P. G. Harper and D. R. Edmodson, "Electronic band structure of the layer-type crystal MoS2 (atomic model)", Physica Status Solidi (b) **44**, 59–69 (1971) (cit. on pp. 10, 12).

[44]J. Wilson and A. Yoffe, "The transition metal dichalcogenides discussion and interpretation of the observed optical, electrical and structural properties", Advances in Physics **18**, 193–335 (1969) (cit. on pp. 10, 12).

[45]G.-B. Liu, D. Xiao, Y. Yao, X. Xu, and W. Yao, "Electronic structures and theoretical modelling of two- dimensional group-VIB transition metal dichalcogenides", Chemical Society Reviews **44**, 2643–2663 (2015) (cit. on pp. 10–11, 13).

[46]J. Heising and M. G. Kanatzidis, "Exfoliated and Restacked MoS2and WS2: Ionic or Neutral Species? Encapsulation and Ordering of Hard Electropositive Cations", Journal of the American Chemical Society **121**, 11720–11732 (1999) (cit. on p. 10).

[47]G. Eda, T. Fujita, H. Yamaguchi, D. Voiry, M. Chen, and M. Chhowalla, "Coherent Atomic and Electronic Heterostructures of Single-Layer MoS2", ACS Nano **6**, 7311–7317 (2012) (cit. on p. 10).

[48]T. A. Loh and D. H. Chua, "Origin of Hybrid 1T- and 2H-WS2 Ultrathin Layers by Pulsed Laser Deposition", The Journal of Physical Chemistry C **119**, 27496–27504 (2015) (cit. on p. 10).

[49]T. Jiang, H. Liu, D. Huang, S. Zhang, Y. Li, X. Gong, Y.-R. Shen, W.-T. Liu, and S. Wu, "Valley and band structure engineering of folded MoS2 bilayers", Nature Nanotechnology **9**, 825–829 (2014) (cit. on p. 10).

[50]R. Suzuki, M. Sakano, Y. J. Zhang, R. Akashi, D. Morikawa, A. Harasawa, K. Yaji, K. Kuroda, K. Miyamoto, T. Okuda, K. Ishizaka, R. Arita, and Y. Iwasa, "Valley-dependent spin polarization in bulk MoS2 with broken inversion symmetry", Nature Nanotechnology **9**, 611–617 (2014) (cit. on p. 10).

[51]D. Xiao, W. Yao, and Q. Niu, "Valley-Contrasting Physics in Graphene: Magnetic Moment and Topological Transport", Physical Review Letters **99**, 10.1103/physrevlett.99.236809 (2007) (cit. on p. 11).

[52]W. Yao, D. Xiao, and Q. Niu, "Valley-dependent optoelectronics from inversion symmetry breaking", Physical Review B **77**, 10.1103/physrevb.77.235406 (2008) (cit. on p. 11).

[53]H. Zeng, G.-B. Liu, J. Dai, Y. Yan, B. Zhu, R. He, L. Xie, S. Xu, X. Chen, W. Yao, et al., "Optical signature of symmetry variations and spin-valley coupling in atomically thin tungsten dichalcogenides", Scientific reports **3**, 1608 (2013) (cit. on pp. 12–13).

[54]D. MacNeill, C. Heikes, K. F. Mak, Z. Anderson, A. Kormányos, V. Zólyomi, J. Park, and D. C. Ralph, "Breaking of Valley Degeneracy by Magnetic Field in Monolayer MoSe2", Physical Review Letters **114**, 037401 (2015) (cit. on pp. 13, 15, 25–26).

[55]A. Srivastava, M. Sidler, A. V. Allain, D. S. Lembke, A. Kis, and A. Imamoğlu, "Valley Zeeman effect in elementary optical excitations of monolayer WSe 2", Nature Physics **11**, 141 (2015) (cit. on pp. 13, 15, 25–26).

[56]A. Kormányos, G. Burkard, M. Gmitra, J. Fabian, V. Zólyomi, N. D. Drummond, and V. Falko, "k· p theory for two-dimensional transition metal dichalcogenide semiconductors", 2D Materials **2**, 022001 (2015) (cit. on pp. 13–14, 17, 21–22, 69–70, 80, 90–94, 108).

[57]T. Scrace, Y. Tsai, B. Barman, L. Schweidenback, A. Petrou, G. Kioseoglou, I. Ozfidan, M. Korkusinski, and P. Hawrylak, "Magnetoluminescence and valley polarized state of a two-dimensional electron gas in WS2 monolayers", Nature Nanotechnology **10**, 603–607 (2015) (cit. on pp. 13–14, 21).

[58]G.-B. Liu, W.-Y. Shan, Y. Yao, W. Yao, and D. Xiao, "Three-band tight-binding model for monolayers of group-VIB transition metal dichalcogenides", Physical Review B **88**, 10.1103/physrevb.88.085433 (2013) (cit. on p. 14).

[59]T. Cao, G. Wang, W. Han, H. Ye, C. Zhu, J. Shi, Q. Niu, P. Tan, E. Wang, B. Liu, and J. Feng, "Valley-selective circular dichroism of monolayer molybdenum disulphide", Nature Communications **3**, 10.1038/ncomms1882 (2012) (cit. on p. 14).

[60]G. Sallen, L. Bouet, X. Marie, G. Wang, C. Zhu, W. Han, Y. Lu, P. Tan, T. Amand, B. Liu, et al., "Robust optical emission polarization in MoS 2 monolayers through selective valley excitation", Physical Review B **86**, 081301 (2012) (cit. on p. 14).

[61]D. Xiao, G.-B. Liu, W. Feng, X. Xu, and W. Yao, "Coupled spin and valley physics in monolayers of MoS 2 and other group-VI dichalcogenides", Physical Review Letters **108**, 196802 (2012) (cit. on pp. 14, 22, 27).

[62]A. M. Jones, H. Yu, N. J. Ghimire, S. Wu, G. Aivazian, J. S. Ross, B. Zhao, J. Yan, D. G. Mandrus, D. Xiao, W. Yao, and X. Xu, "Optical generation of excitonic valley coherence in monolayer WSe2", Nature Nanotechnology **8**, 634–638 (2013) (cit. on p. 14).

[63]G. Wang, C. Robert, M. Glazov, F. Cadiz, E. Courtade, T. Amand, D. Lagarde, T. Taniguchi, K. Watanabe, B. Urbaszek, and X. Marie, "In-Plane Propagation of Light in Transition Metal Dichalcogenide Monolayers: Optical Selection Rules", Physical Review Letters **119**, 10.1103/physrevlett.119.047401 (2017) (cit. on pp. 14–15, 22, 91, 100).

[64]Y. Yanagi and H. Kusunose, "Optical Selection Rules in Spin–Orbit Coupled Systems on Honeycomb Lattice", Journal of the Physical Society of Japan **86**, 083703 (2017) (cit. on pp. 14–15).

[65]G. Aivazian, Z. Gong, A. M. Jones, R.-L. Chu, J. Yan, D. G. Mandrus, C. Zhang, D. Cobden, W. Yao, and X. Xu, "Magnetic control of valley pseudospin in monolayer WSe2", Nature Physics **11**, 148 (2015) (cit. on pp. 15, 25–26).

[66]N. S. Rytova, "Screened potential of a point charge in a thin film", Proc. MSU, Phys., Astron. **3**, 30 (1967) (cit. on pp. 15, 18).

[67]L. V. Keldysh, "Coulomb interaction in thin semiconductor and semimetal films", Journal of Experimental and Theoretical Physics Letters, Vol. 29, p.658 (1979) (cit. on pp. 15, 18).

[68]P. Cudazzo, I. V. Tokatly, and A. Rubio, "Dielectric screening in two-dimensional insulators: Implications for excitonic and impurity states in graphane", Physical Review B **84**, 085406 (2011) (cit. on pp. 15, 17, 19).

[69]T. C. Berkelbach, M. S. Hybertsen, and D. R. Reichman, "Theory of neutral and charged excitons in monolayer transition metal dichalcogenides", Physical Review B **88**, 045318 (2013) (cit. on pp. 15, 17–18, 23, 69–70).

[70]M. M. Ugeda, A. J. Bradley, S.-F. Shi, H. Felipe, Y. Zhang, D. Y. Qiu, W. Ruan, S.-K. Mo, Z. Hussain, Z.-X. Shen, et al., "Giant bandgap renormalization and excitonic effects in a monolayer transition metal dichalcogenide semiconductor", Nature materials **13**, 1091 (2014) (cit. on p. 16).

[71]A. Raja, A. Chaves, J. Yu, G. Arefe, H. M. Hill, A. F. Rigosi, T. C. Berkelbach, P. Nagler, C. Schüller, T. Korn, et al., "Coulomb engineering of the bandgap and excitons in two-dimensional materials", Nature Communications **8**, 15251 (2017) (cit. on pp. 16, 33, 65).

[72]K. T. Winther and K. S. Thygesen, "Band structure engineering in van der Waals heterostructures via dielectric screening: the GΔW method", 2D Materials **4**, 025059 (2017) (cit. on p. 16).

[73]J. Singh, "Theory of Excitons", in *Excitation Energy Transfer Processes in Condensed Matter* (Springer US, 1994), pp. 1–45 (cit. on pp. 16–17).

[74]Y. Li, A. Chernikov, X. Zhang, A. Rigosi, H. M. Hill, A. M. van der Zande, D. A. Chenet, E.-M. Shih, J. Hone, and T. F. Heinz, "Measurement of the optical dielectric function of monolayer transition-metal dichalcogenides: MoS2, MoSe2, WS2, and WSe2", Physical Review B **90**, 205422 (2014) (cit. on p. 16).

[75]D. Y. Qiu, F. H. da Jornada, and S. G. Louie, "Optical spectrum of MoS$_{2}$: Many-body effects and diversity of exciton states", Physical Review Letters **111**, 216805 (2013) (cit. on p. 16).

[76]G. Berghaeuser and E. Malic, "Analytical approach to excitonic properties of MoS2", Physical Review B **89**, 10.1103/physrevb.89.125309 (2014) (cit. on p. 16).

[77]M. Rösner, C. Steinke, M. Lorke, C. Gies, F. Jahnke, and T. O. Wehling, "Two-Dimensional Heterojunctions from Nonlocal Manipulations of the Interactions", Nano Letters **16**, 2322–2327 (2016) (cit. on p. 16).

[78]G. H. Wannier, "The structure of electronic excitation levels in insulating crystals", Physical Review **52**, 191 (1937) (cit. on pp. 16–17, 63).

[79]J. Chang, L. F. Register, and S. K. Banerjee, "Ballistic performance comparison of monolayer transition metal dichalcogenide MX2 (M = Mo, W; X = S, Se, Te) metal-oxide-semiconductor field effect transistors", Journal of Applied Physics **115**, 084506 (2014) (cit. on pp. 17, 90, 108).

[80]H. Shi, H. Pan, Y.-W. Zhang, and B. I. Yakobson, "Quasiparticle band structures and optical properties of strained monolayer MoS2and WS2", Physical Review B **87**, 10.1103/physrevb.87.155304 (2013) (cit. on pp. 17, 90, 108).

[81]D. Wickramaratne, F. Zahid, and R. K. Lake, "Electronic and thermoelectric properties of few-layer transition metal dichalcogenides", The Journal of Chemical Physics **140**, 124710 (2014) (cit. on pp. 17, 90, 108).

[82]S. Latini, T. Olsen, and K. S. Thygesen, "Excitons in van der Waals heterostructures: The important role of dielectric screening", Physical Review B **92**, 10.1103/physrevb.92.245123 (2015) (cit. on p. 17).

[83]J. Zipfel, J. Holler, A. A. Mitioglu, M. V. Ballottin, P. Nagler, A. V. Stier, T. Taniguchi, K. Watanabe, S. A. Crooker, P. C. Christianen, et al., "Spatial extent of the excited exciton states in WS 2 monolayers from diamagnetic shifts", Physical Review B **98**, 075438 (2018) (cit. on pp. 18, 25, 63).

[84]T. C. Berkelbach and D. R. Reichman, "Optical and Excitonic Properties of Atomically Thin Transition-Metal Dichalcogenides", Annual Review of Condensed Matter Physics **9**, 379–396 (2018) (cit. on pp. 18, 70).

[85]H. Yu, X. Cui, X. Xu, and W. Yao, "Valley excitons in two-dimensional semiconductors", National Science Review **2**, 57–70 (2015) (cit. on pp. 19, 33).

[86]G. Moody, C. K. Dass, K. Hao, C.-H. Chen, L.-J. Li, A. Singh, K. Tran, G. Clark, X. Xu, G. BerghÃ¤user, E. Malic, A. Knorr, and X. Li, "Intrinsic homogeneous linewidth and broadening mechanisms of excitons in monolayer transition metal dichalcogenides", Nature Communications **6**, 10.1038/ncomms9315 (2015) (cit. on pp. 20, 99, 102).

[87]C. Poellmann, P. Steinleitner, U. Leierseder, P. Nagler, G. Plechinger, M. Porer, R. Bratschitsch, C. Schüller, T. Korn, and R. Huber, "Resonant internal quantum transitions and femtosecond radiative decay of excitons in monolayer WSe2", Nature Materials **14**, 889–893 (2015) (cit. on pp. 20, 99, 102).

[88]M. Palummo, M. Bernardi, and J. C. Grossman, "Exciton Radiative Lifetimes in Two-Dimensional Transition Metal Dichalcogenides", Nano Letters **15**, 2794–2800 (2015) (cit. on pp. 20, 99, 102).

[89]T. Jakubczyk, V. Delmonte, M. Koperski, K. Nogajewski, C. Faugeras, W. Langbein, M. Potemski, and J. Kasprzak, "Radiatively Limited Dephasing and Exciton Dynamics in MoSe2 Monolayers Revealed with Four-Wave Mixing Microscopy", Nano Letters **16**, 5333–5339 (2016) (cit. on pp. 20, 99, 102).

[90]C. Robert, D. Lagarde, F. Cadiz, G. Wang, B. Lassagne, T. Amand, A. Balocchi, P. Renucci, S. Tongay, B. Urbaszek, and X. Marie, "Exciton radiative lifetime in transition metal dichalcogenide monolayers", Physical Review B **93**, 10.1103/physrevb.93.205423 (2016) (cit. on pp. 20, 99, 102).

[91]M. M. Glazov, T. Amand, X. Marie, D. Lagarde, L. Bouet, and B. Urbaszek, "Exciton fine structure and spin decoherence in monolayers of transition metal dichalcogenides", Physical Review B **89**, 10.1103/physrevb.89.201302 (2014) (cit. on p. 20).

[92]S. Brem, J. Zipfel, M. Selig, A. Raja, L. Waldecker, J. D. Ziegler, T. Taniguchi, K. Watanabe, A. Chernikov, and E. Malic, "Intrinsic lifetime of higher excitonic states in tungsten diselenide monolayers", Nanoscale **11**, 12381–12387 (2019) (cit. on pp. 20, 75–76, 90, 109).

[93]E. Malic, M. Selig, M. Feierabend, S. Brem, D. Christiansen, F. Wendler, A. Knorr, and G. Berghäuser, "Dark excitons in transition metal dichalcogenides", Physical Review Materials **2**, 10.1103/physrevmaterials.2.014002 (2018) (cit. on pp. 21–22, 91, 102).

[94]G. Berghäuser, P. Steinleitner, P. Merkl, R. Huber, A. Knorr, and E. Malic, "Mapping of the dark exciton landscape in transition metal dichalcogenides", Physical Review B **98**, 10.1103/physrevb.98.020301 (2018) (cit. on p. 21).

[95]J. P. Echeverry, B. Urbaszek, T. Amand, X. Marie, and I. C. Gerber, "Splitting between bright and dark excitons in transition metal dichalcogenide monolayers", Physical Review B **93**, 10.1103/physrevb.93.121107 (2016) (cit. on p. 21).

[96]T. C. Berkelbach, M. S. Hybertsen, and D. R. Reichman, "Bright and dark singlet excitons via linear and two-photon spectroscopy in monolayer transition-metal dichalcogenides", Physical Review B **92**, 10.1103/physrevb.92.085413 (2015) (cit. on p. 21).

[97]H. Zhang, C. Berthod, H. Berger, T. Giamarchi, and A. F. Morpurgo, "Band Filling and Cross Quantum Capacitance in Ion-Gated Semiconducting Transition Metal Dichalcogenide Monolayers", Nano Letters **19**, 8836–8845 (2019) (cit. on p. 21).

[98]T. Deilmann and K. S. Thygesen, "Finite-momentum exciton landscape in mono- and bilayer transition metal dichalcogenides", 2D Materials **6**, 035003 (2019) (cit. on pp. 22, 91).

[99]X.-X. Zhang, T. Cao, Z. Lu, Y.-C. Lin, F. Zhang, Y. Wang, Z. Li, J. C. Hone, J. A. Robinson, D. Smirnov, S. G. Louie, and T. F. Heinz, "Magnetic brightening and control of dark excitons in monolayer WSe2", Nature Nanotechnology **12**, 883–888 (2017) (cit. on p. 22).

[100]Y. Zhou, G. Scuri, D. S. Wild, A. A. High, A. Dibos, L. A. Jauregui, C. Shu, K. D. Greve, K. Pistunova, A. Y. Joe, T. Taniguchi, K. Watanabe, P. Kim, M. D. Lukin, and H. Park, "Probing dark excitons in atomically thin semiconductors via near-field coupling to surface plasmon polaritons", Nature Nanotechnology **12**, 856–860 (2017) (cit. on pp. 22, 100).

[101]C. Zhang, H. Wang, W. Chan, C. Manolatou, and F. Rana, "Absorption of light by excitons and trions in monolayers of metal dichalcogenide Mo S2: Experiments and theory", Physical Review B **89**, 205436 (2014) (cit. on p. 22).

[102]B. Ganchev, N. Drummond, I. Aleiner, and V. Fal'ko, "Three-Particle Complexes in Two-Dimensional Semiconductors", Physical Review Letters **114**, 10.1103/physrevlett.114.107401 (2015) (cit. on p. 22).

[103]E. Courtade, M. Semina, M. Manca, M. M. Glazov, C. Robert, F. Cadiz, G. Wang, T. Taniguchi, K. Watanabe, M. Pierre, W. Escoffier, E. L. Ivchenko, P. Renucci, X. Marie, T. Amand, and B. Urbaszek, "Charged excitons in monolayer WSe2: Experiment and theory", Physical Review B **96**, 085302 (2017) (cit. on pp. 22–23, 64, 82–83, 85).

[104]G. Plechinger, P. Nagler, J. Kraus, N. Paradiso, C. Strunk, C. SchÃ¼ller, and T. Korn, "Identification of excitons, trions and biexcitons in single-layer WS2", physica status solidi (RRL) - Rapid Research Letters **9**, 457–461 (2015) (cit. on pp. 22, 24).

[105]G. Plechinger, P. Nagler, A. Arora, R. Schmidt, A. Chernikov, A. G. del Águila, P. C. Christianen, R. Bratschitsch, C. Schüller, and T. Korn, "Trion fine structure and coupled spin–valley dynamics in monolayer tungsten disulfide", Nature Communications **7**, 10.1038/ncomms12715 (2016) (cit. on pp. 22, 83, 100).

[106]A. Steinhoff, M. Florian, A. Singh, K. Tran, M. Kolarczik, S. Helmrich, A. W. Achtstein, U. Woggon, N. Owschimikow, F. Jahnke, and X. Li, "Biexciton fine structure in monolayer transition metal dichalcogenides", Nature Physics **14**, 1199–1204 (2018) (cit. on pp. 22, 24).

[107]M. Barbone, A. R.-P. Montblanch, D. M. Kara, C. Palacios-Berraquero, A. R. Cadore, D. D. Fazio, B. Pingault, E. Mostaani, H. Li, B. Chen, K. Watanabe, T. Taniguchi, S. Tongay, G. Wang, A. C. Ferrari, and M. Atatüre, "Charge-tuneable biexciton complexes in monolayer WSe2", Nature Communications **9**, 10.1038/s41467-018-05632-4 (2018) (cit. on p. 22).

[108]M. Danovich, V. Zólyomi, and V. I. Fal'ko, "Dark trions and biexcitons in WS2 and WSe2 made bright by e-e scattering", Scientific Reports **7**, 10.1038/srep45998 (2017) (cit. on p. 23).

[109]E. Liu, J. van Baren, Z. Lu, M. M. Altaiary, T. Taniguchi, K. Watanabe, D. Smirnov, and C. H. Lui, "Gate Tunable Dark Trions in Monolayer WSe2", Physical Review Letters **123**, 10.1103/physrevlett.123.027401 (2019) (cit. on p. 23).

[110]M. Bugajski, W. Kuszko, and K. Regiński, "Diamagnetic shift of exciton energy levels in GaAs-Ga1- xAlxAs quantum wells", Solid state communications **60**, 669–673 (1986) (cit. on p. 25).

[111]N. Miura, *Physics of Semiconductors in High Magnetic Fields (Series on Semiconductor Science and Technology)* (Oxford University Press, 2007) (cit. on pp. 25, 28).

[112]S. Tarucha, H. Okamoto, Y. Iwasa, and N. Miura, "Exciton binding energy in GaAs quantum wells deduced from magneto-optical absorption measurement", Solid state communications **52**, 815–819 (1984) (cit. on p. 25).

[113]W. Edelstein, H. N. Spector, and R. Marasas, "Two-dimensional excitons in magnetic fields", Physical Review B **39**, 7697 (1989) (cit. on pp. 25, 28).

[114]A. A. Mitioglu, P. Plochocka, Á. Granados del Aguila, P. C. M. Christianen, G. Deligeorgis, S. Anghel, L. Kulyuk, and D. K. Maude, "Optical Investigation of Monolayer and Bulk Tungsten Diselenide (WSe 2) in High Magnetic Fields", Nano Letters **15**, 4387–4392 (2015) (cit. on p. 25).

[115]G. Plechinger, P. Nagler, A. Arora, A. Granados del Águila, M. V. Ballottin, T. Frank, P. Steinleitner, M. Gmitra, J. Fabian, P. C. Christianen, et al., "Excitonic valley effects in monolayer WS2 under high magnetic fields", Nano Letters **16**, 7899–7904 (2016) (cit. on pp. 25, 67).

[116]A. V. Stier, K. M. McCreary, B. T. Jonker, J. Kono, and S. A. Crooker, "Exciton diamagnetic shifts and valley Zeeman effects in monolayer WS2 and MoS2 to 65 Tesla", Nature Communications **7**, 10643 (2016) (cit. on pp. 25, 63, 67, 69).

[117]R. Schmidt, A. Arora, G. Plechinger, P. Nagler, A. G. del Águila, M. V. Ballottin, P. C. Christianen, S. M. de Vasconcellos, C. Schüller, T. Korn, et al., "Magnetic-field-induced rotation of polarized light emission from monolayer WS2", Physical Review Letters **117**, 077402 (2016) (cit. on pp. 25, 67).

[118]A. Arora, M. Drüppel, R. Schmidt, T. Deilmann, R. Schneider, M. R. Molas, P. Marauhn, S. M. de Vasconcellos, M. Potemski, M. Rohlfing, et al., "Interlayer excitons in a bulk van der Waals semiconductor", Nature Communications **8**, 639 (2017) (cit. on p. 25).

[119]M. Goryca, J. Li, A. V. Stier, T. Taniguchi, K. Watanabe, E. Courtade, S. Shree, C. Robert, B. Urbaszek, X. Marie, and S. A. Crooker, "Revealing exciton masses and dielectric properties of monolayer semiconductors with high magnetic fields", Nature Communications **10**, 10.1038/s41467-019-12180-y (2019) (cit. on pp. 25, 30, 69, 80, 97).

[120]M. Koperski, M. R. Molas, A. Arora, K. Nogajewski, M. Bartos, J. Wyzula, D. Vaclavkova, P. Kossacki, and M. Potemski, "Orbital, spin and valley contributions to Zeeman splitting of excitonic resonances in MoSe 2 , WSe 2 and WS 2 Monolayers", 2D Materials **6**, 015001 (2018) (cit. on p. 27).

[121]K. J. Nash, M. S. Skolnick, P. A. Claxton, and J. S. Roberts, "Diamagnetism as a probe of exciton localization in quantum wells", Physical Review B **39**, 10943–10954 (1989) (cit. on p. 28).

[122]S. Walck and T. Reinecke, "Exciton diamagnetic shift in semiconductor nanostructures", Physical Review B **57**, 9088 (1998) (cit. on p. 28).

[123]M. Sugawara, N. Okazaki, T. Fujii, and S. Yamazaki, "Diamagnetic shift and oscillator strength of two-dimensional excitons under a magnetic field in In 0.53 Ga 0.47 As/InP quantum wells", Physical Review B **48**, 8848 (1993) (cit. on p. 28).

[124]X. L. Yang, S. H. Guo, F. T. Chan, K. W. Wong, and W. Y. Ching, "Analytic solution of a two-dimensional hydrogen atom. I. Nonrelativistic theory", Physical Review A **43**, 1186–1196 (1991) (cit. on pp. 28, 70–71).

[125]O. Akimoto and H. Hasegawa, "Interband Optical Transitions in Extremely Anisotropic Semiconductors. II. Coexistence of Exciton and the Landau Levels", Journal of the Physical Society of Japan **22**, 181–191 (1967) (cit. on p. 28).

[126]A. H. MacDonald and D. S. Ritchie, "Hydrogenic energy levels in two dimensions at arbitrary magnetic fields", Physical Review B **33**, 8336–8344 (1986) (cit. on p. 28).

[127]R.-L. Chu, X. Li, S. Wu, Q. Niu, W. Yao, X. Xu, and C. Zhang, "Valley-splitting and valley-dependent inter-Landau-level optical transitions in monolayerMoS2quantum Hall systems", Physical Review B **90**, 10.1103/physrevb.90.045427 (2014) (cit. on p. 28).

[128]M. Bieniek, M. Korkusiński, L. Szulakowska, P. Potasz, I. Ozfidan, and P. Hawrylak, "Band nesting, massive Dirac fermions, and valley Landé and Zeeman effects in transition metal dichalcogenides: A tight-binding model", Physical Review B **97**, 10.1103/physrevb.97.085153 (2018) (cit. on p. 28).

[129]T. Smoleński, O. Cotlet, A. Popert, P. Back, Y. Shimazaki, P. Knüppel, N. Dietler, T. Taniguchi, K. Watanabe, M. Kroner, and A. Imamoglu, "Interaction-Induced Shubnikov–de Haas Oscillations in Optical Conductivity of Monolayer MoSe2", Physical Review Letters **123**, 10.1103/physrevlett.123.097403 (2019) (cit. on p. 28).

[130]Z. Wang, J. Shan, and K. F. Mak, "Valley- and spin-polarized Landau levels in monolayer WSe2", Nature Nanotechnology **12**, 144–149 (2016) (cit. on p. 29).

[131]Y. Cho and T. C. Berkelbach, "Environmentally sensitive theory of electronic and optical transitions in atomically thin semiconductors", Physical Review B **97**, 10.1103/physrevb.97.041409 (2018) (cit. on pp. 31, 33, 69).

[132]A. Raja, L. Waldecker, J. Zipfel, Y. Cho, S. Brem, J. D. Ziegler, M. Kulig, T. Taniguchi, K. Watanabe, E. Malic, T. F. Heinz, T. C. Berkelbach, and A. Chernikov, "Dielectric disorder in two-dimensional materials", Nature Nanotechnology **14**, 832–837 (2019) (cit. on pp. 32–34, 76, 78).

[133]X. Hong, T. Ishihara, and A. V. Nurmikko, "Dielectric confinement effect on excitons inPbI4-based layered semiconductors", Physical Review B **45**, 6961–6964 (1992) (cit. on pp. 33, 42, 45).

[134]M. I. B. Utama, H. Kleemann, W. Zhao, C. S. Ong, F. H. da Jornada, D. Y. Qiu, H. Cai, H. Li, R. Kou, S. Zhao, S. Wang, K. Watanabe, T. Taniguchi, S. Tongay, A. Zettl, S. G. Louie, and F. Wang, "A dielectric-defined lateral heterojunction in a monolayer semiconductor", Nature Electronics **2**, 60–65 (2019) (cit. on p. 33).

[135]D. Rhodes, S. H. Chae, R. Ribeiro-Palau, and J. Hone, "Disorder in van der Waals heterostructures of 2D materials", Nature Materials **18**, 541–549 (2019) (cit. on pp. 33–34).

[136]S. J. Haigh, A. Gholinia, R. Jalil, S. Romani, L. Britnell, D. C. Elias, K. S. Novoselov, L. A. Ponomarenko, A. K. Geim, and R. Gorbachev, "Cross-sectional imaging of individual layers and buried interfaces of graphene-based heterostructures and superlattices", Nature Materials **11**, 764–767 (2012) (cit. on p. 33).

[137]C. Zhou, W. Yang, and H. Zhu, "Mechanism of charge transfer and its impacts on Fermi-level pinning for gas molecules adsorbed on monolayer WS2", The Journal of Chemical Physics **142**, 214704 (2015) (cit. on p. 33).

[138]F. Cadiz, C. Robert, E. Courtade, M. Manca, L. Martinelli, T. Taniguchi, K. Watanabe, T. Amand, A. C. H. Rowe, D. Paget, B. Urbaszek, and X. Marie, "Exciton diffusion in WSe2 monolayers embedded in a van der Waals heterostructure", Applied Physics Letters **112**, 152106 (2018) (cit. on pp. 35, 37, 86, 90).

[139]H. Hillmer, S. Hansmann, A. Forchel, M. Morohashi, E. Lopez, H. P. Meier, and K. Ploog, "Two-dimensional exciton transport in GaAs/GaAlAs quantum wells", Applied Physics Letters **53**, 1937–1939 (1988) (cit. on pp. 35, 86).

[140]F. Steininger, A. Knorr, T. Stroucken, P. Thomas, and S. W. Koch, "Dynamic Evolution of Spatiotemporally Localized Electronic Wave Packets in Semiconductor Quantum Wells", Physical Review Letters **77**, 550–553 (1996) (cit. on p. 35).

[141]L. V. Butov, A. C. Gossard, and D. S. Chemla, "Macroscopically ordered state in an exciton system", Nature **418**, 751–754 (2002) (cit. on p. 35).

[142]A. A. High, A. T. Hammack, J. R. Leonard, S. Yang, L. V. Butov, T. Ostatnický, M. Vladimirova, A. V. Kavokin, T. C. H. Liew, K. L. Campman, and A. C. Gossard, "Spin Currents in a Coherent Exciton Gas", Physical Review Letters **110**, 10.1103/physrevlett.110.246403 (2013) (cit. on pp. 35, 86).

[143]S. Mouri, Y. Miyauchi, M. Toh, W. Zhao, G. Eda, and K. Matsuda, "Nonlinear photoluminescence in atomically thin layeredWSe2arising from diffusion-assisted exciton-exciton annihilation", Physical Review B **90**, 10.1103/physrevb.90.155449 (2014) (cit. on pp. 37, 86, 90, 115).

[144]N. S. Ginsberg and W. A. Tisdale, "Spatially Resolved Exciton and Charge Transport in Emerging Semiconductors", Annual Review of Physical Chemistry **71**, 10.1146/annurev-physchem-052516-050703 (2020) (cit. on pp. 37, 40, 86).

[145]M. Seitz, A. J. Magdaleno, N. Alcázar-Cano, M. Meléndez, T. J. Lubbers, S. W. Walraven, S. Pakdel, E. Prada, R. Delgado-Buscalioni, and F. Prins, "Exciton diffusion in two-dimensional metal-halide perovskites", (2020) (cit. on pp. 37, 111–112).

[146]T. Kato and T. Kaneko, "Transport Dynamics of Neutral Excitons and Trions in Monolayer WS2", ACS Nano **10**, 9687–9694 (2016) (cit. on pp. 37, 86).

[147]J. Wang, Y. Guo, Y. Huang, H. Luo, X. Zhou, C. Gu, and B. Liu, "Diffusion dynamics of valley excitons by transient grating spectroscopy in monolayer WSe2", Applied Physics Letters **115**, 131902 (2019) (cit. on pp. 37, 86, 90).

[148]D. Snoke, "Predicting the ionization threshold for carriers in excited semiconductors", Solid State Communications **146**, 73–77 (2008) (cit. on pp. 38, 88).

[149]A. Chernikov, C. Ruppert, H. M. Hill, A. F. Rigosi, and T. F. Heinz, "Population inversion and giant bandgap renormalization in atomically thin WS2 layers", Nature Photonics **9**, 466–470 (2015) (cit. on p. 38).

[150]A. Steinhoff, M. Florian, M. Rösner, G. Schönhoff, T. O. Wehling, and F. Jahnke, "Exciton fission in monolayer transition metal dichalcogenide semiconductors", Nature Communications **8**, 10.1038/s41467-017-01298-6 (2017) (cit. on pp. 38–40, 88).

[151]J. Shah, M. Combescot, and A. H. Dayem, "Investigation of Exciton-Plasma Mott Transition in Si", Physical Review Letters **38**, 1497–1500 (1977) (cit. on p. 38).

[152]J. Mock, G. Thomas, and M. Combescot, "Entropy ionization of an exciton gas", Solid State Communications **25**, 279–282 (1978) (cit. on p. 38).

[153]J. Zipfel, M. Kulig, R. Perea-Causıén, S. Brem, J. D. Ziegler, R. Rosati, T. Taniguchi, K. Watanabe, M. M. Glazov, E. Malic, et al., "Exciton diffusion in monolayer semiconductors with suppressed disorder", arXiv preprint arXiv:1911.02909 (2019) (cit. on pp. 38–39, 88, 90, 94, 96, 106).

[154]M. Selig, G. Berghäuser, A. Raja, P. Nagler, C. SchÃ¼ller, T. F. Heinz, T. Korn, A. Chernikov, E. Malic, and A. Knorr, "Excitonic linewidth and coherence lifetime in monolayer transition metal dichalcogenides", Nature Communications **7**, 10.1038/ncomms13279 (2016) (cit. on pp. 41, 61, 92).

[155]A. Kojima, K. Teshima, Y. Shirai, and T. Miyasaka, "Organometal halide perovskites as visible-light sensitizers for photovoltaic cells", Journal of the American Chemical Society **131**, 6050–6051 (2009) (cit. on p. 42).

[156]M. M. Lee, J. Teuscher, T. Miyasaka, T. N. Murakami, and H. J. Snaith, "Efficient hybrid solar cells based on meso-superstructured organometal halide perovskites", Science **338**, 643–647 (2012) (cit. on p. 42).

[157]J.-P. Correa-Baena, M. Saliba, T. Buonassisi, M. Grätzel, A. Abate, W. Tress, and A. Hagfeldt, "Promises and challenges of perovskite solar cells", Science **358**, 739–744 (2017) (cit. on pp. 42, 44, 51, 111).

[158]H. J. Snaith, "Present status and future prospects of perovskite photovoltaics", Nature materials **17**, 372–376 (2018) (cit. on p. 42).

[159]M. Saliba, T. Matsui, K. Domanski, J.-Y. Seo, A. Ummadisingu, S. M. Zakeeruddin, J.-P. Correa-Baena, W. R. Tress, A. Abate, A. Hagfeldt, et al., "Incorporation of rubidium cations into perovskite solar cells improves photovoltaic performance", Science **354**, 206–209 (2016) (cit. on p. 42).

[160]W. S. Yang, B.-W. Park, E. H. Jung, N. J. Jeon, Y. C. Kim, D. U. Lee, S. S. Shin, J. Seo, E. K. Kim, J. H. Noh, et al., "Iodide management in formamidinium-lead-halide–based perovskite layers for efficient solar cells", Science **356**, 1376–1379 (2017) (cit. on p. 42).

[161]H. Tsai, R. Asadpour, J.-C. Blancon, C. C. Stoumpos, O. Durand, J. W. Strzalka, B. Chen, R. Verduzco, P. M. Ajayan, S. Tretiak, et al., "Light-induced lattice expansion leads to high-efficiency perovskite solar cells", Science **360**, 67–70 (2018) (cit. on p. 42).

[162]D. H. Cao, C. C. Stoumpos, O. K. Farha, J. T. Hupp, and M. G. Kanatzidis, "2D Homologous Perovskites as Light-Absorbing Materials for Solar Cell Applications", Journal of the American Chemical Society **137**, 7843–7850 (2015) (cit. on p. 42).

[163]J. Zhang, X. Yang, H. Deng, K. Qiao, U. Farooq, M. Ishaq, F. Yi, H. Liu, J. Tang, and H. Song, "Low-Dimensional Halide Perovskites and Their Advanced Optoelectronic Applications", Nano-Micro Letters **9**, 10.1007/s40820-017-0137-5 (2017) (cit. on p. 42).

[164]T. Ishihara, J. Takahashi, and T. Goto, "Exciton state in two-dimensional perovskite semiconductor (C10H21NH3)2PbI4", Solid State Communications **69**, 933–936 (1989) (cit. on pp. 42, 44–45).

[165]E. A. Muljarov, S. G. Tikhodeev, N. A. Gippius, and T. Ishihara, "Excitons in self-organized semiconductor/insulator superlattices: PbI-based perovskite compounds", Physical Review B **51**, 14370–14378 (1995) (cit. on pp. 42, 45).

[166]I. Koutselas, L. Ducasse, and G. C. Papavassiliou, "Electronic properties of three- and low-dimensional semiconducting materials with Pb halide and Sn halide units", Journal of Physics: Condensed Matter **8**, 1217 (1996) (cit. on pp. 42, 45).

[167]H. Tsai, W. Nie, J.-C. Blancon, C. C. Stoumpos, R. Asadpour, B. Harutyunyan, A. J. Neukirch, R. Verduzco, J. J. Crochet, S. Tretiak, L. Pedesseau, J. Even, M. A. Alam, G. Gupta, J. Lou, P. M. Ajayan, M. J. Bedzyk, M. G. Kanatzidis, and A. D. Mohite, "High-efficiency two-dimensional Ruddlesden–Popper perovskite solar cells", Nature **536**, 312–316 (2016) (cit. on pp. 42, 112).

[168]J.-C. Blancon, H. Tsai, W. Nie, C. C. Stoumpos, L. Pedesseau, C. Katan, M. Kepenekian, C. M. M. Soe, K. Appavoo, M. Y. Sfeir, S. Tretiak, P. M. Ajayan, M. G. Kanatzidis, J. Even, J. J. Crochet, and A. D. Mohite, "Extremely efficient internal exciton dissociation through edge states in layered 2D perovskites", Science **355**, 1288–1292 (2017) (cit. on pp. 42, 112).

[169]H.-C. Cheng, G. Wang, D. Li, Q. He, A. Yin, Y. Liu, H. Wu, M. Ding, Y. Huang, and X. Duan, "van der Waals Heterojunction Devices Based on Organohalide Perovskites and Two-Dimensional Materials", Nano Letters **16**, 367–373 (2015) (cit. on p. 42).

[170]K. Leng, I. Abdelwahab, I. Verzhbitskiy, M. Telychko, L. Chu, W. Fu, X. Chi, N. Guo, Z. Chen, Z. Chen, C. Zhang, Q.-H. Xu, J. Lu, M. Chhowalla, G. Eda, and K. P. Loh, "Molecularly thin two-dimensional hybrid perovskites with tunable optoelectronic properties due to reversible surface relaxation", Nature Materials **17**, 908–914 (2018) (cit. on p. 42).

[171]M. Seitz, P. Gant, A. Castellanos-Gomez, and F. Prins, "Long-Term Stabilization of Two-Dimensional Perovskites by Encapsulation with Hexagonal Boron Nitride", Nanomaterials **9**, 1120 (2019) (cit. on pp. 42, 112).

[172]J. Holler, L. Bauriedl, T. Korn, A. Seitz, F. Özyigit, M. Eichinger, C. Schüller, K. Watanabe, T. Taniguchi, C. Strunk, et al., "Air tightness of hBN encapsulation and its impact on Raman spectroscopy of van der Waals materials", 2D Materials **7**, 015012 (2019) (cit. on pp. 42, 112).

[173]D. B. Mitzi, K. Chondroudis, and C. R. Kagan, "Organic-inorganic electronics", IBM Journal of Research and Development **45**, 29–45 (2001) (cit. on pp. 42, 44).

[174]W.-J. Yin, J.-H. Yang, J. Kang, Y. Yan, and S.-H. Wei, "Halide perovskite materials for solar cells: a theoretical review", Journal of Materials Chemistry A **3**, 8926–8942 (2015) (cit. on p. 42).

[175]C. Katan, N. Mercier, and J. Even, "Quantum and Dielectric Confinement Effects in Lower-Dimensional Hybrid Perovskite Semiconductors", Chemical Reviews **119**, 3140–3192 (2019) (cit. on pp. 43–45, 117).

[176]D. B. Mitzi, "Synthesis, structure, and properties of organic-inorganic perovskites and related materials", Progress in inorganic chemistry, 1–121 (1999) (cit. on pp. 43–44).

[177]D. B. Mitzi, "Templating and structural engineering in organic–inorganic perovskites", Journal of the Chemical Society, Dalton Transactions, 1–12 (2001) (cit. on p. 43).

[178]E. G. Tulsky and J. R. Long, "Dimensional Reduction: A Practical Formalism for Manipulating Solid Structures", Chemistry of Materials **13**, 1149–1166 (2001) (cit. on p. 43).

[179]M. Yang, Y. Zhou, Y. Zeng, C.-S. Jiang, N. P. Padture, and K. Zhu, "Square-Centimeter Solution-Processed Planar CH3NH3PbI3Perovskite Solar Cells with Efficiency Exceeding 15%", Advanced Materials **27**, 6363–6370 (2015) (cit. on p. 44).

[180]H. Zhu, Y. Fu, F. Meng, X. Wu, Z. Gong, Q. Ding, M. V. Gustafsson, M. T. Trinh, S. Jin, and X.-Y. Zhu, "Lead halide perovskite nanowire lasers with low lasing thresholds and high quality factors", Nature Materials **14**, 636–642 (2015) (cit. on p. 44).

[181]W. Rehman, D. P. McMeekin, J. B. Patel, R. L. Milot, M. B. Johnston, H. J. Snaith, and L. M. Herz, "Photovoltaic mixed-cation lead mixed-halide perovskites: links between crystallinity, photo-stability and electronic properties", Energy & Environmental Science **10**, 361–369 (2017) (cit. on p. 44).

[182]D. A. Egger, A. Bera, D. Cahen, G. Hodes, T. Kirchartz, L. Kronik, R. Lovrincic, A. M. Rappe, D. R. Reichman, and O. Yaffe, "What Remains Unexplained about the Properties of Halide Perovskites?", Advanced Materials **30**, 1800691 (2018) (cit. on pp. 44–45, 116).

[183]S. Sun, Y. Fang, G. Kieslich, T. J. White, and A. K. Cheetham, "Mechanical properties of organic–inorganic halide perovskites, CH3NH3PbX3(X = I, Br and Cl), by nanoindentation", Journal of Materials Chemistry A **3**, 18450–18455 (2015) (cit. on pp. 44, 116).

[184]Y. Rakita, S. R. Cohen, N. K. Kedem, G. Hodes, and D. Cahen, "Mechanical properties of APbX3 (A = Cs or CH3NH3; X = I or Br) perovskite single crystals", MRS Communications **5**, 623–629 (2015) (cit. on pp. 44, 116).

[185]A. Létoublon, S. Paofai, B. Rufflé, P. Bourges, B. Hehlen, T. Michel, C. Ecolivet, O. Durand, S. Cordier, C. Katan, and J. Even, "Elastic Constants, Optical Phonons, and Molecular Relaxations in the High Temperature Plastic Phase of the CH3NH3PbBr3 Hybrid Perovskite", The Journal of Physical Chemistry Letters **7**, 3776–3784 (2016) (cit. on pp. 44, 116).

[186]O. Yaffe, Y. Guo, L. Z. Tan, D. A. Egger, T. Hull, C. C. Stoumpos, F. Zheng, T. F. Heinz, L. Kronik, M. G. Kanatzidis, J. S. Owen, A. M. Rappe, M. A. Pimenta, and L. E. Brus, "Local Polar Fluctuations in Lead Halide Perovskite Crystals", Physical Review Letters **118**, 10.1103/physrevlett.118.136001 (2017) (cit. on pp. 44, 116).

[187]D. G. Billing and A. Lemmerer, "Synthesis, characterization and phase transitions of the inorganic–organic layered perovskite-type hybrids [(CnH2n+1NH3)2PbI4] (n = 12, 14, 16 and 18)", New Journal of Chemistry **32**, 1736 (2008) (cit. on pp. 44, 51, 113).

[188]J. Even, L. Pedesseau, and C. Katan, "Understanding Quantum Confinement of Charge Carriers in Layered 2D Hybrid Perovskites", ChemPhysChem **15**, 3733–3741 (2014) (cit. on pp. 44–45, 113).

[189]O. Yaffe, A. Chernikov, Z. M. Norman, Y. Zhong, A. Velauthapillai, A. van der Zande, J. S. Owen, and T. F. Heinz, "Excitons in ultrathin organic-inorganic perovskite crystals", Physical Review B **92**, 10.1103/physrevb.92.045414 (2015) (cit. on pp. 44, 46, 112–113).

[190]B. Conings, J. Drijkoningen, N. Gauquelin, A. Babayigit, J. D'Haen, L. D'Olieslaeger, A. Ethirajan, J. Verbeeck, J. Manca, E. Mosconi, F. D. Angelis, and H.-G. Boyen, "Intrinsic Thermal Instability of Methylammonium Lead Trihalide Perovskite", Advanced Energy Materials **5**, 1500477 (2015) (cit. on pp. 44, 51, 111).

[191]M. C. Gelvéz-Rueda, E. M. Hutter, D. H. Cao, N. Renaud, C. C. Stoumpos, J. T. Hupp, T. J. Savenije, M. G. Kanatzidis, and F. C. Grozema, "Interconversion between free charges and bound excitons in 2D hybrid lead halide perovskites", The Journal of Physical Chemistry C **121**, 26566–26574 (2017) (cit. on pp. 44, 51, 111).

[192]C. C. Boyd, R. Cheacharoen, T. Leijtens, and M. D. McGehee, "Understanding Degradation Mechanisms and Improving Stability of Perovskite Photovoltaics", Chemical Reviews **119**, 3418–3451 (2018) (cit. on pp. 44, 51, 111).

[193]G. Papavassiliou, A. Patsis, D. Lagouvardos, and I. Koutselas, "Spectroscopic studies of (C10H21NH3)2PbI4, (CH3NH3)(C10H21NH3)2Pb2I7, (CH3NH3) PbI3, and similar compounds", Synthetic Metals **57**, 3889–3894 (1993) (cit. on p. 44).

[194]G. Papavassiliou, I. Koutselas, A. Terzis, and M.-H. Whangbo, "Structural and electronic properties of the natural quantum-well system (C6H5CH2CH2NH3)2SnI4", Solid State Communications **91**, 695–698 (1994) (cit. on pp. 44–45).

[195]T. Umebayashi, K. Asai, T. Kondo, and A. Nakao, "Electronic structures of lead iodide based low-dimensional crystals", Physical Review B **67**, 10.1103/physrevb.67.155405 (2003) (cit. on pp. 44–45).

[196]J. Even, L. Pedesseau, M.-A. Dupertuis, J.-M. Jancu, and C. Katan, "Electronic model for self-assembled hybrid organic/perovskite semiconductors: Reverse band edge electronic states ordering and spin-orbit coupling", Physical Review B **86**, 10.1103/physrevb.86.205301 (2012) (cit. on p. 44).

[197]J. Even, L. Pedesseau, J.-M. Jancu, and C. Katan, "Importance of Spin–Orbit Coupling in Hybrid Organic/Inorganic Perovskites for Photovoltaic Applications", The Journal of Physical Chemistry Letters **4**, 2999–3005 (2013) (cit. on p. 44).

[198]C. Quarti, N. Marchal, and D. Beljonne, "Tuning the Optoelectronic Properties of Two-Dimensional Hybrid Perovskite Semiconductors with Alkyl Chain Spacers", The Journal of Physical Chemistry Letters **9**, 3416–3424 (2018) (cit. on pp. 44–45).

[199]G. Giorgi, K. Yamashita, and M. Palummo, "Nature of the Electronic and Optical Excitations of Ruddlesden-Popper Hybrid Organic-Inorganic Perovskites: The Role of the Many-Body Interactions", The Journal of Physical Chemistry Letters **9**, 5891–5896 (2018) (cit. on p. 44).

[200]J. Kang and L.-W. Wang, "Dynamic Disorder and Potential Fluctuation in Two-Dimensional Perovskite", The Journal of Physical Chemistry Letters **8**, 3875–3880 (2017) (cit. on p. 44).

[201]S. Silver, J. Yin, H. Li, J.-L. Brédas, and A. Kahn, "Characterization of the Valence and Conduction Band Levels of n = 1 2D Perovskites: A Combined Experimental and Theoretical Investigation", Advanced Energy Materials **8**, 1703468 (2018) (cit. on p. 44).

[202]L. Zhou, A. J. Neukirch, D. J. Vogel, D. S. Kilin, L. Pedesseau, M. A. Carignano, A. D. Mohite, J. Even, C. Katan, and S. Tretiak, "Density of States Broadening in CH3NH3PbI3 Hybrid Perovskites Understood from ab Initio Molecular Dynamics Simulations", ACS Energy Letters **3**, 787–793 (2018) (cit. on p. 44).

[203]A. Amat, E. Mosconi, E. Ronca, C. Quarti, P. Umari, M. K. Nazeeruddin, M. GrÃ¤tzel, and F. D. Angelis, "Cation-Induced Band-Gap Tuning in Organohalide Perovskites: Interplay of Spin-Orbit Coupling and Octahedra Tilting", Nano Letters **14**, 3608–3616 (2014) (cit. on p. 44).

[204]B. Traore, L. Pedesseau, L. Assam, X. Che, J.-C. Blancon, H. Tsai, W. Nie, C. C. Stoumpos, M. G. Kanatzidis, S. Tretiak, A. D. Mohite, J. Even, M. Kepenekian, and C. Katan, "Composite Nature of Layered Hybrid Perovskites: Assessment on Quantum and Dielectric Confinements and Band Alignment", ACS Nano **12**, 3321–3332 (2018) (cit. on p. 45).

[205]C. Quarti, E. Mosconi, and F. D. Angelis, "Interplay of Orientational Order and Electronic Structure in Methylammonium Lead Iodide: Implications for Solar Cell Operation", Chemistry of Materials **26**, 6557–6569 (2014) (cit. on p. 45).

[206]J. L. Knutson, J. D. Martin, and D. B. Mitzi, "Tuning the Band Gap in Hybrid Tin Iodide Perovskite Semiconductors Using Structural Templating", Inorganic Chemistry **44**, 4699–4705 (2005) (cit. on p. 45).

[207]M. R. Filip, G. E. Eperon, H. J. Snaith, and F. Giustino, "Steric engineering of metal-halide perovskites with tunable optical band gaps", Nature Communications **5**, 10.1038/ncomms6757 (2014) (cit. on pp. 45, 116).

[208]Y. Guo, O. Yaffe, T. D. Hull, J. S. Owen, D. R. Reichman, and L. E. Brus, "Dynamic emission Stokes shift and liquid-like dielectric solvation of band edge carriers in lead-halide perovskites", Nature Communications **10**, 10.1038/s41467-019-09057-5 (2019) (cit. on p. 45).

[209]T. Ishihara, X. Hong, J. Ding, and A. Nurmikko, "Dielectric confinement effect for exciton and biexciton states in PbI4-based two-dimensional semiconductor structures", Surface Science **267**, 323–326 (1992) (cit. on p. 46).

[210]J.-C. Blancon, A. V. Stier, H. Tsai, W. Nie, C. C. Stoumpos, B. Traoré, L. Pedesseau, M. Kepenekian, F. Katsutani, G. T. Noe, J. Kono, S. Tretiak, S. A. Crooker, C. Katan, M. G. Kanatzidis, J. J. Crochet, J. Even, and A. D. Mohite, "Scaling law for excitons in 2D perovskite quantum wells", Nature Communications **9**, 10.1038/s41467-018-04659-x (2018) (cit. on pp. 46, 117).

[211]K. Tanaka, F. Sano, T. Takahashi, T. Kondo, R. Ito, and K. Ema, "Two-dimensional Wannier excitons in a layered-perovskite-type crystal (C6H13NH3)2PbI4", Solid State Communications **122**, 249–252 (2002) (cit. on p. 46).

[212]M. M. Benameur, B. Radisavljevic, J. S. Héron, S. Sahoo, H. Berger, and A. Kis, "Visibility of dichalcogenide nanolayers", Nanotechnology **22**, 125706 (2011) (cit. on p. 48).

[213]Y. Huang, E. Sutter, N. N. Shi, J. Zheng, T. Yang, D. Englund, H.-J. Gao, and P. Sutter, "Reliable Exfoliation of Large-Area High-Quality Flakes of Graphene and Other Two-Dimensional Materials", ACS Nano **9**, 10612–10620 (2015) (cit. on p. 49).

[214]C. R. Dean, A. F. Young, I. Meric, C. Lee, L. Wang, S. Sorgenfrei, K. Watanabe, T. Taniguchi, P. Kim, K. L. Shepard, and J. Hone, "Boron nitride substrates for high-quality graphene electronics", Nature Nanotechnology **5**, 722–726 (2010) (cit. on pp. 49, 73, 76).

[215]M. K. L. Man, S. Deckoff-Jones, A. Winchester, G. Shi, G. Gupta, A. D. Mohite, S. Kar, E. Kioupakis, S. Talapatra, and K. M. Dani, "Protecting the properties of monolayer MoS2 on silicon based substrates with an atomically thin buffer", Scientific Reports **6**, 10.1038/srep20890 (2016) (cit. on pp. 49, 73, 76).

[216]F. Cadiz, E. Courtade, C. Robert, G. Wang, Y. Shen, H. Cai, T. Taniguchi, K. Watanabe, H. Carrere, D. Lagarde, et al., "Excitonic Linewidth Approaching the Homogeneous Limit in MoS 2-Based van der Waals Heterostructures", Physical Review X **7**, 021026 (2017) (cit. on p. 49).

[217]E. J. Juarez-Perez, L. K. Ono, M. Maeda, Y. Jiang, Z. Hawash, and Y. Qi, "Photodecomposition and thermal decomposition in methylammonium halide lead perovskites and inferred design principles to increase photovoltaic device stability", Journal of Materials Chemistry A **6**, 9604–9612 (2018) (cit. on pp. 51, 112).

[218]S. J. Byrnes, "Multilayer optical calculations", arXiv preprint arXiv:1603.02720 (2016) (cit. on pp. 56–59).

[219]J. Frenkel, "On the transformation of light into heat in solids. i", Physical Review **37**, 17–44 (1931) (cit. on p. 63).

[220]M. Knupfer, "Exciton binding energies in organic semiconductors", Applied Physics A **77**, 623–626 (2003) (cit. on p. 63).

[221]C. J. Bardeen, "The Structure and Dynamics of Molecular Excitons", Annual Review of Physical Chemistry **65**, 127–148 (2014) (cit. on p. 63).

[222]M. Manca, M. M. Glazov, C. Robert, F. Cadiz, T. Taniguchi, K. Watanabe, E. Courtade, T. Amand, P. Renucci, X. Marie, G. Wang, and B. Urbaszek, "Enabling valley selective exciton scattering in monolayer WSe2 through upconversion", Nature Communications **8**, 14927 (2017) (cit. on p. 64).

[223]E. Liu, J. van Baren, T. Taniguchi, K. Watanabe, Y.-C. Chang, and C. H. Lui, "Magnetophotoluminescence of exciton Rydberg states in monolayer WSe2", Physical Review B **99**, 10.1103/physrevb.99.205420 (2019) (cit. on p. 65).

[224]C. Jin, J. Kim, J. Suh, Z. Shi, B. Chen, X. Fan, M. Kam, K. Watanabe, T. Taniguchi, S. Tongay, et al., "Interlayer electron–phonon coupling in WSe 2/hBN heterostructures", Nature Physics **13**, 127 (2017) (cit. on p. 66).

[225]A. V. Stier, N. P. Wilson, G. Clark, X. Xu, and S. A. Crooker, "Probing the influence of dielectric environment on excitons in monolayer WSe2: insight from high magnetic fields", Nano Letters **16**, 7054–7060 (2016) (cit. on p. 68).

[226]P. J. Gielisse, S. S. Mitra, J. N. Plendl, R. D. Griffis, L. C. Mansur, R. Marshall, and E. A. Pascoe, "Lattice Infrared Spectra of Boron Nitride and Boron Monophosphide", Physical Review **155**, 1039–1046 (1967) (cit. on p. 70).

[227]J. Quereda, A. Castellanos-Gomez, N. Agraït, and G. Rubio-Bollinger, "Single-layer MoS2 roughness and sliding friction quenching by interaction with atomically flat substrates", Applied Physics Letters **105**, 053111 (2014) (cit. on pp. 73, 76).

[228]M. R. Rosenberger, H.-J. Chuang, K. M. McCreary, A. T. Hanbicki, S. V. Sivaram, and B. T. Jonker, "Nano-"Squeegee" for the Creation of Clean 2D Material Interfaces", ACS Applied Materials & Interfaces **10**, 10379–10387 (2018) (cit. on p. 73).

[229]H. J. Conley, B. Wang, J. I. Ziegler, R. F. Haglund, S. T. Pantelides, and K. I. Bolotin, "Bandgap Engineering of Strained Monolayer and Bilayer MoS2", Nano Letters **13**, 3626–3630 (2013) (cit. on p. 82).

[230]R. Roldán, A. Castellanos-Gomez, E. Cappelluti, and F. Guinea, "Strain engineering in semiconducting two-dimensional crystals", Journal of Physics: Condensed Matter **27**, 313201 (2015) (cit. on p. 82).

[231]X. He, H. Li, Z. Zhu, Z. Dai, Y. Yang, P. Yang, Q. Zhang, P. Li, U. Schwingenschlogl, and X. Zhang, "Strain engineering in monolayer WS2, MoS2, and the WS2/MoS2 heterostructure", Applied Physics Letters **109**, 173105 (2016) (cit. on p. 82).

[232]R. Frisenda, M. DrÃ¼ppel, R. Schmidt, S. M. de Vasconcellos, D. P. de Lara, R. Bratschitsch, M. Rohlfing, and A. Castellanos-Gomez, "Biaxial strain tuning of the optical properties of single-layer transition metal dichalcogenides", npj 2D Materials and Applications **1**, 10.1038/s41699-017-0013-7 (2017) (cit. on p. 82).

[233]M. Feierabend, A. Morlet, G. BerghÃ¤user, and E. Malic, "Impact of strain on the optical fingerprint of monolayer transition-metal dichalcogenides", Physical Review B **96**, 10.1103/physrevb.96.045425 (2017) (cit. on p. 82).

[234]I. Niehues, R. Schmidt, M. DrÃ¼ppel, P. Marauhn, D. Christiansen, M. Selig, G. BerghÃ¤user, D. Wigger, R. Schneider, L. Braasch, R. Koch, A. Castellanos-Gomez, T. Kuhn, A. Knorr, E. Malic, M. Rohlfing, S. M. de Vasconcellos, and R. Bratschitsch, "Strain Control of Exciton–Phonon Coupling in Atomically Thin Semiconductors", Nano Letters **18**, 1751–1757 (2018) (cit. on p. 82).

[235]P. Back, M. Sidler, O. Cotlet, A. Srivastava, N. Takemura, M. Kroner, and A. Imamoğlu, "Giant Paramagnetism-Induced Valley Polarization of Electrons in Charge-Tunable Monolayer MoSe2", Physical Review Letters **118**, 10.1103/physrevlett.118.237404 (2017) (cit. on p. 82).

[236]Y. Wang, C. Cong, W. Yang, J. Shang, N. Peimyoo, Y. Chen, J. Kang, J. Wang, W. Huang, and T. Yu, "Strain-induced direct–indirect bandgap transition and phonon modulation in monolayer WS2", Nano Research **8**, 2562–2572 (2015) (cit. on p. 82).

[237]B. G. Shin, G. H. Han, S. J. Yun, H. M. Oh, J. J. Bae, Y. J. Song, C.-Y. Park, and Y. H. Lee, "Indirect Bandgap Puddles in Monolayer MoS2by Substrate-Induced Local Strain", Advanced Materials **28**, 9378–9384 (2016) (cit. on p. 82).

[238]D. Lloyd, X. Liu, J. W. Christopher, L. Cantley, A. Wadehra, B. L. Kim, B. B. Goldberg, A. K. Swan, and J. S. Bunch, "Band Gap Engineering with Ultralarge Biaxial Strains in Suspended Monolayer MoS2", Nano Letters **16**, 5836–5841 (2016) (cit. on p. 82).

[239]O. B. Aslan, M. Deng, and T. F. Heinz, "Strain tuning of excitons in monolayer WSe2", Physical Review B **98**, 10.1103/physrevb.98.115308 (2018) (cit. on p. 82).

[240]O. B. Aslan, I. M. Datye, M. J. Mleczko, K. S. Cheung, S. Krylyuk, A. Bruma, I. Kalish, A. V. Davydov, E. Pop, and T. F. Heinz, "Probing the Optical Properties and Strain-Tuning of Ultrathin Mo1–xWxTe2", Nano Letters **18**, 2485–2491 (2018) (cit. on p. 82).

[241]M. Sidler, P. Back, O. Cotlet, A. Srivastava, T. Fink, M. Kroner, E. Demler, and A. Imamoglu, "Fermi polaron-polaritons in charge-tunable atomically thin semiconductors", Nature Physics **13**, 255–261 (2016) (cit. on p. 83).

[242]L. M. Smith, D. R. Wake, J. P. Wolfe, D. Levi, M. V. Klein, J. Klem, T. Henderson, and H. Morkoç, "Picosecond imaging of photoexcited carriers in quantum wells: Anomalous lateral confinement at high densities", Physical Review B **38**, 5788–5791 (1988) (cit. on p. 86).

[243]L. Yuan, T. Wang, T. Zhu, M. Zhou, and L. Huang, "Exciton Dynamics, Transport, and Annihilation in Atomically Thin Two-Dimensional Semiconductors", The Journal of Physical Chemistry Letters **8**, 3371–3379 (2017) (cit. on p. 86).

[244]D. F. C. Leon, Z. Li, S. W. Jang, C.-H. Cheng, and P. B. Deotare, "Exciton transport in strained monolayer WSe2", Applied Physics Letters **113**, 252101 (2018) (cit. on p. 86).

[245]V. Shahnazaryan, O. Kyriienko, and H. Rostami, "Exciton routing in the heterostructure of a transition metal dichalcogenide monolayer on a paraelectric substrate", Physical Review B **100**, 10.1103/physrevb.100.165303 (2019) (cit. on p. 86).

[246]S. Hao, M. Z. Bellus, D. He, Y. Wang, and H. Zhao, "Controlling exciton transport in monolayer MoSe2 by dielectric screening", Nanoscale Horizons **5**, 139–143 (2020) (cit. on p. 86).

[247]M. M. Glazov, "Phonon wind and drag of excitons in monolayer semiconductors", Physical Review B **100**, 10.1103/physrevb.100.045426 (2019) (cit. on pp. 86, 121).

[248]R. Perea-Causıén, S. Brem, R. Rosati, R. Jago, M. Kulig, J. D. Ziegler, J. Zipfel, A. Chernikov, and E. Malic, "Exciton Propagation and Halo Formation in Two-Dimensional Materials", Nano Letters **19**, 7317–7323 (2019) (cit. on p. 86).

[249]L. Yuan, B. Zheng, J. Kunstmann, T. Brumme, A. B. Kuc, C. Ma, S. Deng, D. Blach, A. Pan, and L. Huang, "Anomalous Interlayer Exciton Diffusion in Twist-Angle-Dependent Moiré Potentials of WS2-WSe2 Heterobilayers", arXiv preprint arXiv:1910.02869 (2019) (cit. on p. 86).

[250]Y. Hoshi, T. Kuroda, M. Okada, R. Moriya, S. Masubuchi, K. Watanabe, T. Taniguchi, R. Kitaura, and T. Machida, "Suppression of exciton-exciton annihilation in tungsten disulfide monolayers encapsulated by hexagonal boron nitrides", Physical Review B **95**, 10.1103/physrevb.95.241403 (2017) (cit. on p. 88).

[251]M. Selig, G. Berghäuser, M. Richter, R. Bratschitsch, A. Knorr, and E. Malic, "Dark and bright exciton formation, thermalization, and photoluminescence in monolayer transition metal dichalcogenides", 2D Materials **5**, 035017 (2018) (cit. on pp. 90, 93, 109).

[252]Y. Song and H. Dery, "Transport theory of monolayer transition-metal dichalcogenides through symmetry", Physical review letters **111**, 026601 (2013) (cit. on p. 92).

[253]Z. Jin, X. Li, J. T. Mullen, and K. W. Kim, "Intrinsic transport properties of electrons and holes in monolayer transition-metal dichalcogenides", Physical Review B **90**, 10.1103/physrevb.90.045422 (2014) (cit. on pp. 92–94).

[254]R. Rosati, R. Perea-Causıén, S. Brem, and E. Malic, "Negative effective excitonic diffusion in monolayer transition metal dichalcogenides", Nanoscale **12**, 356–363 (2019) (cit. on pp. 92–93).

[255]S. Chatterjee, C. Ell, S. Mosor, G. Khitrova, H. M. Gibbs, W. Hoyer, M. Kira, S. W. Koch, J. P. Prineas, and H. Stolz, "Excitonic Photoluminescence in Semiconductor Quantum Wells: Plasma versus Excitons", Physical Review Letters **92**, 10.1103/physrevlett.92.067402 (2004) (cit. on p. 98).

[256]Z. Li, T. Wang, C. Jin, Z. Lu, Z. Lian, Y. Meng, M. Blei, S. Gao, T. Taniguchi, K. Watanabe, T. Ren, S. Tongay, L. Yang, D. Smirnov, T. Cao, and S.-F. Shi, "Emerging photoluminescence from the dark-exciton phonon replica in monolayer WSe2", Nature Communications **10**, 10.1038/s41467-019-10477-6 (2019) (cit. on pp. 100, 103).

[257]E. Liu, J. van Baren, T. Taniguchi, K. Watanabe, Y.-C. Chang, and C. H. Lui, "Valley-selective chiral phonon replicas of dark excitons and trions in monolayer WSe2", Physical Review Research **1**, 10.1103/physrevresearch.1.032007 (2019) (cit. on pp. 100, 103).

[258]S. Brem, A. Ekman, D. Christiansen, F. Katsch, M. Selig, C. Robert, X. Marie, B. Urbaszek, A. Knorr, and E. Malic, "Phonon-assisted Photoluminescence from Dark Excitons in Monolayers of Transition Metal Dichalcogenides", arXiv preprint arXiv:1904.04711 (2019) (cit. on p. 102).

[259]T. Feldtmann, M. Kira, and S. W. Koch, "Phonon sidebands in semiconductor luminescence", physica status solidi (b) **246**, 332–336 (2009) (cit. on p. 104).

[260]D. Christiansen, M. Selig, G. Berghäuser, R. Schmidt, I. Niehues, R. Schneider, A. Arora, S. M. de Vasconcellos, R. Bratschitsch, E. Malic, and A. Knorr, "Phonon Sidebands in Monolayer Transition Metal Dichalcogenides", Physical Review Letters **119**, 10.1103/physrevlett.119.187402 (2017) (cit. on p. 104).

[261]C. Ataca, H. Şahin, and S. Ciraci, "Stable, Single-Layer MX2 Transition-Metal Oxides and Dichalcogenides in a Honeycomb-Like Structure", The Journal of Physical Chemistry C **116**, 8983–8999 (2012) (cit. on p. 104).

[262]A. Berkdemir, H. R. Gutiérrez, A. R. Botello-Méndez, N. Perea-López, A. L. Elıéas, C.-I. Chia, B. Wang, V. H. Crespi, F. López-Urıéas, J.-C. Charlier, H. Terrones, and M. Terrones, "Identification of individual and few layers of WS2 using Raman Spectroscopy", Scientific Reports **3**, 10.1038/srep01755 (2013) (cit. on p. 104).

[263]A. Sengupta, A. Chanana, and S. Mahapatra, "Phonon scattering limited performance of monolayer MoS2 and WSe2 n-MOSFET", AIP Advances **5**, 027101 (2015) (cit. on p. 104).

[264]H. Sahin, S. Tongay, S. Horzum, W. Fan, J. Zhou, J. Li, J. Wu, and F. M. Peeters, "Anomalous Raman spectra and thickness-dependent electronic properties of WSe2", Physical Review B **87**, 10.1103/physrevb.87.165409 (2013) (cit. on p. 104).

[265]M. He, P. Rivera, D. V. Tuan, N. P. Wilson, M. Yang, T. Taniguchi, K. Watanabe, J. Yan, D. G. Mandrus, H. Yu, H. Dery, W. Yao, and X. Xu, "Valley phonons and exciton complexes in a monolayer semiconductor", Nature Communications **11**, 10.1038/s41467-020-14472-0 (2020) (cit. on p. 105).

[266]D. Karaiskaj, M. Thewalt, T. Ruf, M. Cardona, H.-J. Pohl, G. Deviatych, P. Sennikov, and H. Riemann, "Photoluminescence of Isotopically Purified Silicon: How Sharp are Bound Exciton Transitions?", Physical Review Letters **86**, 6010–6013 (2001) (cit. on p. 105).

[267]M. M. Glazov, "Quantum interference effect on exciton transport in monolayer semiconductors", (2019) (cit. on p. 110).

[268]S. Deng, E. Shi, L. Yuan, L. Jin, L. Dou, and L. Huang, "Long-range exciton transport and slow annihilation in two-dimensional hybrid perovskites", Nature Communications **11**, 10.1038/s41467-020-14403-z (2020) (cit. on p. 111).

[269]S. Ruan, M.-A. Surmiak, Y. Ruan, D. P. McMeekin, H. Ebendorff-Heidepriem, Y.-B. Cheng, J. Lu, and C. R. McNeill, "Light induced degradation in mixed-halide perovskites", Journal of Materials Chemistry C **7**, 9326–9334 (2019) (cit. on p. 112).

[270]K. Abdel-Baki, F. Boitier, H. Diab, G. Lanty, K. Jemli, F. Lédée, D. Garrot, E. Deleporte, and J. S. Lauret, "Exciton dynamics and non-linearities in 2D-hybrid organic perovskites", 10.1063/1.4941345 (2015) (cit. on p. 114).

[271]X. Wu, M. T. Trinh, D. Niesner, H. Zhu, Z. Norman, J. S. Owen, O. Yaffe, B. J. Kudisch, and X.-Y. Zhu, "Trap States in Lead Iodide Perovskites", Journal of the American Chemical Society **137**, 2089–2096 (2015) (cit. on p. 114).

[272]M. van Schilfgaarde, T. Kotani, and S. Faleev, "Quasiparticle Self-ConsistentGWTheory", Physical Review Letters **96**, 10 . 1103 / physrevlett . 96.226402 (2006) (cit. on p. 117).

[273]J. Even, L. Pedesseau, J.-M. Jancu, and C. Katan, "DFT and k·p modelling of the phase transitions of lead and tin halide perovskites for photovoltaic cells", physica status solidi (RRL) - Rapid Research Letters **8**, 31–35 (2013) (cit. on p. 117).

List of Publications

1. A. Raja, L. Waldecker, **J. Zipfel**, Y. Cho, S. Brem, J. D. Ziegler, M. Kulig, T. Taniguchi, K. Watanabe, E. Malic, T. F. Heinz, T. C. Berkelbach and A. Chernikov. *Dielectric disorder in two-dimensional materials*, Nature Nano., 14, 832-837 (2019)

2. R. Perea-Causín, S. Brem, R. Rosati, R. Jago, M. Kulig, J. D. Ziegler, **J. Zipfel**, A. Chernikov and E. Malic. *Exciton propagation and halo formation in two-dimensional materials*, Nano Lett., 19, 7317-7323 (2019)

3. S. Brem, **J. Zipfel**, M. Selig, A. Raja, L. Waldecker, J. D. Ziegler, T. Taniguchi, K. Watanabe, A. Chernikov and E. Malic, *Intrinsic lifetime of higher excitonic states in tungsten diselenide monolayers*, Nanoscale, 11, 12381-12387 (2019)

4. **J. Zipfel**, J. Holler, A. A. Mitioglu, M. V. Ballottin, P. Nagler, A. V. Stier, T. Taniguchi, K. Watanabe, S. A. Crooker, P. C. M. Christianen, T. Korn. and A. Chernikov. *Spatial extent of the excited exaction states in WS2 monolayers from diamagnetic shifts*, Phys. Rev. B., 98, 075438 (2018)

5. M. Kulig*, **J. Zipfel***, P. Nagler, S. Blanter, C. Schüller, T. Korn, N. Paradiso, M. M. Glazov and A. Chernikov. *Exciton diffusion and halo effects in monolayer semiconductors*, Phys. Rev. Lett., 120, 207401 (2018)
   *both authors contributed equally to the work

6. P. Steinleitner, P. Merkel, A. Graf, P. Nagler, K. Watanabe, T. Taniguchi, **J. Zipfel**, C. Schüller, T. Korn, A. Chernikov, S. Brem, M. Selig, G. Berghäuser, E. Malic and R. Huber. *Dielectric engineering of electronic correlations in a van der Waals heterostructure*, Nano Lett., 18, 1402-1409 (2018)

In revision:

7. **J. Zipfel**, M. Kulig, R. Perea-Causín , S. Brem, J. D. Ziegler, R. Rosati, T. Taniguchi, K. Watanabe, M.M. Glazov, E. Malic and A. Chernikov. *Exciton diffusion in monolayer semiconductors with suppressed disorder*, arXiv:1911.02909 (2019)

Words of gratitude

Now, at last, follow two particularly important pages, as I want to use these few lines to express my gratitude towards all those that accompanied me on the course of this work.
First of all, I want to thank our collaborators once again, for all the time and effort they put into our joint works. Furthermore, Prof. Dr. Christian Schüller, who agreed to be the second examiner of this work as well as Prof. Dr. Vladimir Braun and Prof. Dr. Dominique Bougeard who volunteered as additional examiners. Thank you, I do not take this for granted.

Then there are a few people I have to thank in particular:
First and foremost my advisor, *Alexey Chernikov*, who did not only advise, but also help and support where he could, teach and guide where he needed to as well as criticize where he had to. I really do thank you for all of those things and for everything that I have learned in the past three years. Working with you was always so easy-going and I really did enjoy every part of it. I hope that we may continue working together in the same joyful and pleasant way.
Marvin Kulig, my colleague from start on, who showed me around and is probably the person to whom I owed this position. I particularly remember the first year where it was just the two of us in the office. But that was fine since you were always such great company with us being involved in countless interesting discussions and debates.
Jonas Ziegler for generally being an amazing colleague to have around. We always had such a great time in the lab and office, regardless whether we actually worked or were just pondering over food. Even more though, I enjoyed the times outside the office, in particular the conferences in St. Petersburg and Toulouse, which were quite the experience.
Koloman Wagner for being an equally amazing colleague to have around. Thank you for a lot of in-depth science talks, but also for introducing me to the pleasant concept of taking a break now and then and just shit-talk a bit with you guys.
Barbara Meisinger and *Edith Wietek* for simply making office hours in these last few months more enjoyable.
Furthermore, I thank everyone who supported me during the writing of this work. Especially my girlfriend *Andrea* for simply listening when I was close to mental

breakdowns, *my parents* for endless support and motivation, my brother *Lukas* who took at lot of time to give advice where he could, although I know he had more important things to do and, of course, my sister *Amelie* who I can not thank enough for how much work (and commas) she actually put into this, reading and correcting for hours and hours on end (except for these two pages, which is why there are probably plenty of mistakes. Sorry little sister!).
I would also like to thank those outside of work, my friends, for always being supportive and sometimes even curious about what I actually do. Finally, there are a lot more people that I would like to acknowledge, but there are just too many to name them all. So please do not be mad with me. I thank each and everyone of you who simply made my time here more pleasant and enjoyable.

To all of you I really am grateful,

von Herzen, Danke!